Binary Star Systems and Extrasolar Planets

by

Matthew Ward Muterspaugh

Submitted to the Department of Physics
in partial fulfillment of the requirements for the degree of

Doctor of Philosophy

at the

MASSACHUSETTS INSTITUTE OF TECHNOLOGY
[September 2005]
July 2005

Author .....
Department of Physics
July 6, 2005

Certified by .....
Bernard F. Burke
Professor Emeritus
Thesis Supervisor

Accepted by 7/6/05
Thomas Greytak
Associate Department Head for Education

Binary Star Systems and Extrasolar Planets

by

Matthew Ward Muterspaugh

Submitted to the Department of Physics
on July 6, 2005, in partial fulfillment of the
requirements for the degree of
Doctor of Philosophy

Abstract

For ten years, planets around stars similar to the Sun have been discovered, confirmed, and their properties studied. Planets have been found in a variety of environments previously thought impossible. The results have revolutionized the way in which scientists understand planet and star formation and evolution, and provide context for the roles of the Earth and our own solar system.

Over half of star systems contain more than one stellar component. Despite this, binary stars have often been avoided by programs searching for planets. Discovery of giant planets in compact binary systems would indirectly probe the timescales of planet formation, an important quantity in determining by which processes planets form.

A new observing method has been developed to perform very high precision differential astrometry on bright binary stars with separations in the range of $\approx 0.1 - 1.0$ arcseconds. Typical measurement precisions over an hour of integration are on the order of 10 micro-arcseconds (μas), enabling one to look for perturbations to the Keplerian orbit that would indicate the presence of additional components to the system.

This method is used as the basis for a new program to find extrasolar planets. The Palomar High-precision Astrometric Search for Exoplanet Systems (PHASES) is a search for giant planets orbiting either star in 50 binary systems. The goal of this search is to detect or rule out planets in the systems observed and thus place limits on any enhancements of planet formation in binaries. It is also used to measure fundamental properties of the stars comprising the binary, such as masses and distances, useful for constraining stellar models at the 10^{-3} level.

This method of differential astrometry is applied to three star systems. δ Equulei is among the most well-studied nearby binary star systems. Results of its observation have been applied to a wide range of fundamental studies of binary systems and stellar astrophysics. PHASES data are combined with previously published radial velocity data and other previously published differential astrometry measurements to produce a combined model for the system orbit. The distance to the system is determined to within a twentieth of a parsec and the component masses are determined at the level of a percent.

κ Pegasi is a well-known, nearby triple star system consisting of a "wide" pair with semi-major axis 235 milli-arcseconds, one component of which is a single-line spectro-

scopic binary (semi-major axis 2.5 milli-arcseconds). Using high-precision differential astrometry and radial velocity observations, the masses for all three components are determined and the relative inclination between the wide and narrow pairs' orbits is found to be 43.8 ± 3.0 degrees, just over the threshold for the three body Kozai resonance. The system distance is determined to a fifth of a parsec, and is consistent with trigonometric parallax measurements.

V819 Herculis is a well-studied triple star system consisting of a "wide" pair with 5.5 year period, one component of which is a 2.2-day period eclipsing single-line spectroscopic binary. Differential astrometry measurements from PHASES determine the relative inclination of the short- and long-period orbits.

Finally, the prospects for finding planets that simultaneously circle both stars in a binary system are evaluated. Planet searches of this type would represent a complementary investigation to PHASES and contribute similar scientific results.

Thesis Supervisor: Bernard F. Burke
Title: Professor Emeritus

Acknowledgments

I thank Bernard Burke for being my advisor. You took a chance on a student who arrived without an astrophysics background, encouraged me to pursue an ambitious project of an original type, and offered support in making the right contacts to gain access to facilities necessary for my research goals. When my progress stalled on particularly challenging steps in developing analysis algorithms, you always knew a reference in which someone had previously solved the same problem in a way that could be applied to my work. You have been everything I have needed in a research advisor.

I thank Ben Lane, who has been an equal contributor and partner in developing the observational techniques and science presented in this thesis. It has been, and will continue to be, a very beneficial collaboration, and a good friendship.

I thank Shri Kulkarni, who has been very generous in supporting my research, and is helping to guide my career.

I thank Kevin Rykoski, friend and PTI night assistant. You go beyond the call of duty, often going to work on your days off to fix equipment, help with alignments, or just participate in friendly conversation with out-of-town observers. The science presented in this thesis was only possible because you learned a very complicated observing mode, allowing us to continue taking data even when I was on the opposite coast from the observatory. Our conversations on sports and politics have made observing a relaxing time.

I thank Maciej Konacki, who has developed a very impressive radial velocity program for binary stars that pursues the same science goal as PHASES, to find planets in binary star systems. Instead of seeking competition between the two techniques, it has been a pleasant experience to work together, combining our observations to develop much more complete models of target systems, as evidenced in chapter 4 of this thesis. I look forward to continued collaboration between the astrometry and radial velocity programs.

Mark Colavita's input has been very valuable to my Ph.D. research. Because your varied expertise is well-known, the demands for your time are always many, but you have always found time to contribute to the PHASES astrometry project. Whether it was developing a reliable way to align metrology systems at PTI, guiding me through procedures at PTI that I had not previously attempted, or providing the key incite necessary to develop a robust method for analyzing the astrometric data in the presence of high noise levels, you have always been impressive in your ability to rapidly get up to speed on the current developments and direct me toward the appropriate next step.

I thank the PTI collaboration, who have opened their instrument to an outsider. The efforts of collaboration members have made PTI a very well engineering system, which enables implementation of complicated observing modes.

I thank the staff of Palomar Observatory, whose hospitality makes observing there a pleasant experience.

I thank the Michelson Fellowship Program for financial support of my Ph.D. research pursuits.

I thank my mother for teaching my sisters and I to be motivated in our academic pursuits. I thank my father for teaching and demonstrating the way a man should live and act.

I would like to thank Guillermo, who has reminded me what it is like to be a young man just beginning to learn about the variety of wonders that exist in the world of science. Thank you also for being very understanding, flexible, and self-disciplined on days when work has prevented me from giving you the attention young men often need.

I thank the officemates of MIT 37-624: Steve Cho, Allyn Dullighan, Will Farr, John Fregeau, Jake Hartman, Miriam Krauss, Ying Liu, Mike Muno, Eric Pfahl, Jeremy Schnittman, and Mike Stevens. Whether the discussion was a question of astrophysics or a political debate, it was always entertaining and is a rich part of my memories of MIT. Thank you to Jeff Blackburne who, despite being cursed with inferior foosball skills than I, was always willing to help with a study break at the foosball table. To all the astrophysics graduate students, I thank you for your friendship.

I thank Dr. Robert E. Pollock of Indiana University, my undergraduate advisor. Thank you for introducing me to scientific researching and teaching me the variety of skills one must know to be a versatile experimental researcher.

I thank Paul Schechter, who guided me during the transition from plasma physics to astrophysics, remained current with my research program, and continues to contribute to my development as an astrophysicist by serving on my thesis committee.

I thank Saul Rappaport for his prompt and always on target feedback, offering a unique perspective on my research.

I thank Edmund Bertschinger, who took an interest in my research despite it being in a very different area of astrophysics than his own. You provided key ideas about how best to analyze the astrometric data.

I thank Jim Elliot, for promoting and supporting the ideas for new research paths that I will be pursuing after graduation.

I thank Martin Dominik and the PLANET collaboration for supplying the graphs for Figure 6-4.

Finally, I thank my wife, Anel, who always filled in for me during the times when graduate school kept me too busy, who had hot baths already prepared for me when I arrived home after taking a general exam, who has supported me during times when I struggled in research, and congratulated me with every step forward in my studies. You did not complain when observing trips took me to California for five days in a row, nor when I was away on extended conferences and workshops. Our wedding was at a time of transition for me, as I decided to direct my research away from plasma physics and begin to explore astrophysics, which was a new interest for me at the time. Your support and understanding have made it possible for me to complete this thesis.

Contents

List of Figures

List of Tables

Chapter 1

Background and Motivation

Prior to the recent discoveries of the first confirmed extrasolar planetary systems, theoretical models of star and planet formation were developed that only explained systems like our own. The most accepted of these was the Safronov model [Safronov, 1972]. A dense region of a molecular cloud undergoes gravitational collapse, its angular momentum changing its shape to a disk in the process. The center of collapse becomes a protostar and dust particles combine to form planet cores in the disk. At small radii, the protostar's heat removes gas from the disk. At large radii, enough gas remains to form envelopes about rocky cores and create giant planets.

Surveys show that over half of star systems contain more than one stellar components. The probability of a star forming without a stellar companion and later becoming a member of a binary via encounters with other stars is very low in most environments (except dense globular clusters). This indicates the Safronov model is an incomplete description of star formation because it predicts only one star being formed at a time. Observational studies of binaries can determine in what ways the Safronov model must be modified to include binaries, and better constrain details of the star formation model.

On the planet formation side, this model proved to be insufficient to explain even the first planets discovered outside our solar system. Objects with masses of terrestrial planets were detected orbiting a pulsar [Wolszczan and Frail, 1992]—the Safronov model does not explain how planets can form in such an environment. The discovery of a planet orbiting the main sequence star 51 Pegasi [Mayor and Queloz, 1995] was surprising because despite the planet being similar to Jupiter in mass, it was found to orbit its star very closely (with an orbital period of only four days). Searching for planets in a variety of places (even those where basic models predict they can not form) promotes the development of more detailed formation models.

For reasons of observational difficulty, narrowly separated binaries are avoided by most planet-finding methods. Searches for planets in close binary systems explore the degree to which stellar multiplicity inhibits or promotes planet formation and long term system stability. There are two generalized configurations for which planets form stable hierarchical systems in binaries. "S-type" planets orbit closely to one star of a relatively wide binary, while "P-type" or circumbinary planets have large orbits around both stars of a more compact binary. The companion star is typically

unresolved, limiting the precisions of many planet-finding techniques.

1.1 Binary Stars

It is generally accepted that the vast majority of stars that will become binaries have already established their binarity by the time that planets begin to form. Observational support for this assumption comes from observations of young binary stars and protostars that have circumstellar and circumbinary disks of the type in which planets are thought to form around single stars.

The study by Duquennoy and Mayor [1991] has demonstrated that the frequency of binaries (BF) defined as

$$\text{BF} = \text{No. of Multiples/Total No. of Systems}$$

among field stars older than 1 gigayear (Gyr) is 57%. The studies of multiplicity of premain-sequence stars (PMS) in the Taurus and Ophiuchus star forming regions have shown that BF for systems in the separation range 1 to 150 AU is twice as large as that of the older field stars [Simon et al., 1995]. Further investigations have concluded that BF is lower for young stellar clusters (and similar to BF of the field stars) and that the binary frequency for PMS seems to be anti-correlated with stellar density [Mathieu et al., 2000]. Nonetheless, BF is very high for both field and premain-sequence stars and effectively binary formation must be a major component of the star formation studies. It is perhaps because our own solar system has only one stellar component that much focus has been placed on understanding star formation as a process that causes just one star to be formed, models of which produce an unresolved mystery concerning how angular momentum is dissipated from the new star. This problem of angular momentum dissipation is easily mitigated when stars form as multiples—excess angular momentum is transferred to orbital motion. If single stars form in multiples that are later disrupted, this proposed solution to the angular momentum transport problem can be applied generally.

Similarly, one may conclude that the typical setting for the planet formation is probably that of a binary system and it may not be possible to assess the overall frequency of extrasolar planets without addressing the binary systems. Yet, current radial velocity (RV) surveys for extrasolar planets favor single stars. This bias is driven by the observing technique and since there is a growing evidence of the occurrence of planets in binary and multiple stellar systems, one can no longer ignore the subject of their formation and properties.

1.2 Extrasolar Planets

Starting in the early nineties there have been three major developments in the field of sub-stellar objects: (1) the discovery of the first planetary system around another star, namely PSR 1257+12 [Wolszczan and Frail, 1992] (2) the discovery of the first confirmed brown dwarf, the companion to Gliese 229B [Nakajima et al., 1995], and

(3) the discovery of a planet around a normal star [Mayor and Queloz, 1995]. These discoveries have propelled major observational programs and the field of brown dwarfs and extra-solar planets has exploded [see summaries Basri, 2000, Perryman, 2000, Marcy and Butler, 1998]. Thus far, over a hundred extrasolar planets have been found by different groups using precise radial velocities [http://vo.obspm.fr/exoplanetes/encyclo/encycl.html; Schneider, 2003].

The study of extrasolar planets has matured beyond the point of simply identifying planetary systems and now can explore deeper questions about the frequency of planetary systems, how planets form, and how far the range of planetary diversity extends. To start with, there are two extreme possibilities: planetary systems are rare (and essentially accounted for by the known systems) or planet formation is rich and diverse and the current sample is limited by observing techniques. The existence of an entire planetary system around a millisecond pulsar—PSR 1257+12—favors the second hypothesis. If so, the current sample selects those planets best identified by RV technique, namely planets with short orbital periods. Additional discoveries that support the hypothesis that planetary systems occur in a broad range of environments include giant planets in orbits as short as one day [Torres et al., 2003], planets with large orbital eccentricities, the possible imaging of a planet orbiting a brown dwarf [Chauvin et al., 2004], and a planet system in a globular cluster [Sigurdsson et al., 2003].

1.3 Planets in Binaries

Current theory is that planets form in and from material of dusty disks observed around young stars. Popular (professional) prejudice has it that planet formation is difficult or inhibited in binary or multiple stars because these disks might be more short-lived. However, *eighteen* of the current sample of over a hundred extrasolar planets are in binary or multiple systems (see Figure 1-3). Given that multiplicity is the norm in the solar neighborhood [57%, Duquennoy and Mayor, 1991] and star-forming regions [Simon et al., 1995], the entire issue of planets in binary and multiple stars cannot be ignored.

The radial velocity detections of planets in binary systems are quite surprising results given that binary stars are often avoided by these surveys (because the secondary will contaminate the spectrum of the primary and thereby limit the measurement precision). Since despite this bias planets are detected in stellar binaries, there is a well justified and important question of the occurrence and properties of planets in such systems. It has been recognized by Zucker and Mazeh [2002] who has noted that there may be a deficiency of "high" mass planetary companions with short period orbits around single stars whereas the opposite may be true for planets in binary systems. Indeed, recent discoveries – a brown dwarf companion with an orbital period of 1.3-day around the star HD 41004B (AB separation 21 AU) and the planet of Gl 86A with mass ($m \sin i$) of 4 M_{Jup} (binary orbital separation of 20 AU) – lend credence to this idea.

1.3.1 Circumstellar and circumbinary disks

One of the prime examples of the circumstellar disks in a binary system is the case of L1551 IRS 5. Rodriguez et al. [1998] show that L1551 IRS 5 is a binary PMS with separation of 45 AU in which each component is surrounded by a disk (see Figure 1-1). The radii of the disks are 10 AU and the estimated masses are 0.06 and 0.03 $M_{\odot}$, enough to produce planets. Recently, McCabe et al. [2003] have spatially resolved mid-infrared scattered light from the protoplanetary disk around the secondary of the PMS binary HK Tau AB . The inferred sizes of the dust grains are in the range 1.5-3 μm which suggests that the first step in the planet formation, the dust grain growth, has occurred in this disk. Altogether, there is ample evidence for the presence of disks in binary systems. Observational indicators such as excess emission at near-infrared to millimeter wavelengths but also spectral veiling, Balmer and forbidden emission lines and polarization suggest that disks can be found around each of the components (circumprimary and circumsecondary disks) as well as around the entire systems [circumbinary disks, for a review see Mathieu et al., 2000]. Specifically, millimeter and submillimeter measurements of dust continuum emission enable measurement of the total disk mass. These observations show that circumbinary disks may be reduced in size and mass but still are present even in close systems. The presence of circumbinary disks is observed at millimeter wavelengths around many PMS spectroscopic binaries. Such massive disks are however rare around wide binaries with separations 1-100 AU. This is reflected in theoretical calculations that predict circumstellar and circumbinary disks truncated by the companions [Lubow and Artymowicz, 2000]. The circumstellar disks have outer radii 0.2-0.5 times the binary separation while the circumbinary disks have the inner radii 2-3 times the semi-major axis of the binary. Finally, the measurements of the infrared excess emission show no difference in frequency of the excess among binaries and single stars. It indicates that the circumstellar material in binary systems may be similar in temperature and surface density to that in disks surrounding single stars [Mathieu et al., 2000]. Hence it seems that with the current data at hand, planet formation in close binary systems is possible.

1.3.2 Planet Formation in Binaries

The theories of planet formation in binary stellar systems are still at early stages. Two mechanisms proposed for giant planet formation in circumstellar disks—core accretion and fragmentation via gravitational instabilities—make conflicting predictions about the formation rate of planets in binaries. This is primarily due to the differences in formation timescales; core-accretion requires 1-10 million years as compared to thousand year timescales for gravitational collapse. Mayer et al. [2004] indicate that gravitational fragmentation models of planet formation predict different efficiencies for giant planet formation in binaries than in single stars, whereas core-accretion models do not. It is argued that a stellar companion will disrupt protoplanetary disks on timescales shorter than required for core-accretion. Whitmire et al. [1998] studied terrestrial planet growth in the circumprimary habitable zones in binary systems. They considered a 4-body system of 2 stars and 2 planetesimals for which by

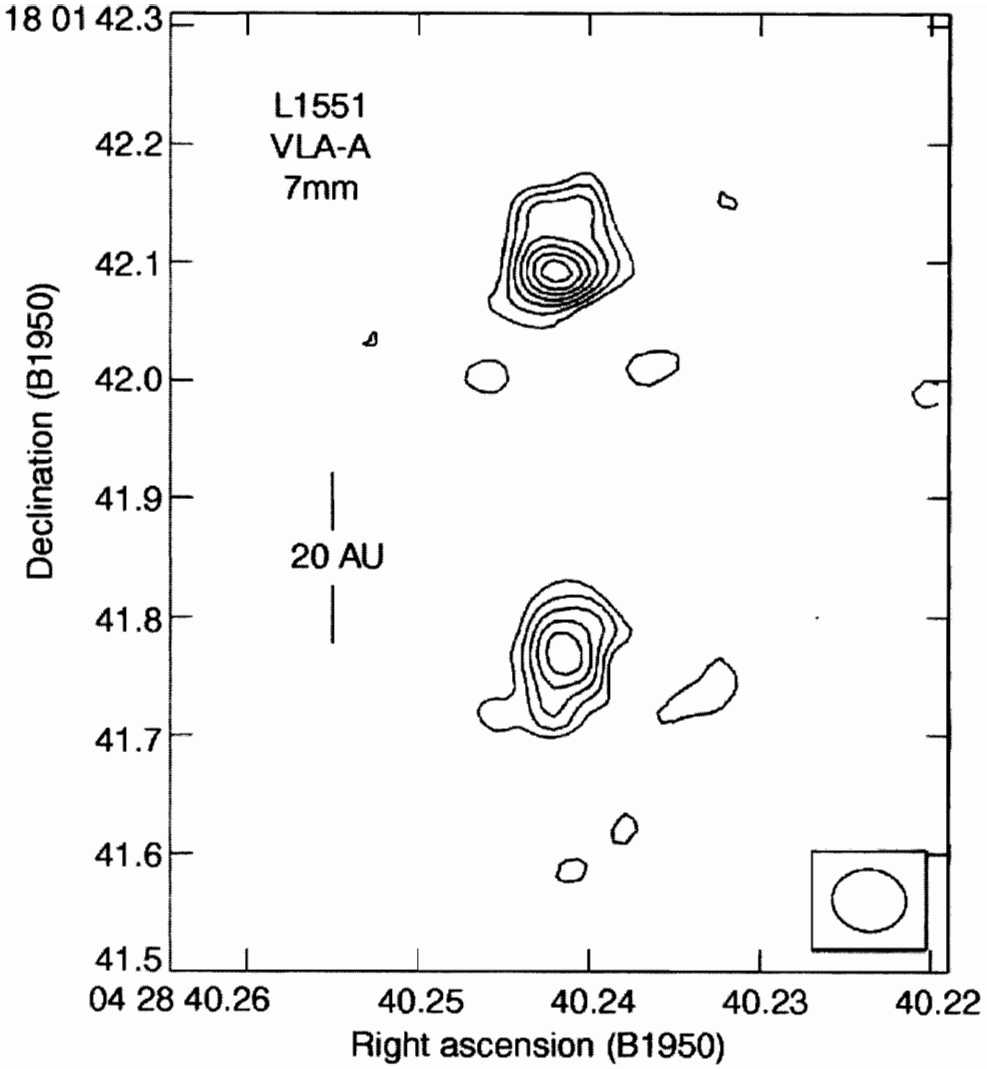

Figure 1-1: Very Large Array (VLA) map of the L1551 IRS 5 region at 7 mm [figure is from Rodriguez et al., 1998].

varying binary parameters (semi-major axis, eccentricity, mass ratio) they were able to determine a critical semi-major axis of the binary below which the secondary does not allow a growth of planetesimals (planetesimals are accelerated by the secondary, the relative velocity of planetesimals is larger than critical and their collisions become destructive). Based on this criterion, they concluded that about 60% of nearby solar-type binaries cannot be excluded from having a habitable planet. Marzari and Scholl [2000] analyzed α Cen AB (semi-major axis of 23 AU, eccentricity of 0.52, mass ratio 1.1/0.92), a prototype close binary system, and demonstrated that planetesimals can accrete into planetary embryos. Barbieri et al. [2002] continued the study and showed that planetary embryos can grow into terrestrial planets in about 50 Myr. Fragmentation models by Boss [1998] claim that giant planet formation is enhanced by the presence of stellar companions–when no binary is present, the disk is more stable and less likely to fragment into planets. However, Nelson [2000] argues that gas heating causes both mechanisms to fail to produce planets in binaries of moderate separation (50 A.U.). Clearly, there is a lack of consensus and the planet formation theories would certainly benefit from observational constraints.

1.3.3 Binary Planet Stability

Theoretical work of planet formation in close binary systems is at a rudimentary stage. Yet, as demonstrated by numerical studies [Holman and Wiegert, 1999], planets (if formed) in binary systems can enjoy a wide range of stable orbits. There is a clear need to supply observational constraints on the occurrence and orbital properties of extrasolar planets in binary systems to provide the key information for the theories of their formation. Unfortunately, it is well known that current RV surveys are biased against binary stars [e.g. see Patience et al., 2002]. The radial velocity surveys exclude binaries with separations of less than 2 arcsecond to avoid the problem posed by the "contamination" caused by the second star [Vogt et al., 2000]. Imaging and particularly coronographic surveys are similarly biased (mainly because current coronographs can suppress light from only one object in the field).

The problem of stability of the planetary orbits in binaries has been recognized for a long time. Most often, it was approached with the aid of numerical studies of the elliptic restricted three-body problem. The orbital configurations considered include the so-called P-type (Planet-type, circumbinary orbits), S-type (Satellite-type, circumprimary or circumsecondary orbits) and L-type orbits (Librator-type, orbits around stable Lagrangian points L4 or L5 for the mass ratio $\mu < 0.04$). There are many papers concerning the stability of S-type motions [e.g. Benest, 2003, Pilat-Lohinger and Dvorak, 2002, Benest, 1996, 1993, 1989, 1988, Rabl and Dvorak, 1988]. These studies concentrated on developing empirical stability criteria in the framework of the circular three-body problem [see e.g. Graziani and Black, 1981, Black, 1982, Pendleton and Black, 1983]. The P-type motions have also been investigated [Pilat-Lohinger et al., 2003, Broucke, 2001, Holman and Wiegert, 1999]. Until now however, there is no observational evidence that they exist. The curious L-type orbits have also attracted the interest of researchers [see e.g. Laughlin and Chambers, 2002].

Most of these studies have been performed by means of direct numerical integra-

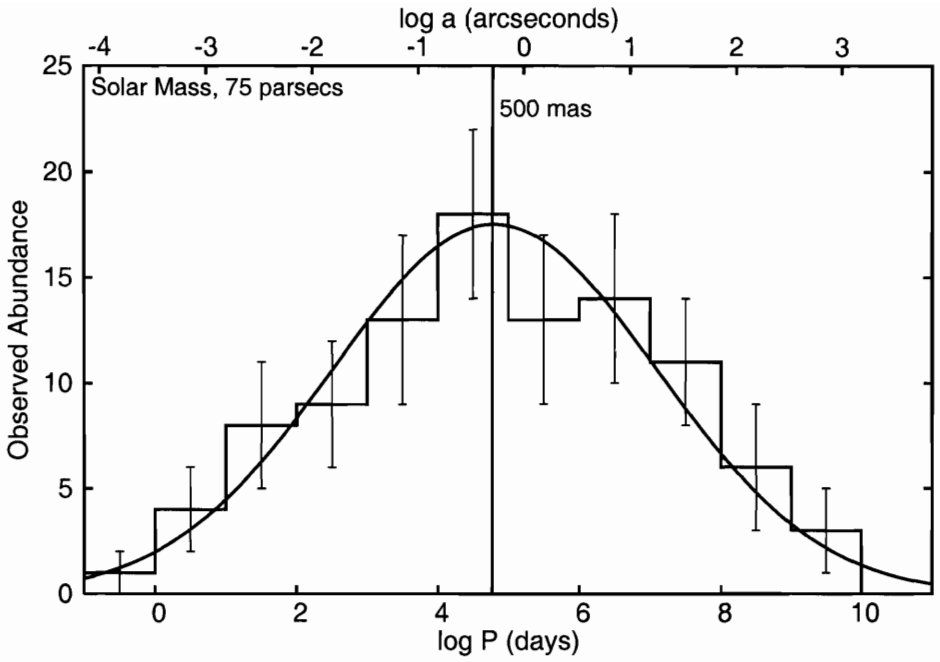

Figure 1-2: The relative population frequency of observed binary stars. Planets are most easily detected in nearby systems (within ≈ 100 parsecs), for which the binary distribution peaks at separations on order of tenths of arcseconds. [Figure is from Duquennoy and Mayor, 1991].

tions, excluding works by some authors, e.g., Pilat-Lohinger et al. [2003], who applied the FLI indicator (FLI, Fast Lyapunov Indicator). They have many limitations: most of the analytical works are done for circular binaries, numerical studies have been restricted to special mass ratios and the integration have been limited to fairly short times. Also, they are almost exclusively restricted to the framework of the three body problem. These drawbacks have been addressed in the recent, remarkable work by Holman and Wiegert [1999] who studied a full range of mass ratios, eccentricities and long integration times (at least 10^4 periods of the binary). They demonstrated that planets in binaries can enjoy a wide range of stable orbits. The stability criteria are most sensitive to the ratio of planet-binary semimajor axis; one can derive "observers' rules of thumb" from the collected theoretical work that P-type planets are stable if they have semimajor axis 3 times larger than that of the binary, and S-types are stable if they are in orbits closer than 1/7 the binary separation.

1.3.4 Planet Frequency versus Binary Separation

The lifetimes of circumstellar disks in binary systems are expected to decrease as the binary separation shrinks. Thus, one may set limits on the timescales over which giant planet formation occurs by decreasing the separations of binaries in which planets are sought. This also allows one to search for any enhancements in formation rates

due to increased disk turbulence that are predicted in some planet formation theories. Finally, the distribution of separations of nearby binaries peaks at less than an arcsecond, a separation smaller than that easily probed by traditional high precision radial velocity techniques.

There are also observational reasons for searching for planets in binaries. In particular, the binary companion makes a convenient nearby reference for astrometric observations. The chance of finding an unrelated but still bright reference star close on the sky to a target is small, which limits the number of targets available to astrometric study. Astrometry has several advantages over other techniques. While radial velocity observations can only set a lower limit on a companion mass, which is degenerate with orbital inclination, astrometry measures companion mass directly. Astrometry is also more sensitive to long period companions. The anticipated diversity in extrasolar system planets has driven astronomers and agencies to consider a multitude of discovery techniques. Each technique has its strengths. This complementarity of sensitivity is one of the principal motivations for the Keck Interferometer and the Space Interferometer Mission (SIM).

1.4 PHASES: The Palomar High-precision Astrometric Search for Exoplanet Systems

The Palomar High-precision Astrometric Search for Exoplanet Systems (PHASES) is a search for S-type giant planets orbiting either star in 50 binary systems. The goal of this search is to detect or rule out planets in the systems observed and thus place limits on any enhancements of planet formation in binaries. This sensitivity-limited search may be extended to a more complete survey of up to 500 stars with an upgraded observational system. The method used to conduct this survey is described in chapter 2 of this thesis. Though the time span of the search does not yet allow us to detect planets, three years of future operation in this mode are anticipated. chapters 3, 4, and 5 each discuss a binary of interest studied with this method, The final chapter discusses techniques for detecting P-type planets; such a search would be complementary to PHASES.

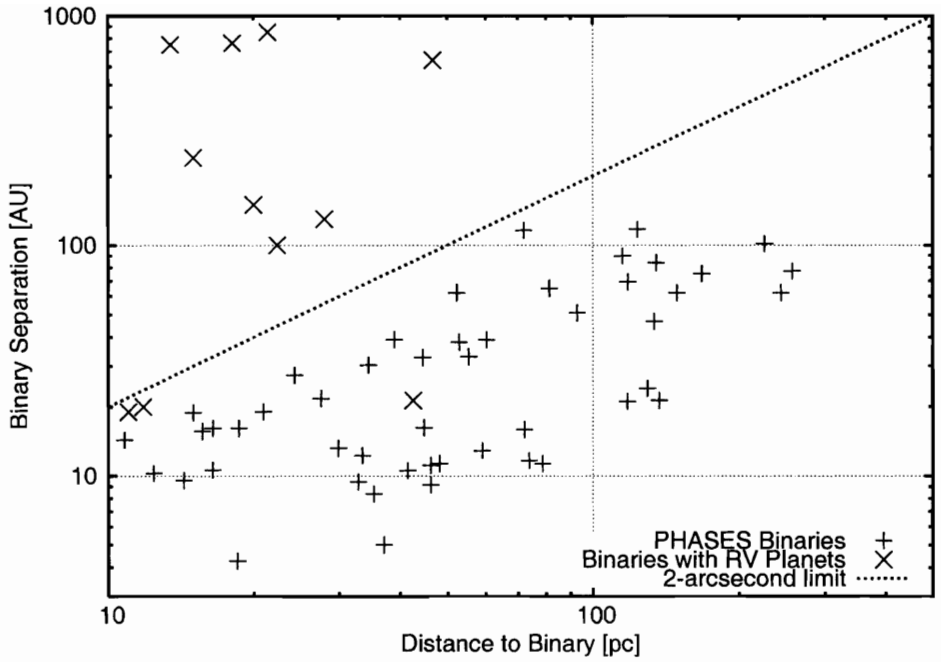

Figure 1-3: The distribution of binaries from the PHASES sample compared to the three binaries with planets which have the smallest binary separation. The 2-arcsecond selection effect is visible.

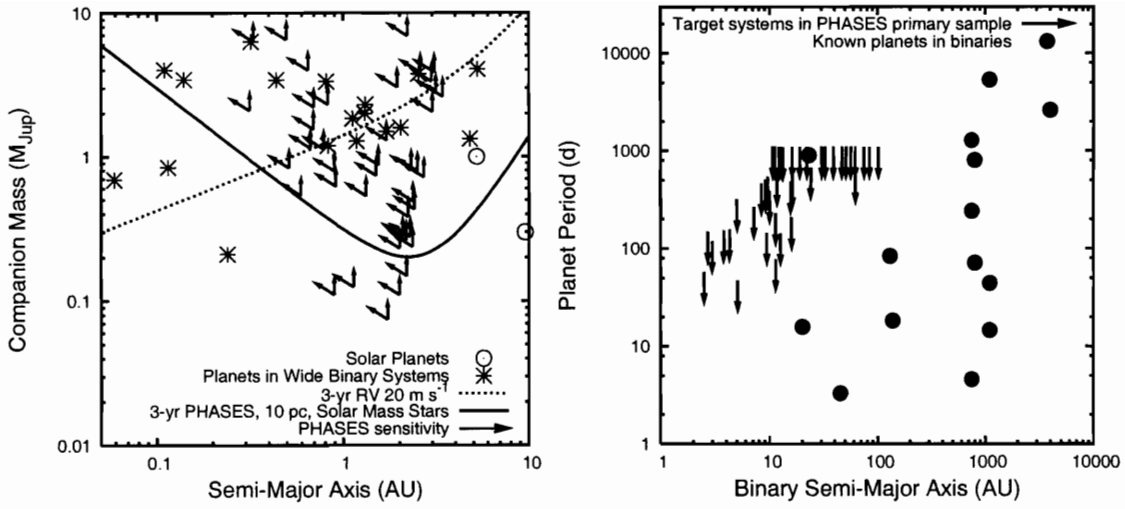

Figure 1-4: A comparison of the performance of PHASES astrometric performance for detecting planets in sub-arcsecond binaries and radial velocity observations of wider systems. In the left graph, radial velocity and astrometry measurements can detect planetary companions in the phase spaces above the plotted curves. Astrometry is sensitive to much lower mass planets near the habitable zone, and can be used to search for planets in binaries with much smaller physical separations. Note in the right graph that for several PHASES targets, the maximum stable planet period is less than three years; orbital stability plays a bigger role in these closely bound systems.

Chapter 2

Narrow Angle Astrometry

A new observing method was developed to perform very high precision differential astrometry on bright binary stars with separations in the range of $\approx 0.1 - 1.0$ arcseconds. Typical measurement precisions over an hour of integration are on the order of 10 micro-arcseconds (μas), enabling one to look for perturbations to the Keplerian orbit that would indicate the presence of additional components to the system. This method of very-narrow-angle astrometry forms the basis of a search for extrasolar planets orbiting either stellar component of the binary. It is also used to measure fundamental properties of the stars comprising the binary, such as masses and distances, useful for constraining stellar models at the 10^{-3} level. This method forms the basis for the Palomar High-precision Astrometric Search for Exoplanet Systems (PHASES).

2.1 Introduction

Long-baseline optical interferometry promises high precision astrometry using modest ground-based instruments. In particular the Mark III Stellar Interferometer [Shao et al., 1988] and Navy Prototype Optical Interferometer [Armstrong et al., 1998] have achieved global astrometric precision at the 10 mas (1 mas = 10^{-3} arcseconds) level [Hummell et al., 1994], while the Palomar Testbed Interferometer (PTI) [Colavita et al., 1999] has demonstrated an astrometric precision of 100 μas (1μas = 10^{-6} arcseconds) between moderately close (30 arcsecond) pairs of bright stars [Shao and Colavita, 1992, Colavita, 1994, Lane et al., 2000]. While interferometric and astrometric methods have proven very useful in studying binary stars, and have long been argued to be well-suited to studying extra-solar planets [Colavita and Shao, 1994, Eisner and Kulkarni, 2001], to date results using these techniques have been limited [Benedict et al., 2002].

There are several reasons why it is desirable to develop viable astrometric planet-detection methods. Most importantly, the parameter space explored by astrometry is complementary to that of radial velocity (astrometry is more sensitive to larger separations). Second, unlike current radial velocity detections, astrometric techniques can be used to determine the orbital inclination of a planet. Finally, astrometry is par-

Figure 2-1: The Palomar Testbed Interferometer as seen from the catwalk of the Palomar Hale 200" telescope.

ticularly well-suited for studying binary stellar systems; such systems challenge other planet-finding techniques. For example, radial velocimetry can suffer from systematic velocity errors caused by spectral contamination from the light of the second star [Vogt et al., 2000]. Similar problems are faced by coronographic techniques, where the light from the second star is not usually blocked by the occulting mask.

This chapter describes recent efforts to obtain very high precision narrow-angle astrometry using PTI to observe binary stars with separations less than one arcsecond, i.e. systems that are typically observed using speckle interferometry [Saha, 2002] or adaptive optics. Such small separations enable astrometric precision on the order of 10 μas which, for a typical binary system in the PHASES target sample (binary separation of 20 AU), should allow detection of planets with masses down to 0.5 Jupiter masses in orbits in the 2 AU range. This approach has been suggested [Traub et al., 1996] and tried [Dyck et al., 1995, Bagnuolo et al., 2003] before, though with limited precision. However, this work is unique in that it makes use of a phase-tracking interferometer; the use of phase-referencing [Lane and Colavita, 2003] removes much of the effect of atmospheric turbulence, improving the astrometric precision by a factor of order 100.

PTI is located on Palomar Mountain near San Diego, CA [Colavita et al., 1999]. It was developed by the Jet Propulsion Laboratory, California Institute of Technology for NASA, as a testbed for interferometric techniques applicable to the Keck Interferometer and other missions such as the Space Interferometry Mission, SIM. It operates in the J (1.2μm),H (1.6μm) and K (2.2μm) bands, and combines starlight from two out of three available 40-cm apertures. The apertures form a triangle with two 87 and one 110 meter baselines.

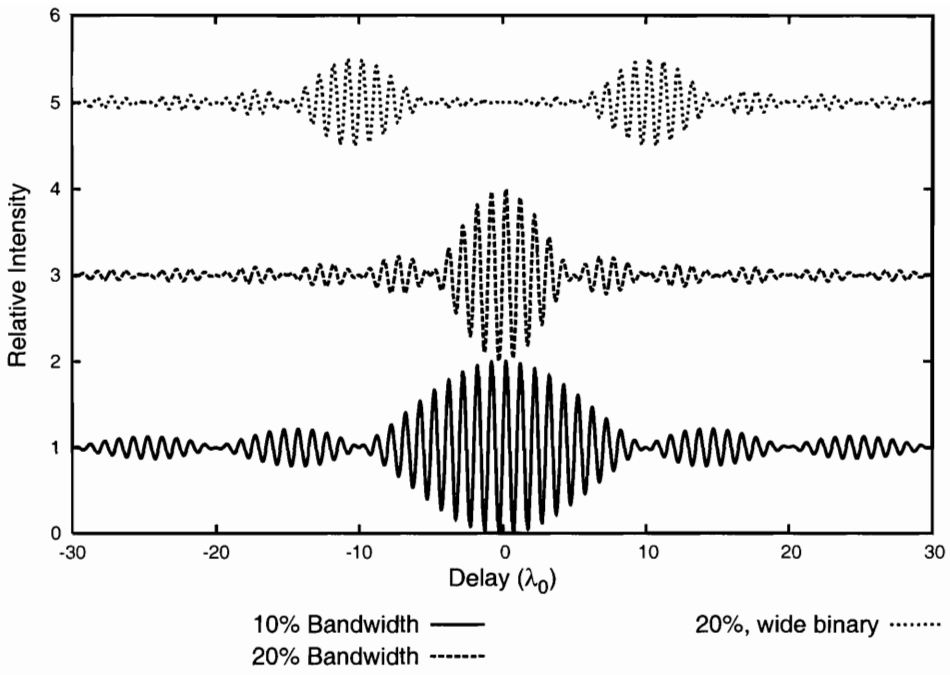

Figure 2-2: The response of an interferometer. The top two curves have been offset by 2 and 4 for clarity. The widths of the fringe packets are determined by the bandpass of the instrument, and the wavelength of fringes by an averaged wavelength of starlight. The top curve shows the intensity pattern obtained by observing two stars separated by a small angle on the sky—the observable is the distance between the fringe packets.

2.2 Optical Interferometers

In an optical interferometer light is collected at two or more apertures and brought to a central location where the beams are combined and a fringe pattern produced on a detector (at PTI, the detectors are NICMOS and HAWAII infrared arrays, of which only a few pixels are used). For a broadband source of central wavelength λ and optical bandwidth $\Delta\lambda$ (for PTI $\Delta\lambda = 0.4\mu$m), the fringe pattern is limited in extent and appears only when the optical paths through the arms of the interferometer are equalized to within a coherence length ($\Lambda = \lambda^2/\Delta\lambda$). For a two-aperture interferometer, neglecting dispersion, the intensity measured at one of the combined beams is given by

$$I(x) = I_0 \left(1 + V \frac{\sin(\pi x/\Lambda)}{\pi x/\Lambda} \sin(2\pi x/\lambda)\right) \tag{2.1}$$

where V is the fringe contrast or "visibility", which can be related to the morphology of the source, and x is the optical path difference between arms of the interferometer. More detailed analysis of the operation of optical interferometers can be found in *Principles of Long Baseline Stellar Interferometry* [Lawson, 2000].

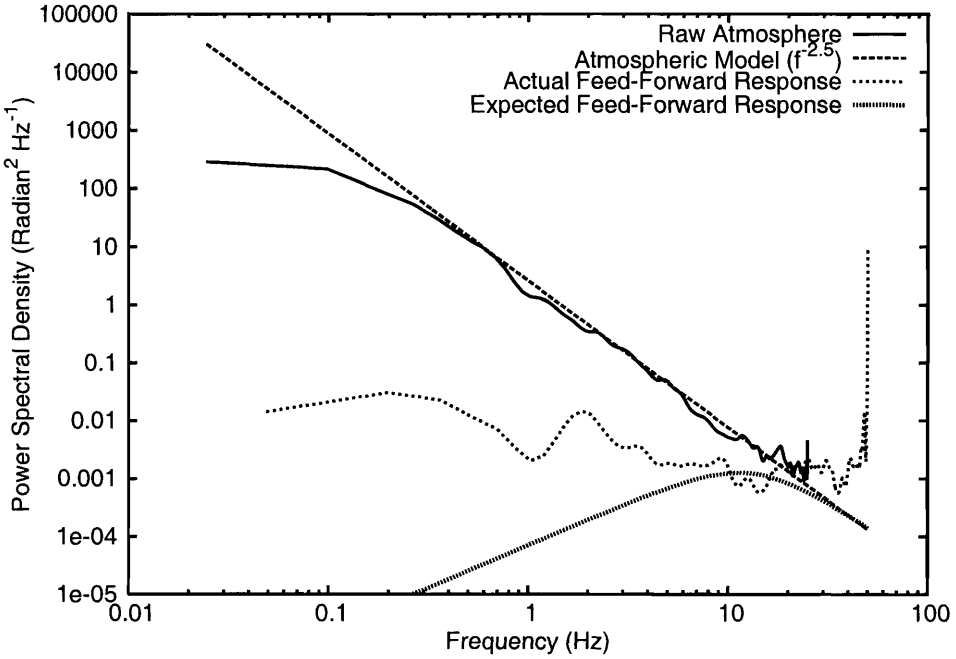

Figure 2-3: Power spectral density of the fringe phase as measured by PTI [Lane and Colavita, 2003]. The phase PSD is best fit by a power law $A(f) \propto f^{-2.5}$, close to the the nominal -8/3 slope of Kolmogorov theory. Also shown is the effective PSD of the phase noise after phase referencing has stabilized the fringe.

2.2.1 Interferometric Astrometry

The location of the resulting interference fringes are related to the position of the target star and the observing geometry via

$$d = \vec{B} \cdot \vec{S} + \delta_a\left(\vec{S}, t\right) + c \tag{2.2}$$

where d is the optical path-length one must introduce between the two arms of the interferometer to find fringes. This quantity is often called the "delay." $\vec{B}$ is the baseline—the vector connecting the two apertures. $\vec{S}$ is the unit vector in the source direction, and c is a constant additional scalar delay introduced by the instrument. The term $\delta_a\left(\vec{S}, t\right)$ is related to the differential amount of path introduced by the atmosphere over each telescope due to variations in refractive index. For a 100-m baseline interferometer an astrometric precision of 10 μas corresponds to knowing d to 5 nm, a difficult but not impossible proposition for all terms except that related to the atmospheric delay. Atmospheric turbulence, which changes over distances of tens of centimeters and on millisecond timescales, forces one to use very short exposures (to maintain fringe contrast) and hence limits the sensitivity of the instrument. It also severely limits the astrometric accuracy of a simple interferometer, at least over large sky-angles.

However, in narrow-angle astrometry one is concerned with a close pair of stars,

and the observable is a differential astrometric measurement, i.e. one is interested in knowing the angle between the two stars ($\overrightarrow{\Delta_s} = \overrightarrow{s_2} - \overrightarrow{s_1}$). The atmospheric turbulence is correlated over small angles. If the measurements of the two stars are simultaneous, or nearly so, the atmospheric term subtracts out. Hence it is still possible to obtain high precision "narrow-angle" astrometry.

2.2.2 Narrow-Angle Astrometry

Traditional interferometric narrow-angle astrometry [Shao and Colavita, 1992, Colavita, 1994] promises astrometric performance at the 10-100 micro-arcsecond level for pairs of stars separated by 10-60 arcseconds; it was first demonstrated with the Mark III interferometer for short integrations [Colavita, 1994], was extended to longer integrations and shown to work at the 100 micro-arcsecond level at PTI [Shao et al., 1999], and is expected to become operational at the Keck Interferometer in 2010. However, achieving such performance requires simultaneous measurement of the fringe positions of both stars, greatly complicating the instrument (two beam combiners and metrology throughout the entire array are required). In addition, the instrumental baseline $\overrightarrow{B}$ must be known to high precision ($\approx$ 100 microns). While this mode has been demonstrated on a limited basis at PTI, the addition of the metrology system severely limits the throughput of the instrument and hence the number of observable targets.

For more closely spaced stars, it is possible to operate in a simpler mode. PTI has been used to observe pairs of stars separated by no more than one arcsecond. In this mode, the small separation of the binary results in both binary components being in the field of view of a single interferometric beam combiner. The fringe positions are measured by modulating the instrumental delay with an amplitude large enough to record both fringe packets. This eliminates the need for a complex internal metrology system to measure the entire optical path of the interferometer, and dramatically reduces the effect of systematic error sources such as uncertainty in the baseline vector (error sources which scale with the binary separation).

However, since the fringe position measurement of the two stars is no longer truly simultaneous it is possible for the atmosphere to introduce path-length changes (and hence positional error) in the time between measurements of the separate fringes. To reduce this effect a fraction of the incoming starlight is redirected to a separate beam-combiner. This beam-combiner is used in a "fringe-tracking" mode [Shao and Staelin, 1980, Colavita et al., 1999] where it rapidly (10 ms) measures the phase of one of the starlight fringes, and adjusts the internal delay to keep that phase constant. The fringe tracking data is used both in real-time (operating in a feed-back servo, after which a small—but measurable—residual phase error remains) and in post-processing (the measured residual error is applied to the data as a feed-forward servo). This technique—known as phase referencing—has the effect of stabilizing the fringe measured by the astrometric beam-combiner. For this observing mode, laser metrology is only required between the two beam combiners through the location of the light split (which occurs after the optical delay has been introduced), rather than throughout the entire array.

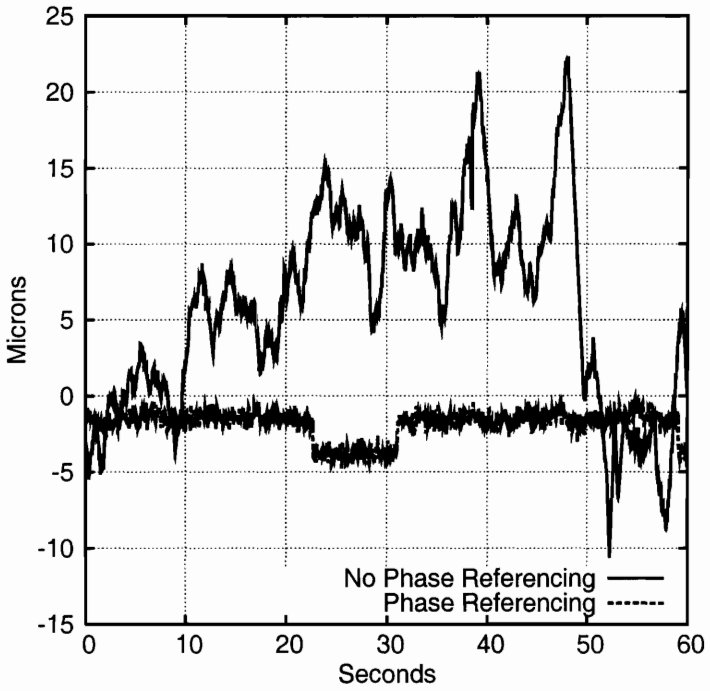

Figure 2-4: An example of how phase referencing stabilizes the fringe. Shown are plots of the fringe position seen by the a PTI fringe tracker with and without phase referencing. The two data sections were taken within 200 seconds of each other. The target star was HD 177724 ($m_K = 2.99$, A0V). One detector was operated with 20 ms sample times and open loop, i.e., measuring but not correcting the phase. In the first experiment, without phase referencing, the raw atmospheric phase fluctuations are observed. For the second data set plotted, a second beam combiner was operated in closed loop, with its phase information being applied to the open loop beam combiner, reducing the phase fluctuations it observed. Note the jump near 20 seconds in the phase-referenced data; this is caused by mis-identification of the central fringe. This is easily detected and corrected during post-processing by measurements of the interferometer's group delay, or fringe phase versus wavelength.

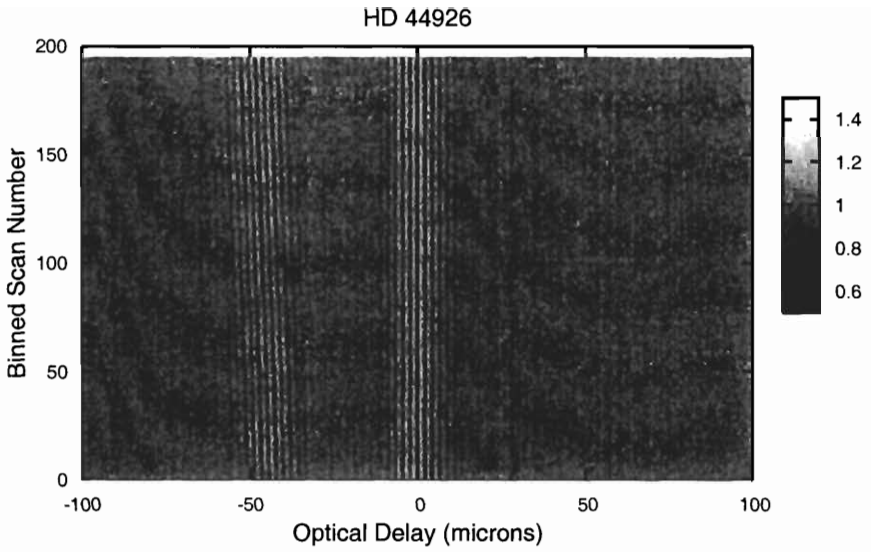

Figure 2-5: Measured intensity in the detector as a function of differential optical path, for successive scans of the speckle binary system HD 44926. Each scan takes 1.5 seconds to acquire. The fringe tracker was locked on to the bright star (around 0), while the second star produces a fringe pattern which starts at -40 μm and moves due to Earth rotation. Although the second fringe pattern is relatively faint, the effect of coherently co-adding 500–2000 scans produces a high signal-to-noise ratio in the final astrometric measurement.

In making an astrometric measurement the optical delay is modulated in a triangle-wave pattern around the stabilized fringe position, while measuring the intensity of the combined starlight beams. The range of the delay sweep is set to include both fringe packets; typically this requires a scan amplitude on the order of 150 μm. Typically one such "scan" is obtained every second, consisting of up to 1000 intensity samples (the scan rate is limited by the source brightness and the requirement that > 2 samples are made per wavelength of scan amplitude). A double fringe packet based on eq. 2.1 is then fit to the data, and the differential optical path between fringe packets is measured.

2.3 Data Reduction Algorithm

The relative astrometric position is extracted from data such as that shown in Figure 2-5 as follows. Observing a binary when its baseline projected separation ($\vec{B} \cdot \vec{\Delta S}$) is of order the interferometric coherence length ($\approx 20\mu$m) or less is avoided due to potential biases associated with an imperfect template fringe packet. First, detector calibrations (gain, bias, and background) are applied to the intensity measurements.

Next, a grid in differential right ascension and declination over which to search is constructed (in ICRS 2000.0 coordinates). For each point in the search grid the expected differential delay is calculated based on the interferometer location, baseline geometry, and time of observation for each scan. These conversions were simplified using the routines from the Naval Observatory Vector Astrometry Subroutines C Language Version 2.0 (NOVAS-C; see Kaplan et al. [1989]). A model of a double-fringe packet is then calculated and compared to the observed scan to derive a χ^2 value; this is repeated for each scan, co-adding all of the χ^2 values associated with that point in the search grid. The final χ^2 surface as a function of differential R.A. and declination is thus derived. The best-fit astrometric position is found at the minimum-χ^2 position, with uncertainties defined by the appropriate χ^2 contour—which depends on the number of degrees of freedom in the problem and the value of the χ^2-minimum. The final product is a measurement of the apparent vector between the stars and associated uncertainty ellipse. Because the data were obtained with a single-baseline instrument, the resulting error contours are very elliptical, with aspect ratios at times ≥ 10.

2.3.1 Probability Distribution Function Sidelobes

One potential complication with fitting a fringe to the data is that there are many local minima spaced at multiples of the operating wavelength. If one were to fit a fringe model to each scan separately and average (or fit an astrometric model to) the resulting delays, one would be severely limited by this fringe ambiguity (for a 110-m baseline interferometer operating at 2.2μm, the resulting positional ambiguity is $\sim$ 4.1 milli-arcseconds). However, by using the χ^2-surface approach, and co-adding the probabilities associated with all possible delays for each scan, the ambiguity disappears. This is due to two things, the first being that co-adding simply improves the signal-to-noise ratio. Second, since the observations usually last for an hour or even longer, the associated baseline change due to Earth rotation also has the effect of "smearing" out all but the true global minimum. The final χ^2-surface does have dips separated by $\sim$ 4.1 milli-arcseconds from the true location, but any data sets for which these show up at the 4σ level are rejected. The final astrometry measurement and related uncertainties are derived by fitting only the 4σ region of the surface.

2.3.2 Residual Unmonitored Phase Noise

Unmonitored system phase noise affects the χ^2 surface in two ways. First, components of the phase noise that operate at frequencies faster than the scan rate cause the two fringe packets to be smeared an extra amount, and to first order this appears as extra noise in the intensity measurements. This affects the width of the χ^2 fit for each individual scan (which is designated σ_m, the "measurement" noise), and thus appears directly in the co-added χ^2 contour.

If instead the instrumental noise is much slower than an individual scan, it is essential "frozen into" the scan—for the duration of that scan, the stars really do appear to have a different separation than their true separation. The χ^2 surface for

the fit to an individual scan takes the form

$$f(d-d_j) = \frac{(d-d_j)^2}{\sigma_m^2} + n \tag{2.3}$$

where d_j is the value of the star separation that minimizes $f = \chi^2$, and n is the number of degrees of freedom of the fit (typical values for n are 400–1000; for this derivation, it suffices to assume a one-dimensional χ^2 surface as it has no curvature in the direction perpendicular to the sky-projected baseline—only Earth-rotation synthesis lifts this degeneracy). The low-frequency components of the phase noise cause d_j to vary from d_o, the true star separation, by more than one expects from measurement noise alone. By taking many such scans, one can determine this instrumental scatter (which is designated as σ_i, the "instrument" noise for an individual scan) and add (in quadrature) the instrumental noise to the measurement noise, as

$$F(d-d_o) = \frac{(d-d_o)^2}{(\sigma_m^2 + \sigma_i^2)/N} + nN \tag{2.4}$$

where N is the number of scans (N is typically hundreds to thousands).

Consider a function $f(d-d_{o_j})$ with centroid position d_{o_j}; this centroid position is distributed with probability

$$P\left(d_{o_j}\right) = \frac{e^{-\left(d_o - d_{o_j}\right)^2/2\sigma_i^2}}{\sqrt{2\pi}\sigma_i}. \tag{2.5}$$

One may naively hope that summing several instances of this function with variable d_{o_j} together would properly add the instrumental and measurement noises in quadrature. However, the summation results in

$$\begin{aligned}
\sum_{j=0}^{N} f\left(d-d_{o_j}\right) &= N\int_{-\infty}^{\infty} f\left(d-x\right) P\left(x\right) \mathrm{d}x \\
&= \frac{(d-d_o)^2}{(\sigma_m^2)/N} + nN + N\frac{\sigma_i^2}{\sigma_m^2} \\
&\neq \frac{(d-d_o)^2}{(\sigma_m^2+\sigma_i^2)/N} + nN.
\end{aligned}$$

Even if one renormalizes so that the additive term equals nN (i.e. multiply by $n/(n+\sigma_i^2/\sigma_m^2)$), this is still:

$$\sum_{j=0}^{N} f\left(d-d_{o_j}\right) = \frac{(d-d_o)^2}{(\sigma_m^2+\sigma_i^2/n)/N} + nN. \tag{2.6}$$

Note the extra factor of n dividing σ_i^2; this effectively underestimates the scan-to-scan instrumental noise by a very large amount—roughly $20\times$ for typical PHASES data.

Instead, the appropriate way to determine the scan-to-scan fit is by noticing that

the minimum value of the co-added χ^2 surface is greater than the total number of degrees of freedom nN by the amount:

$$N\frac{\sigma_i^2}{\sigma_m^2}. \tag{2.7}$$

The quantity σ_m is measured directly from the shape of the surface, which is unchanged, and the number of scans N is known. Thus, one can derive σ_i and apply it to the formal uncertainties. For 430 observations made from 2003-2005, the average value of σ_i^2/σ_m^2 was 1.43; values ranged from 0.0084 (for bright sources and good weather conditions) to 7.2.

Phase-referencing is used to decrease the amount of unmonitored phase noise during narrow-angle astrometry observations (see section 2.4.1), but some residual phase noise remains (see Figure 2-3), so the correction outlined here must be applied to the astrometric data. Synthetic data have been constructed both with and without unmonitored phase noise of the actual spectrum observed, and the data reduction algorithm determines measurement uncertainties consistent with the actual scatters in the measurements between multiple synthetic data sets. Without the additional phase-noise correction outlined here, the formal uncertainties significantly underestimate the scatter in the results.

2.4 Expected Performance

The expected astrometric performance of the new observing mode is determined by several factors contributing measurement uncertainties and biases. These are subdivided into three broad categories: (1) observations noise terms, which are fundamental to atmospheric turbulence and finite source brightness, (2) instrumental noise terms, which result from the design of the interferometer and the method in which the measurement is obtained, and (3) astrophysical noise terms, which result from the astrometric stability of the stars themselves. The size of each noise source is summarized in Table 2.1.

2.4.1 Observational Noise

In calculating the expected astrometric performance three major sources of error are taken into account: errors caused by fringe motion during the sweep between fringes (loss of coherence with time), errors caused by differential atmospheric turbulence (loss of coherence with sky angle, i.e. anisoplanatism), and measurement noise in the fringe position. Each is quantified in turn below, and the expected measurement precision is the root-sum-squared of the terms (Figure 2-6).

2.4.1.1 Loss of Temporal Coherence

The power spectral density of the fringe phase of a source observed through the atmosphere has a power-law dependence on frequency (Figure 2-3); at high frequencies

Table 2.1
Astrometric Noise Sources

Source	Section	Typical Magnitude (μas)
Temporal Decoherence	2.4.1.1	~ 5
Anisoplanatism	2.4.1.2	0.2
Photon Noise	2.4.1.3	3
Differential Dispersion*	2.4.2.1	~ 30
Baseline Errors	2.4.2.2	< 10
Fringe Template	2.4.2.3	1
Scan Rate	2.4.2.4	1
Beam Walk	2.4.2.5	0.5
Global Astrometry	2.4.2.6	$\ll 1$
Star spots	2.4.3.1	$< 8^{\dagger}$
Stellar Granulation	2.4.3.2	< 3

Table 2.1: Sources of astrometric noise.
* Depends on color difference between binary components; for many targets, this is nearly zero, but for extreme color differences, this can be hundreds of μas.
† Photometric variability accompanies star spots, of a magnitude that is easily detected for astrometric signatures of 8 μas or larger.

typically

$$A(f) \propto f^{-\alpha} \tag{2.8}$$

where α is usually in the range 2.5–2.7. The effect of phase-referencing is to high-pass filter this atmospheric phase noise. In this case, the servo is an integrating servo with finite processing delays and integration times, with the residual phase error "fed forward" to the second beam combiner [Lane and Colavita, 2003]. The response of this system to an input atmospheric noise can be written in terms of frequency (see Appendix A in Lane 2003) as

$$H(f) \;=\; \frac{1 - 2\mathrm{sinc}(\pi f T_s)\cos(2\pi f T_d) + \mathrm{sinc}^2(\pi f T_s)}{1 - 2\frac{f_c}{f}\mathrm{sinc}(\pi f T_s)\sin(2\pi f T_d) + \left(\frac{f_c}{f}\right)^2 \mathrm{sinc}^2(\pi f T_s)} \tag{2.9}$$

where $\mathrm{sinc}(x) = \sin(x)/x$, f_c is the closed-loop bandwidth of the fringe-tracker servo (for this experiment $f_c = 10$ Hz), T_s is the integration time of the phase sample (6.75 ms), and T_d is the delay between measurement and correction (done in post-processing, effectively 5 ms). The phase noise superimposed on the double fringe measured by the astrometric beam combiner has a spectrum given by $A(f)H(f)$.

The sampling of the double fringe packet takes a finite amount of time, first sampling one fringe, then the other. In the time domain the sampling function can be represented as a "top-hat" function convolved with a pair of delta functions (one positive, one negative). The width of the top-hat is equal to the time taken to sweep through a single fringe, while the separation between the delta functions is equal to

the time to sweep between fringes. In the frequency domain this sampling function becomes

$$S(f) = \sin^2(2\pi f \tau_p)\mathrm{sinc}^2(\pi f \tau_*) \tag{2.10}$$

where τ_p is the time taken to move the delay between stars ,$\Delta d/v_s$, and τ_* is the time to sweep through a single stellar fringe, Λ/v_s. v_s is the delay sweep rate.

The resulting error in the astrometric measurement, given in radians by σ_{tc}, can be found from

$$\sigma_{tc}^2 = \left(\frac{\lambda}{2\pi \mathrm{B}}\right)^2 \frac{1}{N} \int_0^\infty A(f)H(f)S(f)df \tag{2.11}$$

where N is the number of measurements. It is worth noting that if phase-referencing is not used to stabilize the fringe, i.e. $H(f) = 1$, the atmospheric noise contribution increases by a factor of $\approx 10^2$–10^3.

2.4.1.2 Anisoplanatism

The performance of a simultaneous narrow-angle astrometric measurement has been thoroughly analyzed in [Shao and Colavita, 1992]. Here the primary result for the case of typical seeing at a site such as Palomar Mountain is restated, where the astrometric error in arcseconds due to anisoplanatism (σ_a) is given by

$$\sigma_a = 540 \mathrm{B}^{-2/3} \theta t^{-1/2} \tag{2.12}$$

where B is the baseline (in meters), θ is the angular separation of the stars (in radians), and t the integration time in seconds. This assumes a standard [Lindegren, 1980] atmospheric turbulence profile; it is likely that particularly good sites will have somewhat (factor of two) better performance.

2.4.1.3 Photon Noise

The astrometric error due to photon-noise (σ_p) is given in radians as

$$\sigma_p = \frac{\lambda}{2\pi \mathrm{B}} \frac{1}{\sqrt{N}} \frac{1}{\mathrm{SNR}} \tag{2.13}$$

where N is the number of fringe scans, and SNR is the signal-to-noise ratio of an individual fringe.

2.4.2 Instrumental Noise

There are several effects internal to the instrument that can contribute noise terms or biases to the astrometric measurements. Some could potentially vary on night-to-night timescales as the optical alignments vary on roughly these timescales. Others result from properties of the measurement design.

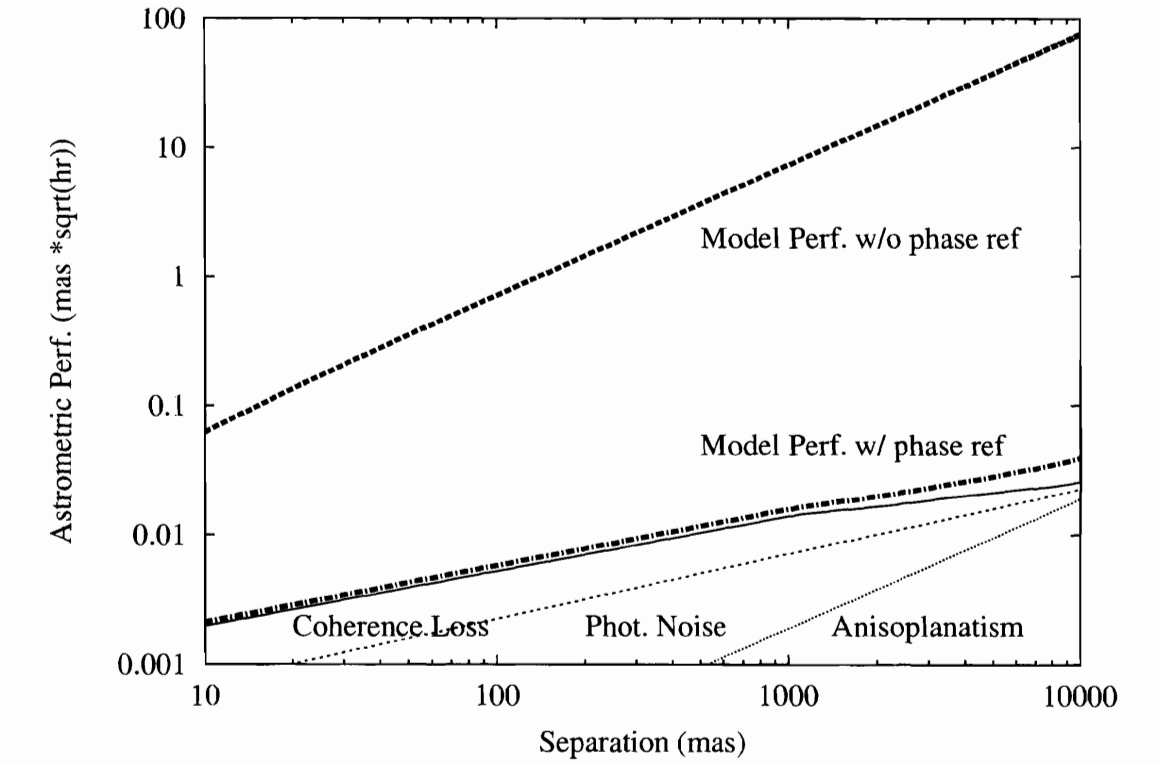

Figure 2-6: The expected narrow-angle astrometric performance in milli-arcseconds for the phase-referenced fringe-scanning approach, for a fixed delay sweep rate, and an interferometric baseline of 110 m. There are three primary sources of astrometric error in this method: angular anisoplanatism [Shao and Colavita, 1992], temporal decoherence [Lane and Colavita, 2003], and photon noise. Also shown is the magnitude of the temporal decoherence effect in the absence of phase referencing, illustrating why stabilizing the fringe via phase referencing is necessary.

2.4.2.1 Differential Dispersion

The path compensation for the geometric delay at PTI is done with delay lines in air and without dispersion compensators. At near-infrared wavelengths, air introduces a wavelength-dependent index of refraction given by [Cox, 2000]

$$\begin{aligned} n &= 1 + \left(\frac{pT_s}{p_s T}\right)\left(6.4328 \times 10^{-5} + \frac{0.029498}{146 - 1/\lambda^2} + \frac{2.554 \times 10^{-4}}{41 - 1/\lambda^2}\right) \\ &\quad -4.349 \times 10^{-5}\left(1 - 7.956 \times 10^{-3}/\lambda^2\right)\frac{p_w}{p_s} \end{aligned} \tag{2.14}$$

where λ is the vacuum wavelength in μm, p is the air pressure, p_w is the partial pressure of water vapor, $p_s = 1.01325 \times 10^5$ Pa, T is the temperature, and $T_s = 288.15$ K. The fringe packets of astrophysical sources are dispersed by an amount that depends on the difference in air paths between arms of the interferometer; this changes the shape and overall location of the fringe packets. If two stars are in the same beam and are identical in color, the change in location is common to both and cancels; similarly, the distortions of the fringe packets are common and cancel to first order in a differential measurement.

If, however, the two stars are of differing colors, each will be dispersed by a slightly different amount, and their apparent separation will be biased. The shift in the apparent position of each star's fringes can be approximated by evaluating the dispersion at the effective mean wavelength of the star in the passband. The effective mean wavelength is given by multiplying the instrumental bandpass by the stellar spectrum. For an order-of-magnitude estimate of the effect of differential dispersion, one can model the instrumental bandpass as a tophat function passing wavelengths $2 - 2.4\mu$m (nominal K-band) and the stellar spectra as blackbodies. The shifts in apparent positions for several spectral types over 40 meters of differential air path (a maximum amount for PTI) are given in Table 2.2. Note that for G5-K5 binaries, the amount is 35.8 μas and for B5-A5 it is 30.6 μas. For much more extreme color ratios, the effect can be as large as 150.6 μas for B5-M5 binaries; the PTI sample does not include such systems, as their high contrast ratios prevent observation in the mode described.

Because the stars are often observed at the same hour angles from one night to the next (and thus the delay positions are relatively common between nights), this effect introduces a much smaller scatter than that listed in the table. However, it may introduce biases in the stellar separations, and introduce scatter between observations taken in multiple baselines (for which the delay positions differ). These biases and scatters are of order the amounts given in Table 2.2.

The binaries in the observation sample are generally of components with equal brightnesses and thus similar colors. No hour-angle dependent biases significant on the level of the precision of the observations are observed (see section 2.5.1). This effect is likely to be important for traditional narrow angle astrometry methods at the Keck Interferometer or Very Large Telescope Interferometer, which aim to use field stars as astrometric references for nearby stars, and reference and target will

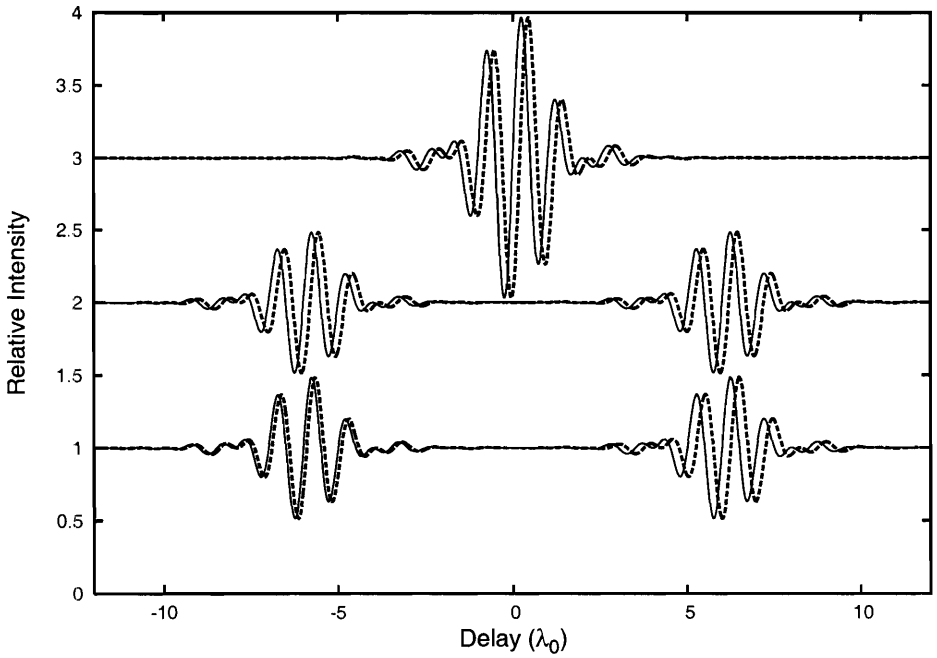

Figure 2-7: Schematic of the shift in fringe positions due to dispersion (the effect has been exaggerated for clarity). The vacuum (no dispersion) interferograms are plotted with solid lines; those dispersed by air with dotted lines.
(top) Dispersion shifts the point of zero optical path difference for a star, due to different amounts of air path in each arm of the interferometer (the effective optical path difference measured as if in vacuum).
(middle) The dispersion shift for stars of equal colors are equal and cancels; the measured separation is the same.
(bottom) Stars of unequal colors are shifted by slightly different amounts by dispersion, and the resulting measured separation is different. For very extreme color differences, the shift can be hundreds of μas.
Not shown are the shape distortions to interferograms.

Table 2.2
Differential Dispersion

Spectral Type	Effective Temperature (K)	Effective K-band Wavelength [μm]	$(n-1)$ $\times 10^4$	$(n-n_{F5})$ $\times 10^9$	$(n-n_{F5})$ $\times$38m [nm]	Error vs. F5 [μas]
O5	44500	2.1763	2.729232	0.93	35.4	73
B5	15400	2.1772	2.729229	0.66	25.0	51
A5	8200	2.1785	2.729225	0.25	9.7	20
F5	6440	2.1794	2.729223	0.00	0.0	0
G5	5770	2.1799	2.729221	-0.14	-5.4	11
K5	4350	2.1815	2.729217	-0.61	-23.3	48
M5	3240	2.1839	2.729210	-1.32	-50.3	103

Table 2.2: Effect of color-dependent differential dispersion. Stellar temperatures are for dwarf stars, from Carroll and Ostlie [1996]. All numbers are for zero water vapor pressure, $p_w = 0$. Increasing water vapor pressure to $p_w = p_s$ increases the astrometric effect by a factor of roughly 20%.

often have very different colors. A PTI upgrade to install dispersion compensators is planned for summer 2005 to address this noise source.

2.4.2.2 Baseline Errors

The baseline vector used in the differential delay equation to determine astrometric quantities is derived by inversion of the delay equation from the fringe locations of point-like sources with known global astrometric positions. Uncertainties and variability of the baseline vector are sources of differential astrometry uncertainties via the differential delay equation. An incorrect baseline model would show up as an hour-angle dependent error term that would potentially increase night-to-night scatter beyond that predicted by the formal uncertainties; this is easily tested by dividing data sets within single nights into multiple sets by hour angle range and comparing results, as in Figure 2-12.

No evidence of hour-angle dependent error terms is seen in the PHASES data, supporting evidence that the baseline models are correct. As shown in Figure 2-8, except for a few outliers (likely due to using point sources with poor global astrometry values or a night's observation only covering a small range of hour angles or declinations) the night-to-night drift in baseline model solutions are less than 1 mm in North-South and East-West directions for the two baselines used for PHASES observations (NS and SW baselines; the NW baseline is not used). The Up-Down dimension is stable to a few millimeters in both cases; this scatter is likely due to limited measurement precision rather than actual baseline variability, implying that it can be improved by averaging several nights' values.

The amount by which a baseline error of $\overrightarrow{\sigma_B}$ affects a differential astrometry measurement $\overrightarrow{\Delta S}$ is determined as follows. To maintain the same observed differential delay between stars, the differential delay equation requires that

$$\overrightarrow{B} \cdot \overrightarrow{\Delta S} = \left(\overrightarrow{B} + \overrightarrow{\sigma_B}\right) \cdot \left(\overrightarrow{\Delta S} + \overrightarrow{\sigma_{\Delta S}}\right) \tag{2.15}$$

where $\overrightarrow{\sigma_{\Delta S}}$ is the astrometric error caused by baseline error $\overrightarrow{\sigma_B}$. Canceling like terms and assuming $\overrightarrow{\sigma_{\Delta S}} \cdot \overrightarrow{\sigma_B}$ is less than the other terms simplifies this to

$$\overrightarrow{\sigma_B} \cdot \overrightarrow{\Delta S} = -\overrightarrow{B} \cdot \overrightarrow{\sigma_{\Delta S}}. \tag{2.16}$$

The vector $\overrightarrow{\Delta S}$ is tangent to the celestial sphere; only that component which is not perpendicular to the baseline is actually measured (this measured component of the separation is referred to as δS) and only its uncertainty ($\sigma_{\delta S}$) is thus applicable. The angle between these measured components and the baseline vector is given by the target's zenith angle z; this is always kept to less than 45 degrees. Of course, the baseline uncertainty vector $\overrightarrow{\sigma_B}$ need not be oriented with $\overrightarrow{B}$ itself; its components σ_{Bx} and σ_{By} tangent to and σ_{Bz} normal to the Earth (also referred to as the "U" component) are introduced. Substituting into eq. 2.16 gives the relationship between baseline error an astrometric error as

$$\delta S \left((\sigma_{Bx} \cos\phi + \sigma_{By} \sin\phi) \cos z + \sigma_{Bz} \sin z \right) = -\left|B\right| \sigma_{\delta S} \cos z \tag{2.17}$$

where ϕ is an angle determined by the hour angle and declination of the target. On rearranging terms, the fractional astrometric measurement uncertainty due to baseline uncertainties is

$$\frac{\sigma_{\delta S}}{\delta S} = -\frac{\sigma_{Bx} \cos\phi + \sigma_{By} \sin\phi + \sigma_{Bz} \tan z}{|B|}. \tag{2.18}$$

For $|B| = 100$ meters and $z < 45$ degrees, baseline uncertainties of 2 mm cause 10 μas errors in a the astrometry for a binary with projected separation $\delta S = 0.5$ arcseconds. Though the measured component of ΔS continually varies as the Earth rotates the baseline vector, the above derivation is true at any given instant. Earth rotation causes errors to appear in both astrometric dimensions.

2.4.2.3 Fringe Template

Because the astrometric measurement is differential between the two stars, it is relatively insensitive to the model fringe template. The fringe model used in the astrometric analysis was determined by observing interferograms of single stars. An effective bandpass was constructed from an incoherent averaging of the periodograms of many such interferograms, and applied to the data. This effective bandpass is only an approximation for most stars, as there are variations in source temperature and spectra. However, reanalysis with several different fringe models shows variations only at the single μas level.

2.4.2.4 Scan Rate and Earth Rotation

Earth rotation causes variable projection of the binary separation on the interferometer baseline vector. The details of the variability depend of the observatory location, sky position of the target binary, and the orientation of the baseline vector, but for order-of-magnitude estimations, can be approximated as a sinusoid with period

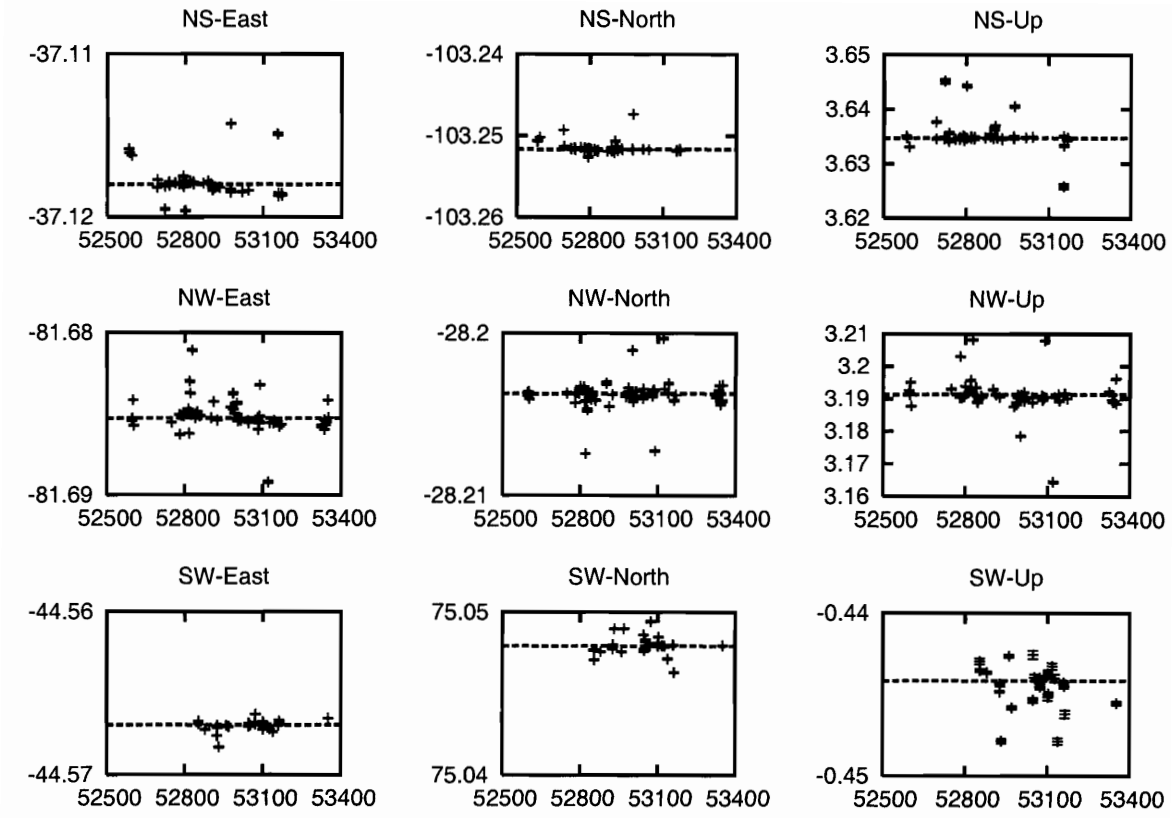

Figure 2-8: Solutions for the three PTI baseline vectors. The three baselines at PTI are named "NS", "NW", and "SW" due to their rough orientations. Each is a three dimensional vector, which is given by components in the "East" (East-West), "North" (North-South), and "Up" (Up-Down) directions (the first two are tangent to the Earth, the last is perpendicular). Horizontal axes are time in Modified Julian Days (MJD), vertical axes is baseline length in meters. Lines represent average baseline fits used for data reduction presented in this thesis; point with error bars represent a given night's baseline solution. The baseline solutions are derived from the observed delay positions of single-star sources with known global astrometric positions via inversion of equation 2.2. The y-axis tic marks in each plot are all 10 mm. Note that the scatter in the "Up" dimension is much larger than the other dimensions; this is due to preferential observing of targets overhead. The baseline solution used for data analysis was a weighted average of the solutions plotted. Note also that the "NW" baseline was not used for data presented in this thesis.

of one day and amplitude equal to the total binary separation (assumed to be 500 milli-arcseconds):

$$\Delta s \approx 500\,\mathrm{mas} \times \cos\left(2\pi t/\mathrm{day}\right). \tag{2.19}$$

The differential delay rate is given by the first derivative of this equation with respect to time, converted from sky angle to delay length by the interferometer's resolution. This differential delay rate is about 20 nm per second, or 5 nm (10 μas) in the (typically) 250 milliseconds required to scan between the fringe packets. Roughly an equal number of scans are obtained in each scan direction (to within 10%), and this effect cancels to first order (to the same level, 10% or 1 μas). However, curvature in the differential delay motion does not cancel; it is given by the second time derivative of the projected separation and is roughly $1.4 \times 10^{-3}\,\mathrm{nm\,s^{-2}}$ (less than 3 nano-arcseconds per square second). Thus the differential delay rate is small enough, and the measurement rate fast enough, that the finite measurement rate does not contribute significant uncertainties.

2.4.2.5 Beam Walk

The interferometer telescopes image a sky field and then recollimate the beam into a pupil plane. Through this process, light from two stars separated on the sky by angle α will be partially sheared with respect to each other and will proceed to illuminate slightly different parts of the optics that guide the light to the detector. Starlight in a recollimated beam that originated from different sky positions will also develop relative shear equal to the path travelled multiplied by their angular separation (see Figure 2-9). To the extent that the optics are imperfect (i.e. have rough surfaces), the light from each star will travel slightly different path-lengths from telescope to detector. This process is known as beam walk.

Colavita [1998] has determined the extent to which beam walk introduces astrometric errors. These calculations are reviewed here.

The surface qualities of mirrors can be defined by measuring the power spectra $W(f)$ of their surface deviations $z(r)$ from perfectly flat. The power spectra can be modeled as by a power law

$$W\left(f\right) = k^2 f^{-a}, f > f_c \tag{2.20}$$

with f the spatial frequency in cycles across the optic and f_c a cutoff frequency (necessary for normalization) defined such that half of the wavefront variance is above that frequency. The total wavefront variance over the optic is w^2, which is determined by

$$w^2/2 = 2\pi \int_{f_c}^{\infty} W\left(f\right) f \mathrm{d}f \tag{2.21}$$

which evaluates to

$$k^2 = \frac{a-2}{4\pi} f_c^{a-2} w^2. \tag{2.22}$$

Typical values are $f_c = 1$, $a = 2.5$; the optics at PTI have quality $w = \lambda_r/20$ (evaluated at $\lambda_r = 633$ nanometers).

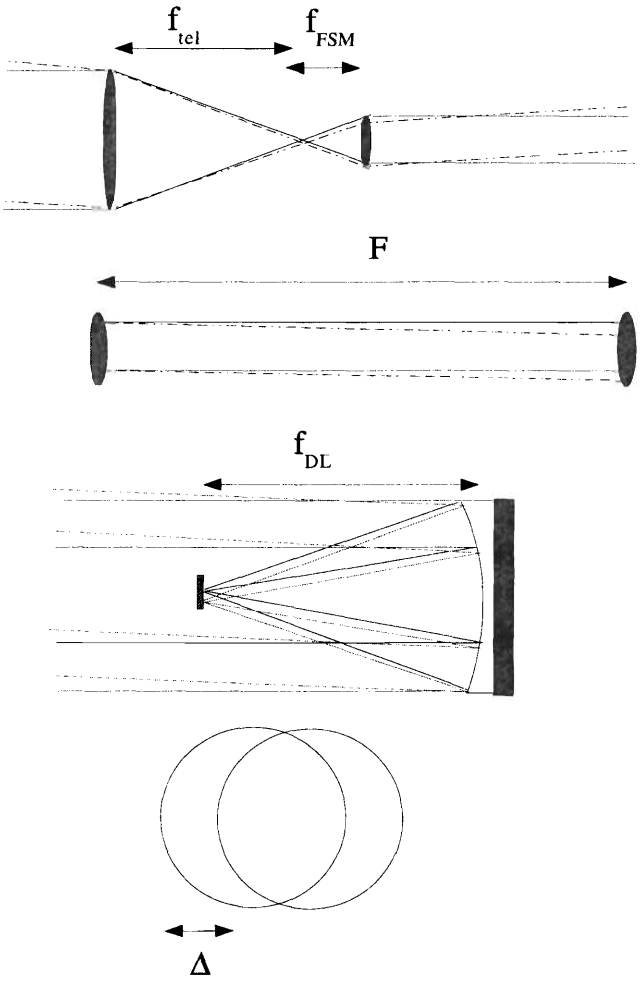

Figure 2-9: Three instances where beam walk can occur, causing stars at slightly different sky angles to illuminate different parts of optical elements.
(top) Shear introduced at the telescope by focusing and recollimating the beam. "FSM" stands for the "Fast Steering Mirror", which provides tip-tilt (first-order adaptive optics) corrections and recollimates the light after the telescope.
(second from top) Shear within a collimated beam over large optical paths.
(second from bottom) Shear at focus of delay line optics (DL, the movable mirrors that provide optical delays).
(bottom) The shear of two beams by amount Δ, causing only partial overlap.

The shear of two equal sized beams (e.g. the light from two stars) illuminating an optic gives an average differential longitudinal path ϵ given by their overlap integral across the optic. Define the relative diameters of the starlight beams to the optic as D (with relative area $A = \pi D^2/4$), and the ratio of the size of the shear to the optic as Δ.

$$\epsilon^2 = \left\langle \left(\frac{1}{A} \int z\left(\vec{r}\right) \mathrm{d}\vec{r} - \frac{1}{A} \int z\left(\vec{r} + \vec{\Delta}\right) \mathrm{d}\vec{r} \right)^2 \right\rangle \tag{2.23}$$

$$= \left\langle \left(\frac{1}{A} \int\int e^{-i2\pi \vec{f}\cdot\vec{r}} \mathrm{d}W\left(\vec{f}\right) \mathrm{d}\vec{r} - \frac{1}{A} \int\int e^{-i2\pi \vec{f}\cdot\left(\vec{r}+\vec{\Delta}\right)} \mathrm{d}W\left(\vec{f}\right) \mathrm{d}\vec{r} \right)^2 \right\rangle$$

$$= \left\langle \left(\frac{1}{A} \int \left(1 - e^{-i2\pi \vec{f}\cdot\vec{\Delta}}\right) \int e^{-i2\pi \vec{f}\cdot\vec{r}} \mathrm{d}\vec{r} \mathrm{d}W\left(\vec{f}\right) \right)^2 \right\rangle$$

$$= \left\langle \left(\int \left(1 - e^{-i2\pi \vec{f}\cdot\vec{\Delta}}\right) \frac{2J_1\left(\pi f D\right)}{\pi f D} \mathrm{d}W\left(\vec{f}\right) \right)^2 \right\rangle$$

$$= 2 \int \left(1 - \cos\left(2\pi \vec{f}\cdot\vec{\Delta}\right)\right) \left(\frac{2J_1\left(\pi f D\right)}{\pi f D} \right)^2 W\left(\vec{f}\right) \mathrm{d}f$$

$$= 4\pi \int \left(1 - J_0\left(2\pi f \Delta\right)\right) \left(\frac{2J_1\left(\pi f D\right)}{\pi f D} \right)^2 W\left(f\right) f \mathrm{d}f \tag{2.24}$$

$$\approx 4\pi \int_0^{1/D} k^2 f^{-1.5} \left(2\Delta f\right)^2 \mathrm{d}f \tag{2.25}$$

$$\approx 34 k^2 \Delta^2 D^{-1.5} \tag{2.26}$$

$$\approx 1.3 w^2 \Delta^2 D^{-1.5} \tag{2.27}$$

where $f_c = 1$ and $a = 2.5$ are assumed in the final three simplifications. The final two versions assume $\Delta << D$.

The first place where beam walk may occur is within the telescope itself. The beam is collimated at the telescope primary, focused by the primary, and recollimated to a 0.075 m beam by the 0.1 m diameter ($D = 0.75$) "Fast Steering Mirror" (FSM; this mirror corrects for tip-tilt wavefront errors across the telescope (low-order adaptive optics)). The distance from primary mirror to the FSM is the sum of their focal lengths, 4.75 m. The beam walk over 0.1 arcsecond (4.8×10^{-7} radians) is thus 2.3 μm, and $\Delta = 2.3 \times 10^{-5}$. Beam walk on the FSM thus contributes an astrometric error of 0.002 μas.

The relative angles of starlight in the recollimated beam are increased by a factor of the ratio of the primary mirror and FSM focal lengths (5.33), thus light from sky locations separated by 0.1 arcseconds has a differential angle of 0.533 arcseconds (2.6×10^{-6} radians). This recollimated beam from the FSM travels through light pipes to the beam combining laboratory, where movable mirrors add a variable amount of delay. This total travel is of order 50 meters; the mirrors are typically 0.1m diameter ($D = 0.75$). The beam walk over 0.533 arcseconds is 130 μm ($\Delta = 1.3 \times 10^{-3}$), which contributes an astrometric error of 0.13 μas. There are a few mirrors along this path, and the total astrometric error would be determined by considering the optical

qualities of all optics and adding the effects in quadrature. Because this beam walk is so small, the sum total of these remains negligible.

The movable mirrors are comprised of a parabolic mirror of focal length 1.07 m and a small (≈ 0.01 m) flat mirror located at its focus. Collimated light is directed to one side of the parabola, focused onto the flat mirror, then recollimated by the parabola's other side. On the flat mirror, the (diffraction-limited) beam diameter is only $2.44\lambda f/d = 77\,\mu$m ($D = 0.0077$), where λ is the operating wavelength of light, f is the parabola's focal length, and d is the collimated beam diameter (0.075 m). The beam walk is $2.8\,\mu$m ($\Delta = 2.8 \times 10^{-4}$). The flat mirror contributes an astrometric error of 0.16 μas from beam walk. It is concluded that beam walk does not contribute significant measurement errors.

2.4.2.6 Global Astrometry Errors

Uncertainty in the global position of a target binary on the celestial sphere couples into the differential astrometric measurement. Errors in right ascension are equivalent to measurement timing errors; declination uncertainties have similar effects. The order of magnitude of this effect can be derived as follows: the fractional error in global astrometry (error in arcseconds divided by total number of arcseconds in a sphere) is roughly equal to the fractional error in differential astrometry separation vector (astrometric error divided by binary separation). A one arcsecond global astrometry error causes differential astrometric errors of less than one μas for binaries of separation one arcsecond or less. Typical uncertainties in global astrometry are much less than an arcsecond, with 10 milli-arcseconds being a much more common value. Effects such as stellar aberration (20 arcseconds) are accounted for in the PHASES data reduction software; if ignored, these could cause significant differential astrometry uncertainties.

2.4.3 Astrophysical Noise

There are potential sources of apparent astrometric motion in the target stars that are not due to unseen companions but rather to processes within the stars themselves. These include star spots and stellar granulation.

2.4.3.1 Star spots

The maximum shift in the center-of-light of a star caused by star spots are evaluated with a model comprised of a uniform stellar disk (radius R) except for a zero-temperature (non-emitting) circular region of radius r tangent to the edge of the stellar disk (i.e. centered at $x = R - r$, $y = 0$). The center of light is displaced by:

$$\begin{aligned} \frac{x_c}{R} &= \frac{\int_{-R}^{R}\int_{-\sqrt{R^2-x^2}}^{\sqrt{R^2-x^2}} x\mathrm{d}y\mathrm{d}x - \int_{R-2r}^{R}\int_{-\sqrt{r^2-(x-R+r)^2}}^{\sqrt{r^2-(x-R+r)^2}} x\mathrm{d}y\mathrm{d}x}{R\pi\left(R^2-r^2\right)} \\ &= -\frac{r^2/R^2}{1+r/R}. \end{aligned} \tag{2.28}$$

The presence of star spots can be confirmed through photometric measurements simultaneous with astrometric observations. The non-emitting spots in this model would cause photometric variations proportional to the fractional area of the stellar disk covered:

$$\frac{F}{F_o} = 1 - \frac{r^2}{R^2} \tag{2.29}$$

where F_o is the star's flux when no spots are present. Equations 2.28 and 2.29 provide a relationship between the apparent astrometric and photometric shifts caused by star spots.

The largest possible astrometric shift by a star spot is given by evaluating a slightly different model. In this case, the star spot fills the (non-circular) area from the star's edge to a chord at distance x_o from the star's true center. The astrometric shift is

$$\begin{aligned} \frac{x_c}{R} &= \frac{\int_{-R}^{x_o} \int_{-\sqrt{R^2-x^2}}^{\sqrt{R^2-x^2}} x \mathrm{d}y\mathrm{d}x}{R \int_{-R}^{x_o} \int_{-\sqrt{R^2-x^2}}^{\sqrt{R^2-x^2}} \mathrm{d}y\mathrm{d}x} \\ &= -\frac{2\left(1-\frac{x_o^2}{R^2}\right)^{3/2}}{3\left(\frac{\pi}{2} + \arcsin\frac{x_o}{R} + \frac{x_o}{R}\left(1-\frac{x_o^2}{R^2}\right)^{1/2}\right)} \end{aligned} \tag{2.30}$$

with corresponding photometric variations of

$$\frac{F}{F_o} = \frac{1}{\pi}\left(\frac{\pi}{2} + \arcsin\frac{x_o}{R} + \frac{x_o}{R}\left(1-\frac{x_o^2}{R^2}\right)^{1/2}\right). \tag{2.31}$$

For stars of typical radius 1 milli-arcsecond, the simplified model gives a roughly linear relationship of 0.8 micro-arcsecond of astrometric shift per milli-magnitude of photometric variability. Photometric variations of these scales can be monitored by small ground-based telescopes. The timescale of these variations is on order the rotation rate of a star (days to weeks).

2.4.3.2 Stellar Granulation

Stellar granulation causes photometric variability of subsections of a star's surface. Averaged over the whole of the stars surface, these photometric variations can cancel to large extent and the intrinsic variability of the star remain small, though with a large astrometric uncertainty. Svensson and Ludwig [2004] showed that the effects of stellar granulation are independent of a star's radius but are strongly correlated with surface gravity, and provide values for the astrometric effects in white light.

For stars with very low surface gravities (i.e. red giants), astrometric perturbations can be quite large—as much as $300\,\mu\mathrm{as}/D\,[\mathrm{pc}]$. Red giants within 100 parsecs are overresolved by PTI and cannot be observed, thus even for these stars this effect is negligible. For main sequence stars, the effect is closer to $0.1\,\mu\mathrm{as}/D\,[\mathrm{pc}]$.

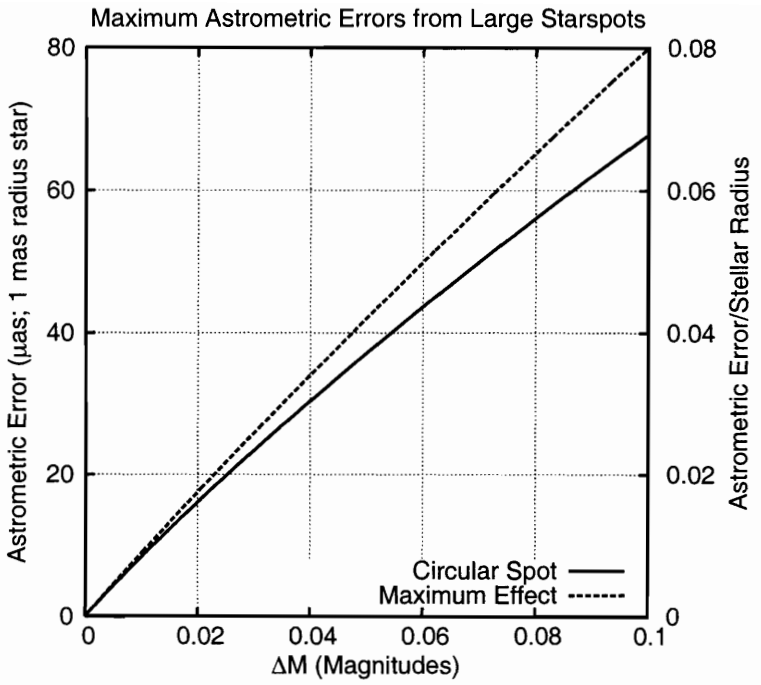

Figure 2-10: The maximum effect of star spots on astrometric measurements versus the photometric variations they cause.

2.5 Demonstrated Performance

2.5.1 Intranight Repeatability

Intranight repeatability was explored by dividing each night's data sets into subsets and comparing the astrometric fits. The subsets were analyzed with the standard data reduction pipeline, again keeping only those for which only one maximum in the likelihood function is found at the formal uncertainty 4σ level (this requirement is met less often for these subsets as there are less data to remove the fringe ambiguity). Two methods of dividing a night's measurements were explored: first, the scans were grouped by even and odd numbered scans (creating two interwoven data sets), second, the scans were divided in half by hour angle (creating two back-to-back data sets). Three target systems were tested in each case. Note that dividing the scans by odd- and even-numberings does not have the effect of dividing the scans by scan direction—on occasion scans are skipped due to low SNR or loss of fringe lock by the phase-referencing beam combiner, which serves to randomize the scan directions between the even and odd sets.

The distributions of the χ^2-determined probability of agreement for the interwoven subsets are shown in Figure 2-11; those for the hour-angle divided sets are in Figure 2-12. The one-sided Kolmogorov-Smirnov (K-S) significance probability for the subsets agreeing on intranight timescales are given in Table 2.3. The distribution of values for this K-S metric show the astrometric quantities determined from the subsets agree at the level expected by their formal uncertainties, and the data scatter is consistent

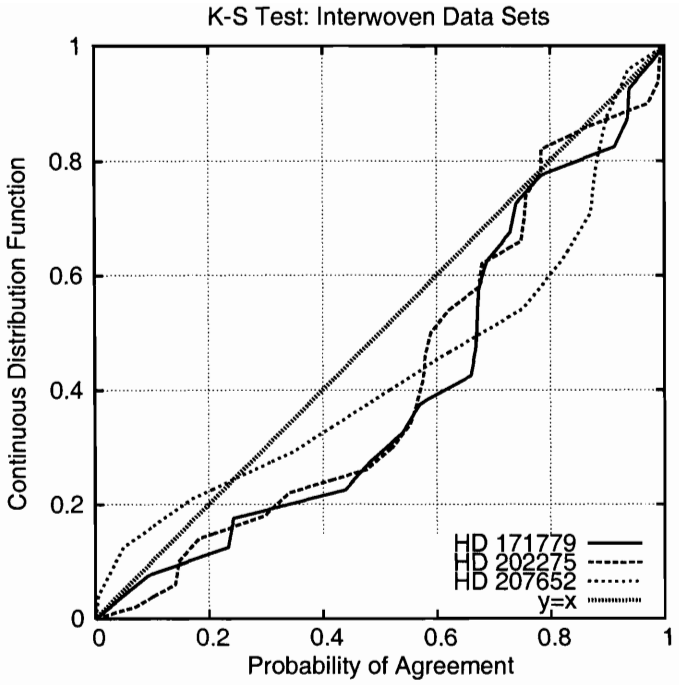

Figure 2-11: K-S test to detect intranight scatter beyond that predicted by the formal measurement uncertainties. Each night's data set was divided into two subsets each with half the scans of the night, and the fits' results compared with χ^2 metric. In this test, the subsets were interwoven—odd numbered scans were evaluated separately from even numbered scans.

on intranight timescales.

2.5.2 Distributions of Delay Residuals

As previously mentioned, the signal-to-noise ratio of any individual scan is too low to allow for unique identification of the projected separations of the two stars—χ^2 model fitting of fringe packets for two stars has multiple local minima separated by the fringe spacing and the correct global minima is only determined through evaluating many scans. After each data set has been analyzed, each scan's χ^2 fit can be reevaluated for projected separations within one wavelength of that predicted by the best-fit astrometric solution. The minimum point of this limited-domain χ^2 function (which is also the "correct" global minimum) is found and its distance from the best-fit predicted projected separation is recorded. In this way the scatter in the basic observable (the differential delays) is recovered on a scan-by-scan basis. These delay residuals appear to be Gaussian-distributed with average standard deviation of $180 \pm 10\,\mathrm{nm\,scan}^{-\frac{1}{2}}$, corresponding to a 3 nm = 6 μas uncertainty over an hour integration ($\approx$ 3600 scans). This agrees well with the formal uncertainties determined by the standard data reduction algorithm.

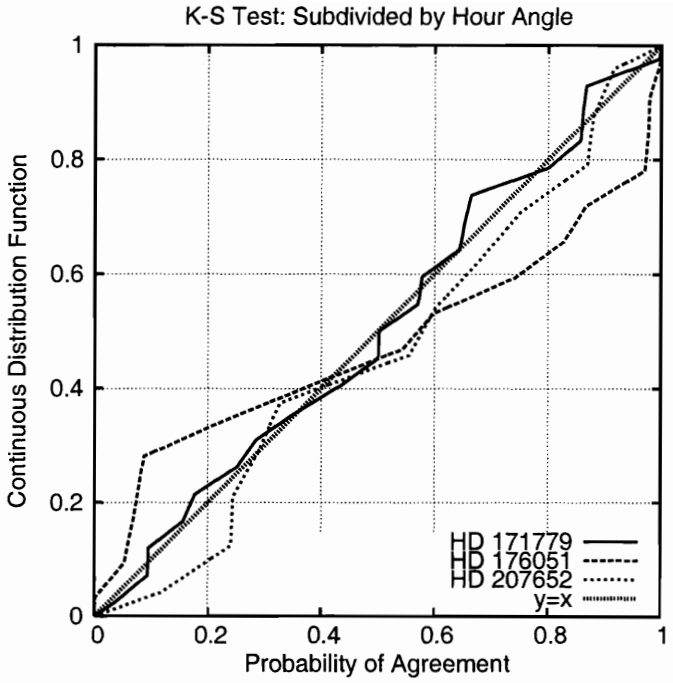

Figure 2-12: K-S test to detect intranight scatter beyond that predicted by the formal measurement uncertainties. Each night's data set was divided into two subsets each with half the scans of the night, and the fits' results compared with χ^2 metric. In this test, the subsets were divided by hour angle—the first half of a night's scans for a given target were evaluated separately from the second half of the scans. Note that even for HD 176051, which does have an appreciable color difference between primary (G0V) and secondary (K1V) (for which differential dispersion may introduce scatter), the fits agree to within the formal uncertainties.

Table 2.3
Kolmogorov-Smirnov Probability of Agreement

Star	Even-Odd Subsets	Hour-Angle Based Subsets
HD 171779	0.1885	0.9998
HR 176051		0.5341
HD 202275	0.1458	
HD 207652	0.6110	0.9943

Table 2.3: K-S test to detect intranight scatter beyond that predicated by the formal uncertainties. A night's observation was subdivided into two subsets in one of two ways: first, the scans were grouped by even and odd numbered scans (creating two interwoven data sets), second, the scans were divided in half by hour angle (creating two back-to-back data sets). In each case, three target systems were chosen for analysis in this manner. The K-S probability of agreement is shown for each set (values range from zero to one, low values indicate the subsets do not agree within the formal uncertainties).

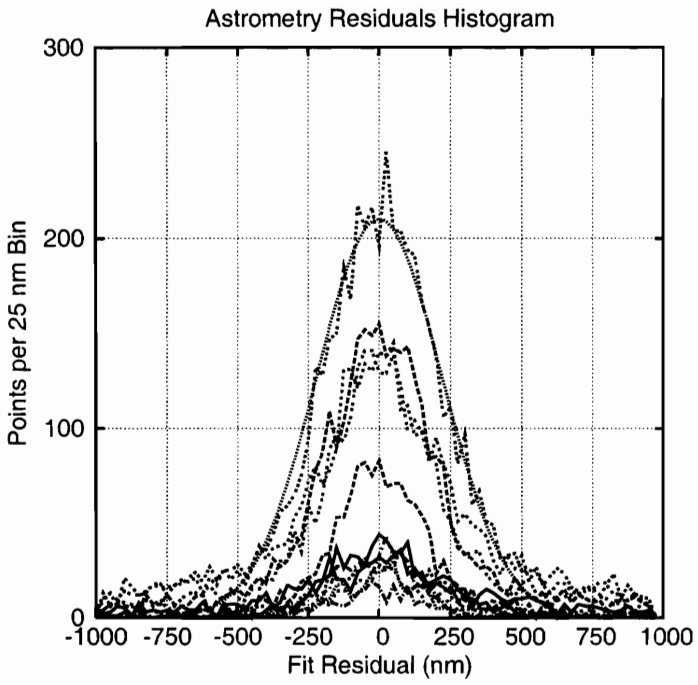

Figure 2-13: Histograms of differential delay model residuals on a scan-by-scan basis for several nights of data on multiple binaries. One nm corresponds to roughly 2.1 micro-arcseconds; each histogram contains on order 2000 scans. Also plotted is a best-fit Gaussian distribution for the histogram with the most scans.

2.5.3 Allan Variances

Though histograms of delay-model residuals show the differential-delay measurements are Gaussian-distributed, if the measurements are correlated with each other the number of independent measurements would be over-estimated and the formal uncertainties underestimated (for example, an unmonitored change in delay path at frequencies lower than the scan rate could cause correlations between successive scans). The Allan variance is a statistical quantity to determine the degree of correlation between measurements within a data set [cf. Thompson et al., 2001]. It is calculated by comparing a data set with a time-lagged version of itself. The Allan variance σ_A^2 at lag k scans is

$$\sigma_A^2(k) = \frac{1}{2(N+1-k)} \sum_{n=0}^{N-2k} \left(\frac{1}{k} \sum_{m=0}^{k-1} y_{m+n} - y_{k+m+n} \right)^2 \tag{2.32}$$

where N is the total number of scans and y_i is the residual model separation for scan i (these are the same residuals used to make the histograms in Figure 2-13. The Allan variance of a data set with white (uncorrelated) noise decreases as $\sqrt{k}$. No correlations are seen in the Allan variances—the noise is white over all statistically-significant lag intervals.

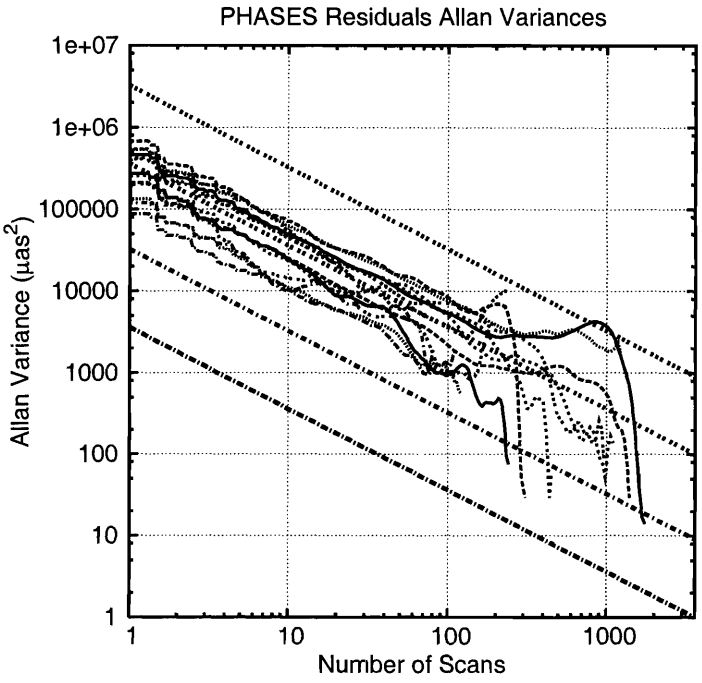

Figure 2-14: Allan variances of differential delay model residuals, plotted versus number of scans, for several nights of data on multiple binaries. The model lines show the expected Allan variances for uncorrelated measurements that yield precisions of 1, 3, 10, and 30 micro-arcseconds in an hour of observation ($\approx$ 3600 scans).

2.5.4 Internight Repeatability

At the level of precision of these differential astrometry measurements, orbital evolution of the target binary systems is measurable on timescales of days. Thirty-six binaries have been observed with this mode, eighteen of which have been observed six or more times and have also not previously been identified as having more than two stellar components (see Table 2.4). Orbital models consisting of low-order polynomials or Keplerian orbits (whichever model fit best was used) were fit to the differential astrometry for these eighteen binaries. These fits show scatter beyond the formal astrometric uncertainties on internight timescales. The median factor of disagreement between the single-night (formal) uncertainties ($\sim 10\mu$as) and night-to-night fits is found to be 3.32 ($\sim 33\mu$as).

While the cause of this disagreement has been identified as occurring on timescales on order of a day, the source itself has not yet been identified. Figure 2-15 indicates possible slight correlations between the excess scatter and both differential magnitude and sky separation. Differential magnitude is generally related to differential color for stars of similar evolutionary state; this correlation may indicate differential dispersion is indeed contributing to excess scatter.

The slight correlation with sky separation may be related to a complicated coupling of longitudinal and lateral dispersions. Longitudal dispersion is due to differences in the air path between the arms of the interferometer; resulting in color-

dependent solutions to the delay equation, eq. 2.2. Lateral dispersion (i.e. in a direction perpendicular to the beam path) can be introduced by imperfect optics that act as prisms by some (small) amount, introducing color-dependent lateral shifts at the detector. Because light from the two stars in the binary only partially overlap on the detector pixel, the portion of the (laterally dispersed) light which is sampled by the pixel will differ, the stars will appear to be of different colors, and errors similar to those from differential dispersion will occur (note that no error occurs if the longitudinal dispersion is zero). This effect varies with binary separation.

A dispersion compensator upgrade for PTI is being developed for summer 2005 to correct the variations in longitudinal dispersion. It is anticipated that this upgrade will remove the correlations between the night-to-night repeatability and differential color and sky separations.

Table 2.4
PHASES Sources: Internight repeatability

HD Number	$\sqrt{\chi^2_r}$	$\sigma_{\rm min}$	$\sigma_{\rm maj}$	$\sqrt{\chi^2_r} \times \sigma_{\rm min}$	$\sqrt{\chi^2_r} \times \sigma_{\rm maj}$	Primary Spectral Type	K	V	ΔK	$N_{\rm obs}$	Span (days)	$N_{\rm scans}$
13872	1.4	16.8	417.5	23.7	588.7	F6 V	4.4	5.6	0.144	14	472	905
207652	1.4	8.8	177.8	12.8	257.8	F2 III-IV	3.5	5.3	0.460	15	142	1427
44926	1.6	7.2	208.2	11.4	328.9	K1 III	4.1	6.6	0.152	8	361	1788
17904	1.8	21.0	393.6	38.5	720.2	F4 Vvar	4.3	5.3	1.149	19	465	821
140159	1.9	14.9	420.8	28.3	799.5	A1 V	4.4	4.5		6	104	581
114378	2.0	13.9	370.5	27.8	741.0	F5 V	3.2	4.3		9	459	401
77327	2.2	10.3	202.4	22.4	439.2	A1 Vn	3.5	3.6		13	493	789
137107	2.8	10.2	280.9	28.8	792.1	G2 V	3.5	5.0	0.191	13	399	866
171779	3.0	9.5	180.1	27.9	531.2	K0 III	2.8	5.3	0.170	23	442	1190
196524	3.3	12.7	371.3	42.0	1232.6	F5 IV	2.6	4.1	1.093	14	590	1258
140436	3.6	7.8	256.9	28.3	932.5	A1 Vs	3.7	3.8	0.966	9	384	1847
202275	3.8	7.1	165.6	26.9	629.2	F5 V	3.3	5.0	0.065	28	612	1391
5286	5.3	13.0	274.4	68.4	1443.6	K1 IV	3.1	6.5	0.459	9	356	790
176051	5.3	13.6	337.3	72.5	1801.4	G0 V	3.8	5.2	1.338	22	616	1386
202444	6.8	12.3	556.4	84.3	3806.0	F1 IV	2.7	4.1		8	77	2646
6811	7.7	19.6	375.8	149.8	2874.8	B7 III	1.3	4.2	1.434	9	418	936
221673	17.5	5.8	49.4	101.0	863.0	K4 III	1.8	5.0	0.560	53	478	2267
60318	17.8	3.7	66.0	66.4	1175.0	K0 III	3.0	5.3		12	524	3366

Table 2.4: Internight repeatability for the eighteen PHASES sources observed six or more times and are not already known to contain spectroscopic subsystems. It is possible the last two stars (K giants HD 221673 and HD 60318) have short period stellar companions not previously discovered; Differential dispersion effects are expected to be particularly large for HD 176051, HD 6811, and HD 221673.

While the night-to-night agreement is not yet at the level of the intranight uncertainties, it is at the precision required to find Jupiter mass companions to these binary systems. Three years of additional funding for PTI operations has recently been granted by NASA for continued operation of the PHASES differential astrometry program, beginning in 2005; this should allow enough time coverage of PHASES targets to allow detection of planets, should they exist. The two years of PHASES observations thus far completed are not yet enough for a planet-finding campaign, but do allow detailed studies on several of the binary systems themselves. Three of these systems are discussed in chapters 3, 4, and 5.

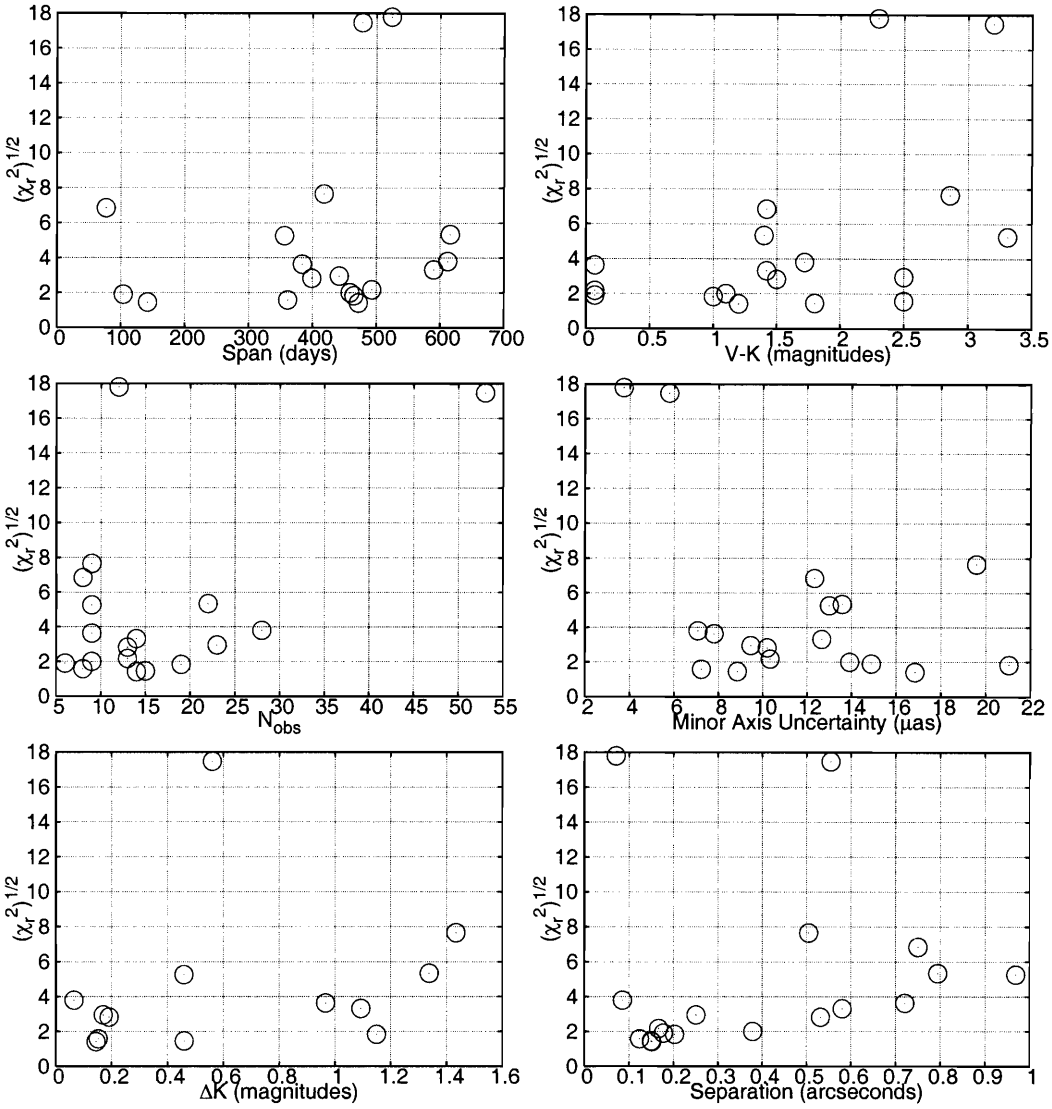

Figure 2-15: Scale factor $\sqrt{\chi_r^2}$ of disagreement between the intranight uncertainties and night-to-night repeatability plotted versus six quantities that vary between targets. Only those eighteen systems for which six or more observations have been made and that are not previously known to contain spectroscopic subsystems are plotted. The values of $\sqrt{\chi_r^2} \approx 18$ for HD 221673 and HD 60318 are outliers and may be evidence of previously unknown short period subsystems; alternatively, these two binaries have the smallest formal uncertainties and these might indicate a noise floor due to systematic error sources such as baseline measurement. (Top Left) Span in days of the observations. (Top Right) $V - K$ color. (Middle Left) Number of observations. (Middle Right) Median value of intranight uncertainty ellipse minor axis. (Bottom Left) Differential magnitude between binary components; this quantity is generally related to color difference for stars of similar evolutionary state. For 5 systems, K-band differential magnitudes are not available. (Bottom Right) Median sky separation. No strong correlations are observed, though slight correlations of $\sqrt{\chi_r^2}$ with differential magnitude and separation are observed. It is possible that more than one effect is causing the excess scatter, each contributing differently to various systems.

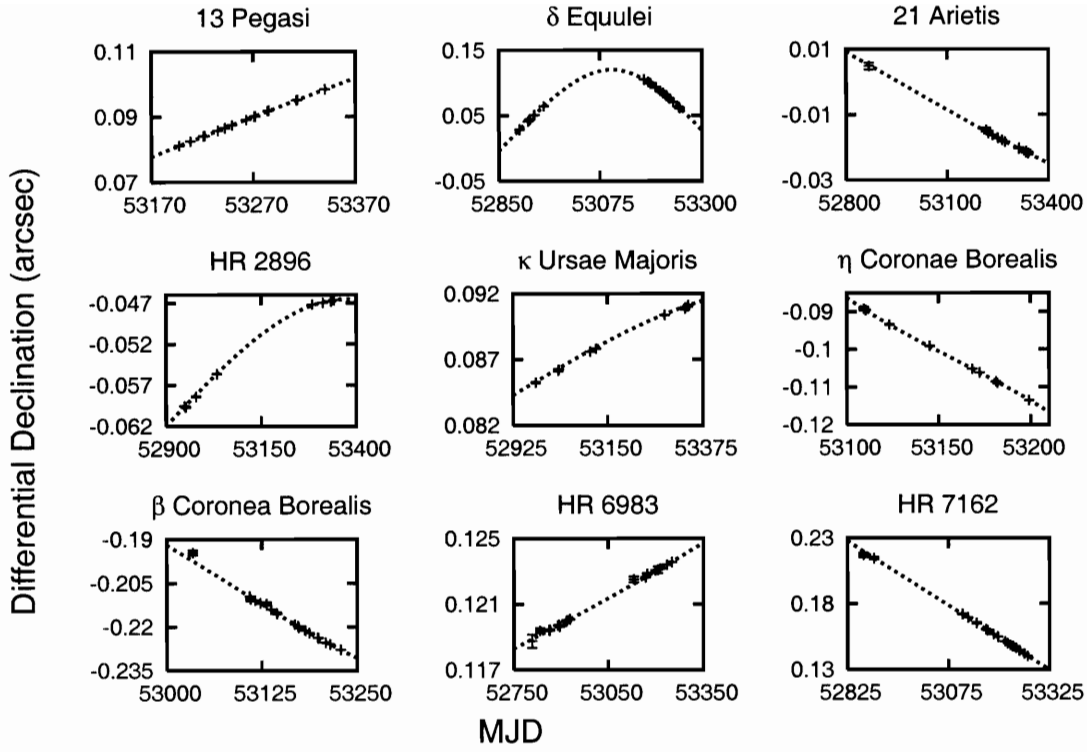

Figure 2-16: Nine PHASES targets observed over multiple nights, showing night-to-night orbital motion of the binary systems. Because the North-South oriented baseline has been used for the majority of the observations, the differential declination direction is generally closely aligned to the minor axis of the differential astrometry error ellipse. Scatter about the orbital models is typically of order 3 times larger than the formal uncertainties.

Chapter 3

PHASES High Precision Differential Astrometry of δ Equulei

δ Equulei is among the most well-studied nearby binary star systems. Results of its observation have been applied to a wide range of fundamental studies of binary systems and stellar astrophysics. It is widely used to calibrate and constrain theoretical models of the physics of stars. Twenty-seven high precision differential astrometry measurements of δ Equulei from PHASES have been made. The median size of the minor axes of the uncertainty ellipses for these measurements is 26 micro-arcseconds (μas). These data are combined with previously published radial velocity data and other previously published differential astrometry measurements using other techniques to produce a combined model for the system orbit. The distance to the system is determined to within a twentieth of a parsec and the component masses are determined at the level of a percent. The constraints on masses and distance are limited by the precisions of the radial velocity data; plans to improve this deficiency and the outlook for further study of this binary are outlined.

The contents of this chapter have been submitted to the *Astronomical Journal* for publication with authors Matthew W. Muterspaugh, Benjamin F. Lane, Maciej Konacki, Bernard F. Burke, M. M. Colavita, S. R. Kulkarni, and M. Shao.

3.1 Introduction

The study of δ Equulei as a binary star has lasted nearly 200 years. In the early 1800s, William Herschel's (mistaken) listing of it as a wide binary (with what Friedrich Struve later proved to be an unrelated background star) brought it to the attention of many astronomers. While making follow-up observations to support his father's claim that the proposed pair were only an optical double, Otto Wilhelm von Struve in 1852 found that while the separation of the optical double continued to grow (to 32"), the point-spread-function of δ Equulei itself appeared elongated. He concluded that δ Equulei itself is a much more compact binary. (It is perhaps interesting to

note that the Struve family's study of the system continued through 1955, when Otto Struve and K. L. Franklin included the system in a spectroscopic study.)

δ Equulei (7 Equulei, HR 8123, HIP 104858, HD 202275, ADS 14773) is among the most well-studied nearby binary star systems. It is particularly useful to studies of binary systems and stellar properties as it is close ($d = 18.4$ pc), bright ($V = 4.49$, $K = 3.27$), and can be studied both visually (semi-major axis roughly a quarter of an arcsecond) and spectroscopically (spectral classes F7V+F7V, $K \approx 12.5$ km s^{-1}) in a reasonable amount of time ($P \approx 5.7$ years); Mazeh et al. [1992] found only 23 binaries within 22 pc with periods less than 3000 days and spectra that were nearly solar (spanning types F7-G9, classes IV-V, V, and VI). As such, it is regularly included in statistical surveys of binary systems [see, for example, Heacox, 1998, Hale, 1994] and fundamental stellar properties such as the mass-luminosity relationship, calibrating photometric parallax scales, tabulating the H-R diagram of the solar neighborhood, and constraining models of stellar atmospheres [see, for example, Lastennet et al., 2002, Eggen, 1998, Castelli et al., 1997, Smalley and Dworetsky, 1995, Boehm, 1989, Habets and Heintze, 1981, Popper, 1980]. These applications depend upon accurate knowledge of the components' physical properties and the system's parallax.

Previously, the visual orbit models (and thus evaluation of the total system mass and orbital parallax) of δ Equulei have been limited by differential astrometry with relative precisions on order of a few percent. The recently developed method for ground-based differential astrometry at the 10 μas level for sub-arcsecond ("speckle") binaries has been used to study δ Equulei over the 2003-2004 observing seasons. These measurements represent an improvement in precision of over two orders of magnitude over previous work on this system. These new data, an updated three-dimensional model of the system, and the physical properties of the component stars are presented. The observations were taken as part of the Palomar High-precision Astrometric Search for Exoplanet Systems (PHASES).

3.2 Observations and Data Processing

3.2.1 PHASES Observations

δ Equulei was observed with PTI on 27 nights in 2003-2004 using the observing mode described in Lane and Muterspaugh [2004] and in chapter 2 of this thesis. For δ Equulei, the typical scanning rate in 2003 was one scan per second and four intensity measurements per ten milliseconds; these values were doubled in 2004. The typical scan amplitude was 100 microns. An average of 1700 scans were collected each night the star was observed over a time span of 30 to 90 minutes.

The differential astrometry measurements are listed in Table 3.1, in the ICRS 2000.0 reference frame. A Keplerian fit to the PTI data using the formal uncertainties found the minimized value of reduced $\chi^2_r = 14.46$, implying either that the uncertainty estimates are too low by a factor of 3.8 or the (single) Keplerian model is not appropriate for this system. Several possible sources of excess astrometric scatter have been evaluated. The maximum effect of starspots is evaluated as approximately

8 μas of scatter per 10 millimagnitudes of photometric variability, a level not observed in δ Equulei (Hipparcos photometry shows a scatter of only 4 millimagnitudes [van Leeuwen et al., 1997]). The delay lines at PTI are in air rather than vacuum, introducing longitudinal dispersion to the system and color-dependent variations to the points of zero optical delay. Because the components of δ Equulei are equal temperature, this effect cancels in a differential measurement.

The uncertainty values listed in Table 3.1 have been increased by a factor of 3.8 over the formal uncertainties; these increased values are used in fits presented in this paper, in order that this data set can be combined with others. At this time it is found that more complicated models (such as adding additional unseen system components) do not produce better fits to the PTI data. The rescaled (raw) median minor- and major-axis uncertainties are 26 (6.8) and 465 (122) μas. The rescaled (raw) mean minor- and major-axis uncertainties are 35 (9.2) and 1116 (294) μas.

3.2.2 Previous Differential Astrometry Measurements

Previously published differential astrometry measurements made with other methods have been collected. Most of these measurements were tabulated by Hartkopf et al. [2004] in the Fourth Catalog of Interferometric Measurements of Binary Stars, though several additional measurements (particularly those made by micrometer measures) had to be researched from the original sources. In two cases discrepancies between the uncertainties listed in the Fourth Catalog and the original sources were found (the 1977.8811 point by Morgan et al. [1980] and that from 1983.9305 by Bonneau et al. [1984]); in each case the uncertainties listed in the original work are used. Several data points listed without uncertainty estimates in the Fourth Catalog were found to have uncertainty estimates listed in the original works, in which case those values were used.

Most of the previous differential astrometry measurements were published without any associated uncertainties. To allow these to be used in combined fits with other data sets, average uncertainties were determined as follows. The measurements were separated into subgroups by observational method and each set was analyzed individually; the first group included eyepiece and micrometer observations, and the second contained interferometric observations, including speckle, phase-grating, aperture masking, and adaptive optics. The uncertainties were first estimated to be 10 milli-arcseconds in separation and 1 degree in position angle. A Keplerian model was fit to the data, and residuals in separation and position angle treated individually to update the estimates and outliers removed. This procedure was iterated until uncertainties were found consistent with the scatter. The 66 visual data points used have average uncertainties of 37.2 milli-arcseconds in separation and 3.53 degrees. The 58 interferometric data points used have average uncertainties of 5.92 milli-arcseconds and 1.59 degrees.

A Keplerian model was fit to the data points for which uncertainty estimates were available to determine whether these were systematically too large or too small, and to find outliers. Because there were only four visual/micrometer measurements with published uncertainties, these were not treated as a separate group. There

Table 3.1
PHASES data for δ Equulei

JD-2400000.5	δRA (mas)	δDec (mas)	$\sigma_{\rm min}$ (μas)	$\sigma_{\rm maj}$ (μas)	$\phi_{\rm e}$ (deg)	$\sigma_{\rm RA}$ (μas)	$\sigma_{\rm Dec}$ (μas)	$\frac{\sigma^2_{\rm RA,Dec}}{\sigma_{\rm RA}\sigma_{\rm Dec}}$	N
52896.18089	43.1331	28.3054	27.9	279.0	150.13	242.3	141.1	-0.97371	854
52897.15549	42.9731	29.2553	24.0	378.4	146.47	315.7	209.9	-0.99054	1698
52915.20224	46.9142	41.1237	34.8	465.2	163.69	446.6	134.8	-0.96308	885
52917.18203	46.8911	42.6169	15.0	273.3	160.60	257.8	91.8	-0.98499	2197
52918.17180	46.9129	43.3924	26.1	305.1	158.50	284.1	114.4	-0.96945	1181
52920.19763	46.8789	44.7316	37.2	1537.1	166.02	1491.6	373.0	-0.99472	970
52929.15827	49.5698	50.3713	18.0	333.9	162.42	318.4	102.3	-0.98287	1846
52930.16162	49.3723	51.1589	53.3	1344.3	163.85	1291.3	377.5	-0.98912	584
52951.10343	53.1325	64.3276	119.7	3391.8	163.63	3254.4	962.9	-0.99157	232
53172.44519	30.9090	105.4060	26.9	849.2	152.99	756.7	386.4	-0.99695	1142
53173.40171	30.6927	104.8840	34.4	629.2	17.94	598.7	196.6	0.98292	1322
53181.39890	28.0318	101.4538	36.2	1586.5	149.30	1364.2	810.6	-0.99865	679
53182.39947	27.4793	101.1192	29.3	1339.1	149.87	1158.3	672.6	-0.99873	1391
53186.39977	25.5104	99.5860	69.3	2784.6	151.54	2448.4	1328.2	-0.99824	250
53187.39616	26.2104	98.5359	22.7	816.0	151.72	718.7	387.1	-0.99778	2087
53197.39430	21.9940	93.8953	15.7	126.8	155.88	115.9	53.8	-0.94784	2668
53198.36980	21.8513	93.2833	14.9	136.6	152.64	121.5	64.2	-0.96511	3203
53199.39127	22.2861	92.4201	66.5	2970.9	156.61	2727.0	1180.8	-0.99812	515
53208.31795	17.7859	87.9990	19.7	197.4	20.76	184.7	72.3	0.95684	3244
53214.33956	15.9122	84.5147	22.5	210.8	154.02	189.8	94.5	-0.96443	2792
53215.33920	15.4419	83.9798	13.6	132.7	153.90	119.3	59.6	-0.96725	3947
53221.26266	14.0158	80.9103	12.6	240.5	15.60	231.7	65.8	0.98013	5719
53222.34182	12.6377	79.9100	16.3	784.0	159.11	732.5	279.9	-0.99806	2302
53229.30103	10.0096	75.6266	16.6	407.2	154.97	369.0	172.9	-0.99436	2316
53236.23726	8.2328	70.6564	97.6	3640.5	147.94	3085.8	1934.1	-0.99822	66
53249.24027	1.7950	62.9850	14.9	192.5	153.47	172.4	87.0	-0.98165	2234
53251.19930	2.4844	60.8650	54.3	4775.1	148.21	4058.8	2516.1	-0.99968	794

Table 3.1: All quantities are in the ICRS 2000.0 reference frame. The uncertainty values presented in this data have all been scaled by a factor of 3.8 over the formal (internal) uncertainties within each given night. Column 6, $\phi_{\rm e}$, is the angle between the major axis of the uncertainty ellipse and the right ascension axis, measured from increasing differential right ascension through increasing differential declination (the position angle of the uncertainty ellipse's orientation is $90 - \phi_{\rm e}$). The last column is the number of scans taken during a given night. The quadrant was chosen such that the larger fringe contrast is designated the primary (contrast is a combination of source luminosity and interferometric visibility).

were 42 interferometric measurements with published uncertainty estimates. The uncertainty estimates were found to be systematically too small; this factor was larger in position angle than in separation. Upon iteration, it was found that the separation uncertainties for these 46 data points needed to be increase by a factor of 1.71 and the position angle uncertainties by 2.38.

3.2.3 Radial Velocity Data

Radial velocity data that has previously been published by Dworetsky et al. [1971] and Popper and Dworetsky [1978] at Lick Observatory, Hans et al. [1979] at the Dominion Astrophysical Observatory (DAO), and Duquennoy and Mayor [1988] from CORAVEL have also been collected. The Lick and DAO datasets were published without absolute uncertainty estimates but with relative weights assigned. Each data set were fit independently to a Keplerian model and the scatter in the residuals was used to determine the absolute uncertainties; The Lick Observatory unit weight uncertainty is 0.35 $\mathrm{km\,s^{-1}}$ (one measurement is marked by the authors as poor, and is given half weight); the DAO unit weight uncertainty is 0.41 $\mathrm{km\,s^{-1}}$, with the data set consisting of both unit weight and half weighted measurements. A fit of the CORAVEL data to a Keplerian model showed excess scatter beyond the level of the formal uncertainties; a scale factor of 1.527 has been applied to those uncertainties to allow these data to be combined with the other sets for simultaneous fits.

3.3 Orbital Models

The first correct orbital solution for δ Equulei was that of Luyten [1934a], and is consistent with the modern orbit. van de Kamp and Lippincott [1945] measured the astrometry of the binary photocenter (center of light) and derived its first photocentric orbit. Their measurements yielded a measure of the mass ratio of 0.508:0.492 $\pm$0.016 (van de Kamp [1954] later also derived individual masses of 1.96 and 1.89 $M_\odot$ with the same method, values which are too large due to an underestimated parallax). The first spectroscopic orbit was by Dworetsky et al. [1971], providing a mass ratio of roughly 1.044. Finally, a full three-dimensional model for the system was determined by Hans et al. [1979]. Since that time, several more orbital solutions have been offered [see, for example, Starikova, 1981, Duquennoy and Mayor, 1988, Hartkopf et al., 1996, Söderhjelm, 1999, Pourbaix, 2000].

Three model parameters for the system velocity V_o are introduced, one corresponding to each observatory from which radial velocity data is obtained. This allows for instrumental variations; in particular, Hans et al. [1979] notes a potential zero-point discrepancy of 500 $\mathrm{m\,s^{-1}}$ in data sets. Having fit each data set independently to correct uncertainty estimates, all are combined into a simultaneous fit to best determine system parameters. The results are listed in Table 3.2 and plotted in Figure 3-1.

Each fit was repeated several times varying the set of non-degenerate parameters used in order to obtain uncertainty estimates for a number of desired quantities. The fit to radial velocity data alone was fit once using $a \sin i$ and $R = M_1/M_2$ as

parameters, and again replacing these with K_1 and K_2, the velocity amplitudes. Similarly, the combined fits were repeated replacing parameters $\{a, R\}$ with the sets $\{M = M_1 + M_2, R\}$ and $\{M_1, M_2\}$. Quantities in the combined fit that were derived from other parameters are listed separately at the end of Table 3.2.

Despite spanning less than a year (a sixth of the orbit), the PHASES data by themselves are able to constrain many orbital parameters better than previous observations. We note in particular that the orbital angles are very well constrained. However, the relatively short time coverage of the PHASES data presents strong degeneracies between the system period, eccentricity, and semi-major axis, which increases the fit uncertainties to levels much larger than one would expect given the precision of the astrometry. If, for example, one holds fixed the period and eccentricity at the fit values, the uncertainty in semi-major axis drops from 3200 to 92 μas. It is noted that the PHASES-only fit results in values of period, eccentricity, and semimajor axis that agree with previous fits at only the 3σ level. As mentioned, these parameters are degenerate with each other in the PHASES-only fit, thus it is not surprising that all are discrepant at the same level. The PHASES measurements do agree well enough to be included in a combined fit. By adding just the radial velocity measurements to the fit, the degeneracies are lifted, the fit parameters agree well with previous results, and most orbital parameters are constrained at a fractional level of 10^{-4}.

The reduced χ^2_r of the combined fit to PHASES, radial velocity, and previous differential astrometry data is 1.17. This combined set represents 329 data points (each with 2 degrees of freedom); the model has 12 parameters meaning the fit has 646 degrees of freedom. This value for χ^2_r is slightly higher than one would expect, but this is likely due to the manner in which the uncertainties had to be derived. All parameter uncertainties have been increased by a factor of $\sqrt{1.17}$ to reflect this difference.

The addition of the previous differential astrometry to the combined model does little to improve the fit. The combined fit is limited by the precision of the radial velocity observations. Using the technique for obtaining high precision radial velocimetry on double line spectroscopic binaries using an iodine cell reported in Konacki [2004], a campaign to obtain such data has been started to better constrain the orbital model, component masses, and system distance. The PHASES program will also continue to observe δ Equulei so that the combination of high precision radial velocities and differential astrometry can be used for a comprehensive search for giant planets orbiting either star. Simulations show collecting ten radial velocity measurements with 20 $\mathrm{m\,s^{-1}}$ precisions during the 2005 observing season will improve the constraints on the component masses by a factor of two.

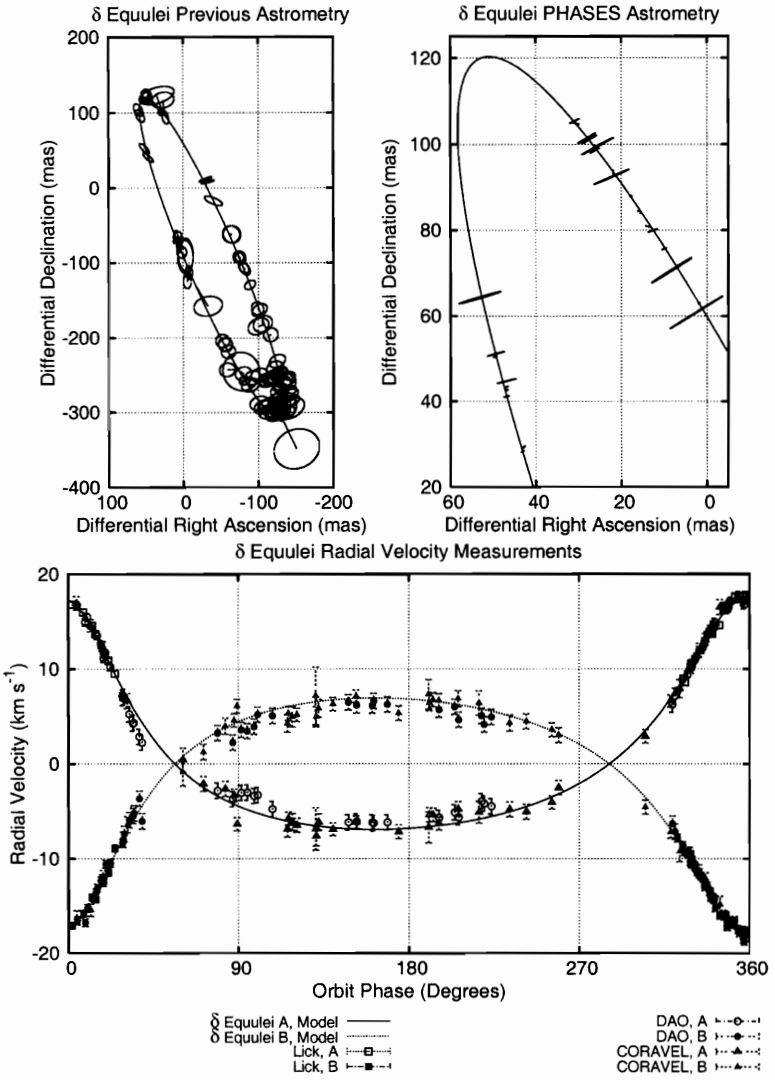

Figure 3-1: The orbit of δ Equulei. The dimensions of the uncertainty ellipses plotted for the PHASES measurements have been stretched by a factor of 3.8 as discussed in the text. The high ellipticities of PHASES uncertainty ellipses are caused by use of a single baseline interferometer coupled with the limited range of hour angles over which δ Equulei could be observed (due to limited optical delay range at PTI). For clarity, only previous astrometry measurements for which all dimensions of the uncertainty ellipses are smaller than 50 milli-arcseconds are plotted. The system center-of-mass velocities have been removed from the radial velocity graph.

Table 3.2
Orbit models for δ Equulei.

	Söderhjelm [1999]	Pourbaix [2000]	RV	PHASES	PHASES + RV	PHASES + Pre. + RV
P (yr)	5.713	5.703 ±0.0070	5.706 ±0.003	5.40 ±0.11	5.7059 ±0.0003	5.7058 ±0.0003
P (days)			2084.08 ±0.92	1974 ±39	2084.07 ±0.12	2084.05 ±0.11
T_0 (yr)	1992.85	1981.47 ±0.012	2004.285 ±0.015	2004.299 ±0.002	2004.2954 ±0.001	2004.2950 ±0.001
T_0 (MJD)			53109.9 ±5.5	53114.53 ±0.75	53112.90 ±0.45	53112.76 ±0.42
e	0.44	0.440 ±0.0046	0.4519 ±0.0029	0.415 ±0.008	0.437001 ±0.000076	0.436983 ±0.000072
a (mas)	231	232 ±1.8		222.8 ±3.2	231.85 ±0.11	231.88 ±0.11
$V_{0,Lick}$ ($\mathrm{km\,s^{-1}}$)			-15.398 ±0.097		-15.40 ±0.10	-15.40 ±0.11
$V_{0,DAO}$ ($\mathrm{km\,s^{-1}}$)			-15.876 ±0.074		-15.875 ±0.078	-15.875 ±0.081
$V_{0,C}$ ($\mathrm{km\,s^{-1}}$)		-15.85 ±0.074	-15.728 ±0.095		-15.73 ±0.10	-15.73 ±0.10
M_1 ($M_\odot$)		1.19 ±0.034			1.192 ±0.012	1.193 ±0.012
M_2 ($M_\odot$)		1.12 ±0.032			1.187 ±0.011	1.188 ±0.012
$M_1 + M_2$ ($M_\odot$)	2.35				2.380 ±0.018	2.380 ±0.019
M_1/M_2	1.06 ±0.03	1.06 ±0.018	1.004 ±0.011		1.004 ±0.012	1.004 ±0.012
i (deg)	99	99.0 ±0.43		99.520 ±0.052	99.394 ±0.020	99.396 ±0.019
ω (deg)	3	8.0 ±1.0	187.01 ±0.91	188.53 ±0.25	187.96 ±0.12	187.92 ±0.11
Ω (deg)	203	203.8 ±0.29		203.292 ±0.044	203.301 ±0.046	203.312 ±0.043
π (mas)	54.32 ±0.90	55.0 ±0.67			54.38 ±0.14	54.39 ±0.15
d (pc)					18.388 ±0.048	18.386 ±0.050
a (AU)					4.263 (Derived)	4.263 (Derived)
$a \sin i$ (AU)			4.186 ±0.011		4.206 (Derived)	4.206 (Derived)
K_1 ($\mathrm{km\,s^{-1}}$)			12.224 ±0.074		12.181 (Derived)	12.182 (Derived)
K_2 ($\mathrm{km\,s^{-1}}$)			12.272 ±0.074		12.229 (Derived)	12.230 (Derived)

Table 3.2: Pre.: Previous differential astrometry measurements.

3.4 Parallax

Early attempts to measure the parallax of δ Equulei suffered from systematic errors due to its binary nature until Luyten determined a model for the visual orbit. In the same paper that van de Kamp and Lippincott determined the first orbit of the δ Equulei photocenter, they determined a trigonometric parallax of 48 ± 5 milli-arcseconds.

The best current values for the trigonometric parallax of δ Equulei are given by Gatewood [1994] as an average of ground based observations (54.2 ± 0.93 mill-arcseconds) and from the Hipparcos mission (a binary-orbit corrected parallax of 54.32 ± 0.90 milli-arcseconds is reported [Söderhjelm, 1999]). The combined orbital solution using PHASES differential astrometry and previously published radial velocity measurements provides the best estimate of orbital parallax, at 54.39 ± 0.15 milli-arcseconds, in good agreement with the trigonometric values and the previous best orbital parallax of 55 ± 0.67 milli-arcseconds [Pourbaix, 2000]. The orbital parallax determination is limited by the precision of the radial velocity measurements; simulations show that the high precision radial velocity observations planned for the next observing season will improve the precision by a factor of two.

3.5 System Age

The measured apparent V magnitude for the system is reported as 4.487 ± 0.02 by the Simbad astronomical database. Combining this value with the measured ΔV between the stars of 0.09 ± 0.04 measured by ten Brummelaar et al. [2000] using adaptive optics on the Mt. Wilson 100" telescope and the distance determined by our orbital model, the components are found to have absolute magnitudes of $V_1 = 3.87 \pm 0.028$ and $V_2 = 3.96 \pm 0.029$. These values are combined with the stellar evolution models of Girardi et al. [2000] to determine the system age. The system's metallicities (in solar units) of [Z/H] $= -0.07$ [Gray et al., 2003] and [Fe/H] $= -0.07$ [Nordström et al., 2004] most closely match Girardi et al.'s isochrone for stars of solar metallicity. The system age is $\log t = 9.35^{+0.1}_{-0.15}$ ($\approx 2.2 \pm 0.6$ Gyr). The relevant isochrones are plotted in Figure 3-2.

3.6 δ Equulei and PHASES

δ Equulei is a sample system discussed in the S-type (orbiting just one stellar component of a binary) planet stability studies of Rabl and Dvorak [1988] and Holman and Wiegert [1999]. The numerical simulations of Rabl and Dvorak determined that planets were stable around either star if their orbital semi-major axis were 0.68 AU ($P = 0.34$ year) or smaller; an additional semi-stable region existed out to 0.86 AU. The conclusion of Holman and Wiegert was that the regions of stability were of size 0.67 AU ($P = 0.43$ years; they assumed slightly different values for the component masses) around the primary and 0.66 AU around the secondary ($P = 0.42$ years).

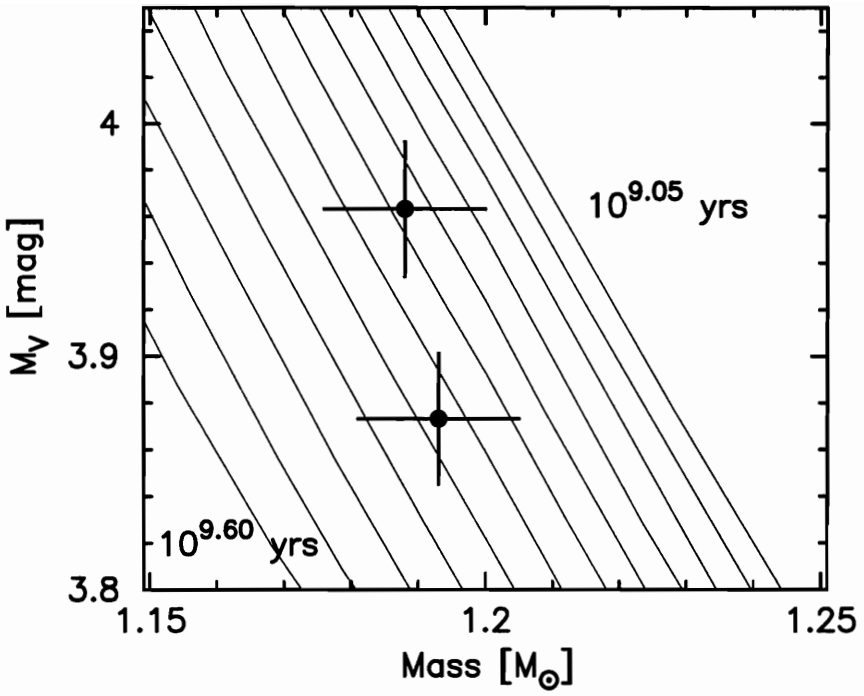

Figure 3-2: Isochrones for stars of near-solar metallicities as functions of stellar mass and absolute magnitude. Isochrones shown are separated by $\log t = 0.05$. Also plotted are the properties of the two components of δ Equulei. The system age is $\log t = 9.35^{+0.1}_{-0.15}$.

From these studies, a stable region of roughly $\frac{2}{3}$ AU around each star in which planets could be found is assumed.

No obvious periodicities are found in the fit residuals, which are plotted in Figures 3-3, 3-4, and 3-5. Periodograms of the PHASES fit residuals show no clear peaks between one and 180 days. An attempt was made to refit the PHASES data using a double-Keplerian model; each attempt was initialized with seed values for the wide Keplerian portion equal to the values found for the single Keplerian fit, with 3500 different starting values between one and 200 days for the period of the narrow portion (secondary Keplerian). The final value for the reduced χ_r^2 was never found to fall below 12.69, which is not significantly different from the value from the single Keplerian model of 14.46; because several seed periodicities produced χ_r^2 near the 12.69 level, it is concluded this slight dip is a result of random noise and the data sampling function. There are no periodic signals in our residuals at the level of 100μas, at least along the average minor axis of the PHASES uncertainty ellipses. At this conservative level one can conclude that there are not additional companions of mass

$$M_p \geq 11.5 \left(\frac{P}{\text{month}}\right)^{-\frac{2}{3}} \text{ Jupiter Masses.} \tag{3.1}$$

The orbit of a third body could be hidden if it happens to be high inclination and coaligned with the major axis of our uncertainty ellipses. A more thorough analysis of the fit residuals and better constraints on companion masses will be part of a future investigation.

3.7 Conclusions

The high precision differential astrometry measurements of the PHASES program are used to constrain the distance to δ Equulei more than four times more precisely than previous studies, despite covering only a sixth of the orbit. The orbital parallax agrees well with the trigonometric one determined by Hipparcos observations. Whereas characterization of the system was previously limited by the precisions of differential astrometry measurements, it is now limited by the radial velocity observations. Continued monitoring of this nearby standard binary will be useful to search for additional system components as small as a Jupiter mass in dynamically stable orbits.

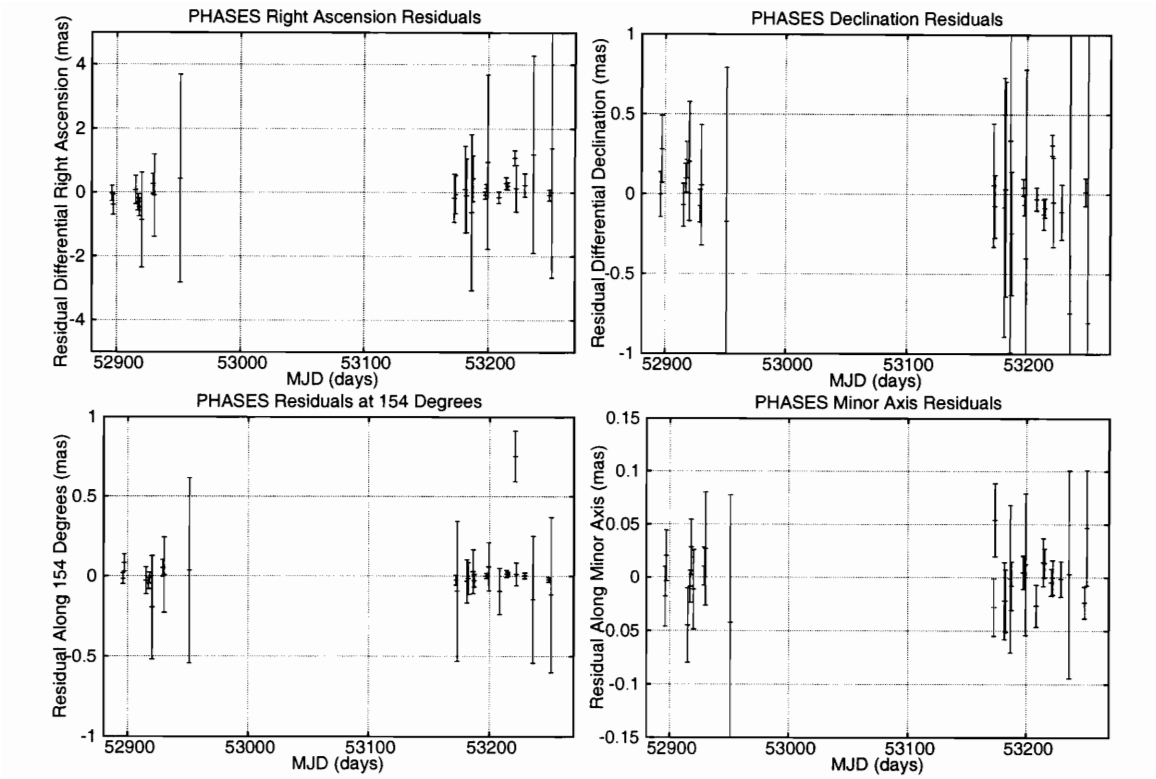

Figure 3-3: Residuals for PHASES differential astrometry of δ Equulei. The error bars plotted have been stretched by a factor of 3.8 over the formal uncertainties as discussed in the text. The high ellipticity of the uncertainty ellipses causes neither the right ascension nor the declination uncertainties to be near the precision of the minor axis uncertainties, which have median uncertainty of 26 μas. Due to the roughly North-South alignment of the baseline used for 24 of the 27 measurements, our more sensitive axis was typically declination. The bottom left plot shows the residuals along a direction that is 154 degrees from increasing differential right ascension through increasing differential declination (equivalent to position angle 296 degrees), which corresponds to the median direction of the minor axis of the PHASES uncertainty ellipses. Because the orientation of the PHASES uncertainty ellipses varies from night to night, no single axis is ideal for exhibiting the PHASES precisions, but this median axis is best aligned to do so. The bottom right plot shows residuals along the minor axis of each measurement's uncertainty ellipse.

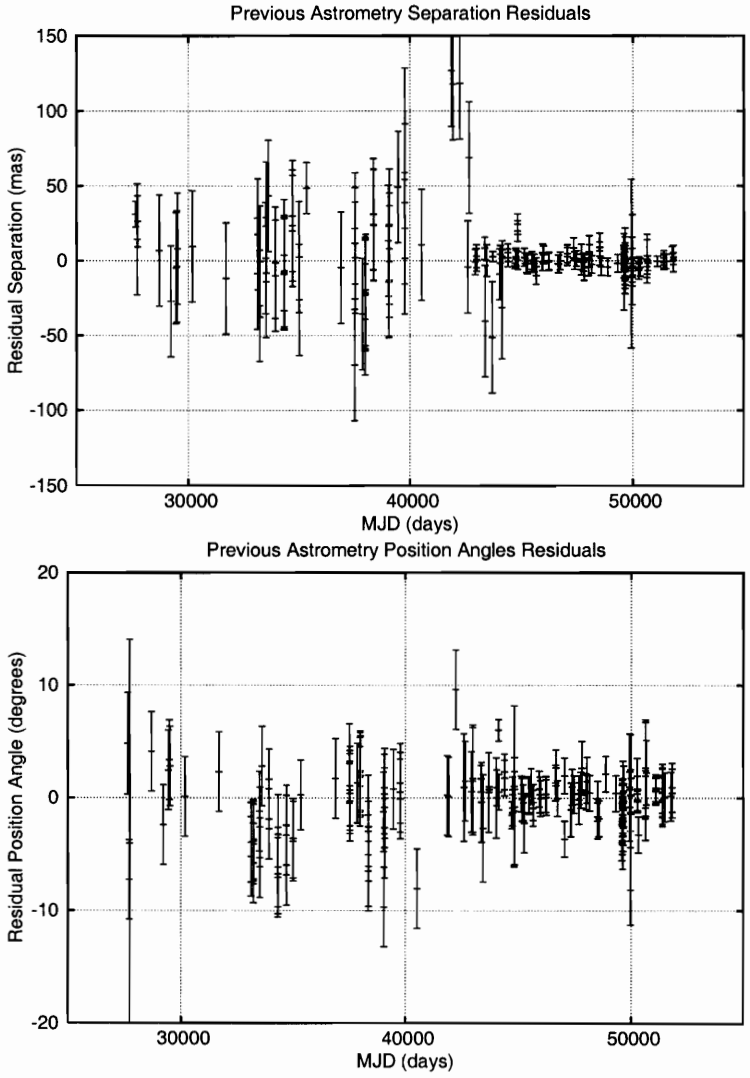

Figure 3-4: Residuals for previous differential astrometry of δ Equulei. Four points from the 1850's by Otto Wilhelm von Struve are not plotted, though they also fit well.

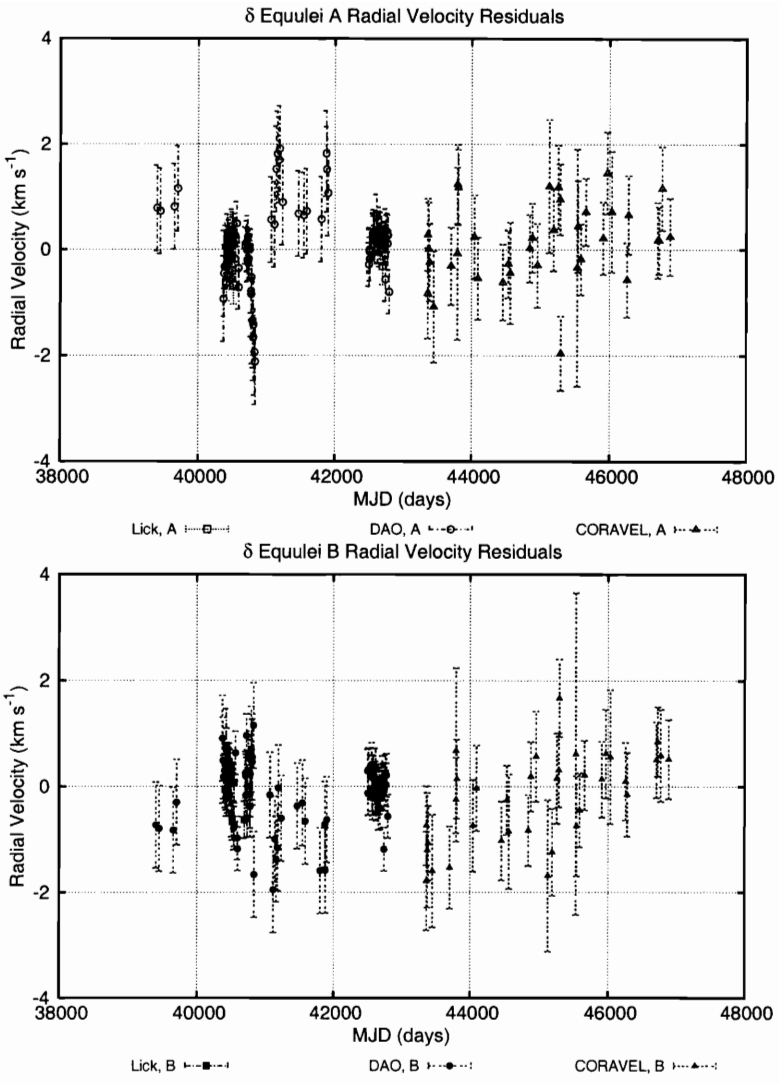

Figure 3-5: Residuals for radial velocimetry of δ Equulei, from three observatories.

Chapter 4

PHASES Differential Astrometry and Iodine Cell Radial Velocities of the κ Pegasi Triple Star System

κ Pegasi is a well-known, nearby triple star system. It consists of a "wide" pair with semi-major axis 235 milli-arcseconds, one component of which is a single-line spectroscopic binary (semi-major axis 2.5 milli-arcseconds). Using high-precision differential astrometry and radial velocity observations, the masses for all three components are determined and the relative inclinations between the wide and narrow pairs' orbits is found to be 43.8 ± 3.0 degrees, just over the threshold for the three body Kozai resonance. The system distance is determined to 34.64 ± 0.22 parsec, and is consistent with trigonometric parallax measurements.

The contents of this chapter have been submitted to the *Astrophysical Journal* for publication with authors Matthew W. Muterspaugh, Benjamin F. Lane, Maciej Konacki, Sloane Wiktorowicz, Bernard F. Burke, M. M. Colavita, S. R. Kulkarni, and M. Shao.

4.1 Introduction

κ Pegasi (10 Pegasi, ADS 15281, HR 8315, HD 206901; $V \approx 4.1$, $K \approx 3.0$) is comprised of two components, each with F5 subgiant spectrum, separated by 235 milli-arcseconds (here referred to as A and B; for historical reasons, B is the brighter and more massive—this distinction has been the cause of much confusion). Both components A and B have been reported as spectroscopic subsystems (A is in fact only a single star; B is confirmed as a double and the brighter component is designated as Ba, and the unseen companion as Bb). An additional component C is well separated from the other members of the system (13.8 arcseconds) and is faint; this may be optical (physically unrelated) and is not relevant to the present analysis.

Burnham [1880] discovered the sub-arcsecond A-B binary in 1880. Since this discovery, a number of studies have been carried out to determine the orbit of A-B and to search for additional components. Campbell and Wright [1900] reported a period

and semimajor axis for the A-B pair of 11 years and 0.4 arcseconds, respectively, and that the brighter of the stars is a spectroscopic binary with a period "that seems to be about six days." Luyten [1934b] combined all previous observational data to produce a visual orbit between components A and B and a spectroscopic orbit for Ba with period 5.97 days (he interchanged the designations A and B; here his results have been converted to the convention previously mentioned). His work also discredited previous claims that the line of apsides of Ba-Bb varied with the period of the A-B system. Luyten derived a mass for component A of 1.9 $M_{\odot}$ and a combined mass for the Ba-Bb subsystem of 3.3 $M_{\odot}$. Additionally, because there are no observed eclipses in the Ba-Bb system, he concluded that the maximum possible mass ratio M_{Ba}:M_{Bb} is 3:1. Beardsley and King [1976] obtained separate spectra for components A and B. Their observations confirmed that component B is a 5.97 day single-line spectroscopic binary, and also suggested that A was a spectroscopic binary with period 4.77 days. Barlow and Scarfe [1977] showed that additional observations did not support a subsystem in component A, and suggested that the observations of Beardsley and King suffered from mixed spectra of components A and Ba.

Mayor and Mazeh [1987] have published the most recent spectroscopic orbit for the Ba-Bb subsystem, as well as several measurements of the radial velocity of component A, which also did not confirm the proposed 4.77 day velocity variations. Mayor and Mazeh appear to switch naming conventions for components A and B several times in their paper. They report a mass ratio "M_A:M_B = 1.94 ± 0.6"; this is counter to the tradition of κ Pegasi B being the more massive star, though they later indicate that it is component B that contains the 5.97 day spectroscopic binary. The most recent visual orbit for system A-B was published by Söderhjelm using historical data combined with Hipparcos astrometry [Söderhjelm, 1999]. Because the period is relatively short and Hipparcos was capable of wide-field astrometry, estimates for the parallax (27.24 ± 0.74 mas), total mass (4.90 $M_{\odot}$), and mass ratio of components A and B (M_B:M_A = 1.76 ± 0.11, in inverse agreement with Mayor & Mazeh) were also possible. Historically, dynamical measurements of the component masses and parallax have been poorly determined for κ Pegasi due to a lack of radial velocity measurements for component A (and Bb), which leave these quantities degenerate.

This chapter reports astrometric observations of the A-B system with precisions that allow for detection of the center of light (CL) motion of the Ba-Bb subsystem. These astrometric measurements were obtained as part of PHASES, which aims to detect planets orbiting either component of fifty sub-arcsecond binaries. High-precision iodine-cell radial velocity measurements of κ Pegasi A and Ba obtained with Keck-HIRES are also presented, and a combined double Keplerian, three-dimensional orbital model for the κ Pegasi system is determined. This model allows determination of all three component masses and the distance to the system to within a few percent.

4.2 Orbital Models

Basic models have been applied to the astrometric data. The simplifying assumption was made that the Ba-Bb subsystem is unperturbed by star A over the timescale of

the observing program, allowing the model to be split into a wide (slow) interaction between star A and the center of mass (CM) of B, and the narrow (fast) interaction between stars Ba and Bb. The results presented in this paper result from modeling both the A-B and Ba-Bb motions with Keplerian orbits.

In general, one cannot simply superimpose the results of the two orbits. The observable in PHASES measurements is the separation of star A and the CL of the Ba-Bb subsystem. Because the CL of Ba-Bb, the CM of Ba-Bb, and the location of star Ba are generally all unequal, a coupling amplitude must be added to the combined model. This coupling amplitude measures the relative size of the semi-major axis of the Ba-Bb subsystem to that of the motion of the CL of the Ba-Bb subsystem. The sign of the superposition is determined by the relative sizes of the mass and luminosity ratios of the stars Ba and Bb. As an example, if the CL is located between the CM of Ba-Bb and the location of star Ba, the motion of the CL will be in opposite direction to the vector pointing from Ba to Bb. For a subsystem with mass ratio $M_{\rm Bb}/M_{\rm Ba}$ and luminosity ratio $L_{\rm Bb}/L_{\rm Ba}$, the observed quantity is

$$\overrightarrow{y_{\rm obs}} = \overrightarrow{r_{\rm A-B}} - \frac{M_{\rm Bb}/M_{\rm Ba} - L_{\rm Bb}/L_{\rm Ba}}{(1 + M_{\rm Bb}/M_{\rm Ba})\,(1 + L_{\rm Bb}/L_{\rm Ba})}\overrightarrow{r_{\rm Ba-Bb}} \tag{4.1}$$

where $\overrightarrow{r_{\rm A-B}}$ is the model separation pointing from star A to the CM of B, and $\overrightarrow{r_{Ba-Bb}}$ is the model separation pointing from star Ba to star Bb. Including this coupling term for astrometric data is important when a full analysis including radial velocity data is made. The light-time effect for the finite speed of light across the A-B orbit is included in computing the model of the Ba-Bb orbit.

Alternatively, one can directly combine a model of the A-B system with a model of the motion of the CL of Ba-Bb. For purely astrometric data such a model is appropriate. In this case, there is no sign change for the Ba-Bb CL model, and no extra coupling amplitude is required. This model is used to fit purely astrometric data sets.

$$\overrightarrow{y_{\rm obs}} = \overrightarrow{r_{\rm A-B}} + \overrightarrow{r_{\rm Ba-Bb,C.O.L.}} \tag{4.2}$$

4.3 Observations and Data Processing

4.3.1 PHASES Observations

The PHASES measurements have excess scatter about a fit to the double Keplerian model given by eq. 4.2. Either a scaling factor of 6.637 or a noise floor at 142 μas is required to produce a χ^2_r of unity for the PHASES-only orbit; these values are much larger than observed in other PHASES targets. Because the PHASES analysis has been shown to be consistent on intranight timescales, it is concluded that this excess scatter must occur on timescales longer than a day. Model fit residuals of the PHASES measurements do not show periodic signals, implying the excess scatter is not the result of an additional system component.

Two effects might explain the excess scatter in the PHASES measurements. First, significant variability of either component Ba or Bb would alter the CL position.

Hipparcos photometry shows total system photometric scatter only at the level of 4 milli-magnitudes [van Leeuwen et al., 1997]; in the extreme case that this scatter were entirely due to variability of component Bb, the astrometric signal would only be of order 35 μas. The Hipparcos range in photometric variability is 20 milli-magnitudes; variability on this scale would produce astrometric shifts of scale larger than the observed noise floor, but would require Bb to be an extremely variable star.

A second explanation for the excess scatter may be that the model (equation 4.1) is not quite the proper model for PHASES observations of triple star systems. In particular, the location of the phase-zero for the Ba-Bb subsystem is not exactly that of its CL; due to the interferometer's fringe response function, the coupling factor is non-linear and approaches the CL approximation for small separations. If the companion were faint (in this case, a white dwarf), this effect would be negligible and the phase-zero would just be the location of component Ba. If this effect is significant in the κ Pegasi system one might expect to see large amounts of night-to-night scatter in the interferometric visibility ratios between the A and B fringe packets. Unfortunately, the interferograms are much too noisy to allow detection of what is expected to be less than a 4% effect (at the level of the interferogram signal to noise, no scatter is observed in the PHASES interferograms). In comparison to recent PHASES work on the V819 Herculis triple system [Muterspaugh et al., 2005a, also this thesis, chapter 5], this effect is more significant for κ Pegasi because the baseline-projected Ba-Bb subsystem separation is sometimes of order the interferometer resolution (the V819 Herculis Ba-Bb subsystem semimajor axis is much smaller and the CL approximation is more appropriate).

For these reasons, PHASES observations are likely better suited to studying planets in binary systems than they are for studying triple star systems. The proposed processes would introduce a noise-floor to the astrometric measurements rather than a scaling to be applied to all uncertainty estimates. Orbital solutions for the triple system were twice computed; once with all PHASES uncertainties increased by a 6.637 scale factor, and again by imposing a 142 μas noise-floor on the PHASES uncertainties. Differences in the fit parameter values represent the systematic errors.

The PHASES differential astrometry measurements are listed in Table 4.1, in the ICRS 2000.0 reference frame.

Table 4.1
κ Pegasi PHASES Astrometry

JD-2	00000.5	δRA (mas)	δDec (mas)	Reweighted Uncertainties						Uncertainties with Noise Floor					
				$\sigma_{\rm min}$ (μas)	$\sigma_{\rm maj}$ (μas)	$\phi_{\rm e}$ (deg)	$\sigma_{\rm RA}$ (μas)	$\sigma_{\rm Dec}$ (μas)	$\frac{\sigma^2_{\rm RA,Dec}}{\sigma_{\rm RA}\sigma_{\rm Dec}}$	$\sigma_{\rm min}$ (μas)	$\sigma_{\rm maj}$ (μas)	$\sigma_{\rm RA}$ (μas)	$\sigma_{\rm Dec}$ (μas)	$\frac{\sigma^2_{\rm RA,Dec}}{\sigma_{\rm RA}\sigma_{\rm Dec}}$	N
5259	15558	139.4192	-68.9527	148.5	2245.9	174.63	2236.1	256.9	-0.81429	142.0	338.4	337.2	144.9	-0.17988	49
5280	42172	176.3305	-52.8124	57.5	2373.4	148.20	2017.3	1251.8	-0.99854	142.0	357.6	313.0	223.8	-0.68878	35
5283	42590	178.7642	-49.5003	55.3	253.1	158.25	235.9	106.9	-0.83218	142.0	142.0	142.0	142.0	0.00000	756
5283	47700	178.2380	-48.6352	89.0	2518.7	173.84	2504.2	284.3	-0.94917	142.0	379.5	377.6	146.9	-0.23806	36
5286	26351	179.1262	-46.6494	34.6	327.7	144.93	268.9	190.4	-0.97524	142.0	142.0	142.0	142.0	0.00000	015
5286	43495	180.0359	-45.8604	32.5	635.5	1.42	635.3	36.1	0.43473	142.0	142.0	142.0	142.0	0.00000	536
5286	25769	180.3088	-45.0103	49.6	770.9	146.66	644.6	425.7	-0.99026	142.0	142.0	142.0	142.0	0.00000	067
5286	42699	179.3844	-45.8741	23.3	591.6	2.24	591.1	32.9	0.70385	142.0	142.0	142.0	142.0	0.00000	573
5289	30945	180.2407	-42.5429	33.5	123.8	172.30	122.8	37.1	-0.41400	142.0	142.0	142.0	142.0	0.00000	935
5289	35153	180.8695	-42.7435	59.7	2076.2	0.77	2076.0	65.9	0.42147	142.0	312.8	312.8	142.0	0.02340	39
5289	33761	181.2314	-42.0489	28.4	251.0	0.66	251.0	28.5	0.10017	142.0	142.0	142.0	142.0	0.00000	171
5289	31028	181.5086	-41.4518	38.7	142.8	173.23	141.9	42.0	-0.37137	142.0	142.0	142.0	142.0	0.00000	568
5289	29061	180.7701	-41.3602	22.1	76.5	172.05	75.9	24.3	-0.39859	142.0	142.0	142.0	142.0	0.00000	320
5289	28730	180.3950	-41.7411	19.0	64.2	171.46	63.6	21.1	-0.41211	142.0	142.0	142.0	142.0	0.00000	804
5291	28300	180.4724	-39.4518	37.7	173.3	179.51	173.3	37.7	-0.03707	142.0	142.0	142.0	142.0	0.00000	315
5291	29333	179.8880	-39.7969	53.6	2184.6	1.79	2183.5	86.6	0.78553	142.0	329.1	329.0	142.3	0.05867	054
5291	11818	181.2814	-38.7883	63.9	3766.3	147.06	3161.0	2048.7	-0.99931	142.0	567.5	482.5	330.8	-0.86317	65
5291	28864	181.3653	-38.3103	24.1	606.1	2.52	605.5	35.9	0.74130	142.0	142.0	142.0	142.0	0.00000	859
5292	12057	180.8864	-38.2854	73.2	5122.7	148.32	4359.7	2690.8	-0.99949	142.0	771.8	661.1	422.9	-0.91997	36
5292	26987	181.2990	-38.0007	64.8	1315.4	4.54	1311.3	122.6	0.84768	142.0	198.2	197.9	142.4	0.05353	07
5293	25991	181.2730	-37.3111	79.1	1909.0	2.95	1906.5	126.2	0.77828	142.0	287.6	287.3	142.6	0.07860	55
5295	22128	179.7824	-34.3888	94.5	5611.8	7.01	5569.9	691.3	0.99046	142.0	845.5	839.4	174.7	0.57398	80
5295	20159	180.7612	-35.0063	93.8	3396.8	3.52	3390.4	228.7	0.91180	142.0	511.8	510.9	145.2	0.19992	62
5298	12402	179.3421	-30.6844	76.3	2358.2	5.09	2348.9	222.6	0.93893	142.0	355.3	354.1	144.9	0.18272	52
5313	50643	168.6227	-9.8442	85.7	3811.2	143.14	3049.9	2287.0	-0.99890	142.0	574.2	467.3	362.7	-0.87665	027
5314	46573	168.9574	-7.4882	200.1	14641.9	143.10	11708.9	8793.5	-0.99960	142.0	2206.1	1766.2	1329.6	-0.99106	12
5315	47072	166.1418	-4.9533	48.1	896.3	146.79	750.4	492.5	-0.99317	142.0	142.0	142.0	142.0	0.00000	389
5316	42321	164.7537	-3.8669	94.4	4229.5	145.84	3500.2	2376.3	-0.99885	142.0	637.3	533.3	376.6	-0.89277	09
5317	46749	162.4907	-2.9062	18.6	183.2	155.52	166.9	77.8	-0.96483	142.0	142.0	142.0	142.0	0.00000	600
5317	44399	162.7425	-3.3484	28.4	717.8	21.10	669.7	259.8	0.99313	142.0	142.0	142.0	142.0	0.00000	831

Table 4.1 (Continued)

JD-2	0000.5	δRA (mas)	δDec (mas)	Reweighted Uncertainties $\sigma_{\rm min}$ (μas)	$\sigma_{\rm maj}$ (μas)	$\phi_{\rm e}$ (deg)	$\sigma_{\rm RA}$ (μas)	$\sigma_{\rm Dec}$ (μas)	$\frac{\sigma^2_{\rm RA,Dec}}{\sigma_{\rm RA}\sigma_{\rm Dec}}$	Uncertainties with Noise Floor $\sigma_{\rm min}$ (μas)	$\sigma_{\rm maj}$ (μas)	$\sigma_{\rm RA}$ (μas)	$\sigma_{\rm Dec}$ (μas)	$\frac{\sigma^2_{\rm RA,Dec}}{\sigma_{\rm RA}\sigma_{\rm Dec}}$	
5318	.1157	162.9387	-0.9785	29.3	371.5	150.66	324.1	183.8	-0.98317	142.0	142.0	142.0	142.0	0.00000	22
5318	.0964	162.5248	-0.6694	36.5	484.6	150.82	423.5	238.4	-0.98456	142.0	142.0	142.0	142.0	0.00000	07
5318	.1943	161.7325	-0.6729	45.5	590.6	153.56	529.2	266.1	-0.98165	142.0	142.0	142.0	142.0	0.00000	5
5318	.0125	162.1831	-0.1186	34.9	503.3	154.19	453.4	221.4	-0.98454	142.0	142.0	142.0	142.0	0.00000	34
5319	6300	159.6357	0.5078	19.7	198.5	149.30	171.0	102.8	-0.97496	142.0	142.0	142.0	142.0	0.00000	72
5319	9162	160.0532	1.0905	15.8	140.7	156.01	128.7	59.0	-0.95637	142.0	142.0	142.0	142.0	0.00000	.39
5319	0299	160.6171	1.6181	62.2	1178.0	157.43	1088.0	455.8	-0.98902	142.0	177.5	172.7	147.8	-0.15743	46
5320	1220	159.4821	1.7555	47.0	2927.0	29.73	2541.7	1452.3	0.99931	142.0	441.0	389.4	251.1	0.76793	14
5320	1109	157.6318	2.4027	48.9	672.3	33.07	564.0	369.1	0.98745	142.0	142.0	142.0	142.0	0.00000	91
5320	6518	157.5593	2.1577	37.9	1651.8	24.63	1501.6	689.1	0.99817	142.0	248.9	233.8	165.6	0.40866	53
5321	2511	156.9988	3.2377	20.0	212.8	151.10	186.6	104.4	-0.97573	142.0	142.0	142.0	142.0	0.00000	11
5322	8836	156.3834	3.9629	21.0	307.1	35.67	249.8	179.9	0.98966	142.0	142.0	142.0	142.0	0.00000	.97
5322	9947	155.6012	5.6284	18.1	113.4	155.62	103.6	49.6	-0.91724	142.0	142.0	142.0	142.0	0.00000	50
5322	9186	156.0978	6.1869	20.9	150.8	152.91	134.6	71.1	-0.94423	142.0	142.0	142.0	142.0	0.00000	51
5323	4062	154.8590	5.5446	62.8	5338.3	145.13	4380.1	3052.3	-0.99969	142.0	804.3	664.9	474.4	-0.93213	1
5323	6794	154.9441	6.3985	20.5	138.3	152.94	123.5	65.5	-0.93639	142.0	142.0	142.0	142.0	0.00000	93
5323	7795	155.2394	7.0247	20.3	156.2	154.23	140.9	70.3	-0.94743	142.0	142.0	142.0	142.0	0.00000	79
5323	4000	154.6541	7.2600	40.8	282.9	150.03	245.9	145.7	-0.94659	142.0	142.0	142.0	142.0	0.00000	.84
5324	2289	151.8710	8.8380	19.2	282.1	148.88	241.7	146.8	-0.98828	142.0	142.0	142.0	142.0	0.00000	47
5327	2848	148.9036	11.8975	49.2	1684.3	160.31	1585.9	569.5	-0.99578	142.0	253.8	243.7	158.7	-0.36294	74
5328	3449	145.3500	13.9405	33.5	532.2	37.54	422.5	325.4	0.99157	142.0	142.0	142.0	142.0	0.00000	56
5331	.0718	142.2377	18.5964	27.6	652.0	159.78	611.9	226.8	-0.99157	142.0	142.0	142.0	142.0	0.00000	46

Table 4.1: PHASES data for κ Pegasi. All quantities are in the ICRS 2000.0 reference frame. The reweighted uncertainty values presented in this data have all been scaled by a factor of 6.637 over the formal (internal) uncertainties within each given night. Alternatively, a noise floor is introduced to the uncertainties at a value of 142 μas; both methods of accounting for excess scatter in the data are used in modeling the system to determine systematic uncertainties. Column 6, $\phi_{\rm e}$, is the angle between the major axis of the uncertainty ellipse and the right ascension axis, measured from increasing differential right ascension through increasing differential declination (the position angle of the uncertainty ellipse's orientation is $90 - \phi_{\rm e}$). Introducing a noise floor to the data preserves this orientation angle. The last column is the number of scans taken during a given night.

4.3.2 Previous Differential Astrometry Measurements

Previously published differential astrometry measurements made with other methods have been collected. Most of these measurements were tabulated by Hartkopf et al. [2004] in the Fourth Catalog of Interferometric Measurements of Binary Stars, though several additional measurements (particularly those made by micrometer measures) had to be researched from the original sources. In two cases discrepancies were found between the uncertainties listed in the Fourth Catalog and the original sources (the 1982.595 and 1982.852 measurements, both from Tokovinin [1983]); in each case the uncertainties listed in the original work were used. Several data points listed without uncertainty estimates in the Fourth Catalog were found to have uncertainty estimates listed in the original works, in which case those values were used.

A Keplerian model was fit to the data points for which uncertainty estimates were available to determine whether these were systematically too large or too small, and to find outliers. Because there were only eight visual/micrometer measurements with published uncertainties, these were not treated as a separate group. There were 38 interferometric measurements with published uncertainty estimates. The uncertainty estimates were found to be systematically too small; this factor was larger in position angle than in separation. Upon iteration, it was found that the separation uncertainties for these 46 data points needed to be increase by a factor of 1.1 and the position angle uncertainties by 2.22. A double Keplerian model (as in eq. 4.2, to allow for the Ba-Bb subsystem) does not improve the fit; the measurements are insensitive to this small signal.

Most of the previous differential astrometry measurements were published without any associated uncertainties. To allow these to be used in combined fits with other data sets, the average uncertainties were determined as follows. The measurements were separated into subgroups by observational method and each set was analyzed individually; the first group included eyepiece and micrometer observations, and the second contained interferometric observations, including speckle, phase-grating, aperture masking, and adaptive optics. The uncertainties were first estimated to be 10 milli-arcseconds in separation and 1 degree in position angle. A Keplerian model was fit to the data, and residuals in separation and position angle treated individually to update the estimates and outliers removed. This procedure was iterated until uncertainties were found consistent with the scatter. Again no improvements were seen in fitting to a double Keplerian model. The 88 visual data points used have average uncertainties of 28.1 milli-arcseconds in separation and 7.76 degrees in position angle. The 36 interferometric data points used have average uncertainties of 2.8 milli-arcseconds and 1.1 degrees.

While these previous differential astrometry measurements were generally made at different observing wavelengths than the PHASES K-band measurements, their precision is low enough that the wavelength dependency of the Ba-Bb CL is negligible.

4.3.3 Iodine-cell Radial Velocity Data

Twenty radial velocity measurements for component A and thirty for component Ba were obtained with an iodine gas cell reference using the HIRES spectrometer on the Keck telescopes, using the method described in Konacki [2004]. The formal uncertainties of these velocity measurements agree relatively well with scatters about simple models. The component A velocity uncertainties need to be increased by a multiplicative factor of 1.073 to fit a simple linear model ($a + bx$, x is time) with goodness of fit $\chi^2_r = 1$. The component Ba velocities were fit to a single-Keplerian model representing the Ba-Bb orbital motion combined with a quadratic equation for the CM velocity, which accounts for A-B motion. The component Ba velocity uncertainties must be increased by a multiplicative factor of 1.184 to fit with $\chi^2_r = 1$. These measurements are listed in Table 4.2; the uncertainties presented have already been increased by these amounts. The average velocity uncertainty for the (spectrally broad lined) component A is 250 $\mathrm{m\,s^{-1}}$ and that for component Ba is 35 $\mathrm{m\,s^{-1}}$.

The angle of the Keck-HIRES slit mask is held constant relative to angle on the sky for all observations, and the slit is centered on the CL of the three κ Pegasi components A, Ba, and Bb. Orbital motion of the A-B system changes the position of each star relative to the CL of the system and thus within the slit. These alignment changes are observed as an apparently variable system CM velocity; the signs of these variations for component A are opposite that for the Ba-Bb pair. In the combined 3-dimensional fit with other data sets, this effect is modeled with a polynomial system velocity of

$$V_A = V_{0,Keck} + V_{1,Keck}\,(t - 53198) + V_{2,Keck}\,(t - 53198)^2 \tag{4.3}$$

for component A and

$$V_{Ba} = V_{0,Keck} - R_V\left(V_{1,Keck}\,(t - 53198) + V_{2,Keck}\,(t - 53198)^2\right) \tag{4.4}$$

for component Ba, where t is the time of observation (accounting for the light-time effect) in Modified Julian Date (MJD), and 53198 is an arbitrary offset near the average time of all observations. The best fit is found with fixing $R_V = 1$ without letting it vary as a fit parameter, likely because only the (higher precision) Ba measurements are sensitive to this effect (the size of the required correction is found to be smaller than the component A measurement precisions). Illuminating the slit with a multimode fiber may remove this effect.

The observed spectra do show effects from a third set of spectral lines. These are probably from component Bb; that they can be seen at all indicates this component is too bright to be a white dwarf. A three-dimensional cross-correlation is being developed to obtain velocity measurements for all three components simultaneously, which will be included in a future investigation.

Table 4.2
Keck-HIRES Radial Velocities

JD-2400000.5	RV A ($km\,s^{-1}$)	σ_A ($km\,s^{-1}$)	RV Ba ($km\,s^{-1}$)	$\sigma_B a$ ($km\,s^{-1}$)
52961.26742			30.6932	0.0358
52961.30804			29.4782	0.0368
52961.38225			27.0732	0.0377
52962.25385			-8.9328	0.0346
52962.29817			-10.8228	0.0347
52962.37163			-14.0178	0.0378
52962.37825			-14.3178	0.0384
53094.64549			-42.7248	0.0374
53094.64687			-42.7958	0.0369
53094.65230			-42.8538	0.0378
53205.36826	-20.1918	0.2499	39.5022	0.0318
53205.37367	-20.1978	0.2138	39.4852	0.0352
53205.40455	-20.1938	0.2551	39.5292	0.0314
53205.40589	-20.0458	0.2501	39.4652	0.0318
53205.45277	-20.2498	0.2337	39.5232	0.0334
53205.45679	-20.0298	0.2137	39.4502	0.0363
53205.49655	-19.8808	0.2037	39.2702	0.0377
53205.49792	-19.8688	0.2046	39.3172	0.0365
53205.55404	-20.0027	0.3180		
53205.55811	-20.0847	0.3032		
53276.30124	-19.6247	0.2562	25.5523	0.0350
53276.30196	-19.8067	0.2554	25.5453	0.0350
53276.39785	-19.3757	0.2648	28.5373	0.0340
53276.40044	-19.5267	0.3083	28.6253	0.0328
53276.47261	-19.1697	0.2747	30.6663	0.0333
53276.47322	-19.1787	0.2669	30.6823	0.0332
53277.25969	-18.8347	0.2734	38.0633	0.0445
53277.26627	-18.9937	0.2201	37.9723	0.0349
53277.29652	-19.0287	0.2141	37.6463	0.0328
53277.29817	-18.9047	0.2155	37.6093	0.0329
53328.28414			-42.1537	0.0329
53328.33982			-40.8997	0.0336

Table 4.2: Keck-HIRES iodine-cell radial velocity data of κ Pegasi. The uncertainties presented have been scaled from the formal (internal) uncertainties to reflect the scatter about a best-fit models. The scaling factor for component A velocities was 1.073; for Ba, it was 1.184.

4.3.4 Previous Radial Velocity Data

Previously published radial velocity measurements from Lick Observatory and CORAVEL have also been collected. Each set of radial velocity measurements were fit to double Keplerian models. Luyten [1934b] determined the uncertainties of the Lick Observatory velocities presented in Henroteau [1918] at 1.66 $\mathrm{km\,s^{-1}}$; these values are found to be consistent in the present study. The CORAVEL velocities from Mayor and Mazeh [1987] required reweighting by a multiplicative factor of 2.31 to be consistent with the scatter about the model.

Three velocities for component A were reported in Mayor and Mazeh [1987]. These measurements are discrepant with the other measurements, and are not included in the present fit. Because these velocity measurements were made with a one dimensional cross-correlation algorithm, spectral contamination from component Ba may have biased the A velocities. The broad spectral lines of component A may be more sensitive to spectral blending.

4.4 Orbital Solution

A combined model for the system was determined by fitting all measurements to equation 4.1. The fit was repeated twice, once using PHASES data with reweighted uncertainties, and again with a 142 μas noise floor for the PHASES data. All plots presented in this paper assume the fit solution in which the 142 μas noise floor was imposed. The combined fit with PHASES data uncertainties reweighted has a minimized reduced $\chi^2_r = 1.223$; for the combined fit with a 142 μas PHASES noise floor $\chi^2_r = 1.228$. The fits have 22 free parameters and 555 degrees of freedom; the values for χ^2_r are slightly higher than one would expect, likely resulting from the way in which several of the uncertainties had to be estimated. The uncertainties presented for all fit parameters in Table 4.3 have been increased by a factor of $\sqrt{\chi^2_r}$. The combined orbital model is plotted in Figures 4-1 (the A-B orbit) and 4-2 (the Ba-Bb orbit).

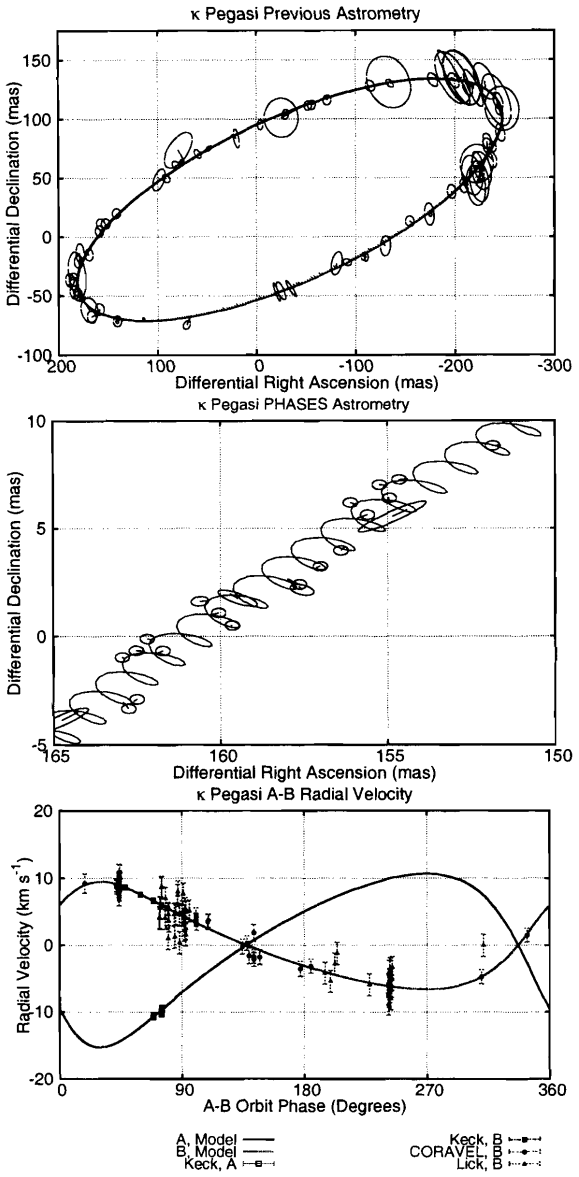

Figure 4-1: The orbit of κ Pegasi A-B. (Top) The complete A-B orbit plotted with the uncertainty ellipses for previous differential astrometry measurements. For clarity, only previous astrometry measurements for which all dimensions of the uncertainty ellipses are smaller than 20 milli-arcseconds are plotted. (Middle) A portion of the PHASES measurements from the 2004 observing season; the CL motion of the Ba-Bb orbit is superimposed on the A-B (wide) orbit. A noise floor of 142 μas has been imposed on the PHASES measurements as discussed in the text. (Bottom) Component A and Ba radial velocity measurements; the system CM velocities and Ba-Bb motion have been removed from the radial velocity graph. Phase zero is at periastron passage.

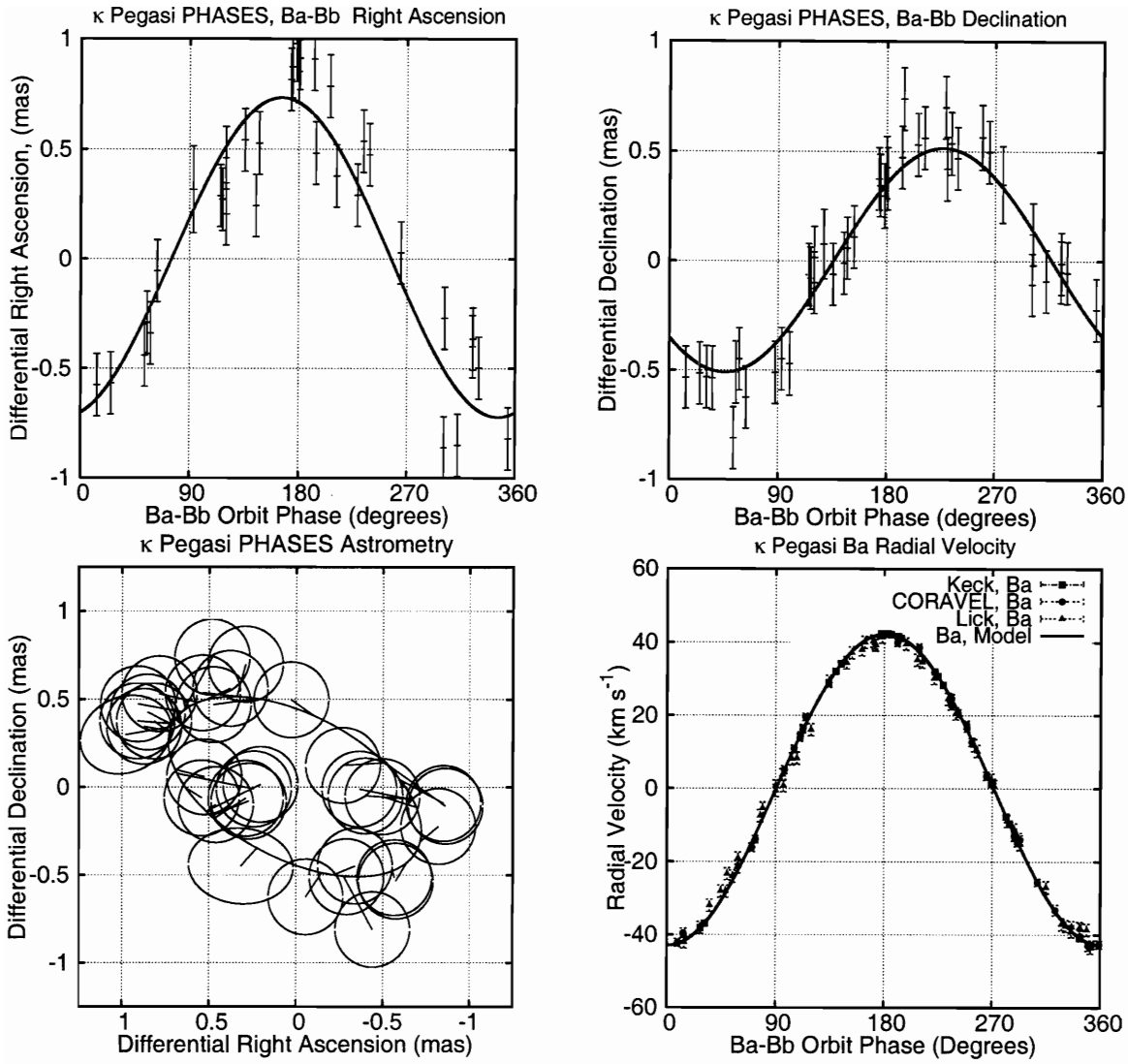

Figure 4-2: The orbit of κ Pegasi Ba-Bb. (Top Left and Right, Bottom Left) Apparent astrometric orbit of the Ba-Bb CL, plotted with PHASES measurements (with the A-B motion removed). A noise floor of 142 μas has been imposed on the PHASES measurements as discussed in the text. Only measurements with uncertainties less than 200 μas are plotted. (Top) Differential right ascension (Left) and declination (right) versus orbital phase; phase zero is at periastron passage. (Bottom Left) Only those measurements for which all dimensions of the uncertainty ellipses are smaller than 200 μas are plotted. (Bottom Right) Radial velocity of component Bb; system CM velocities and A-B orbit velocities have been removed.

Table 4.3
Orbit models for κ Pegasi

	Martin et al. [1998] Hartkopf et al. [1989]	Söderhjelm [1999]	PHASES Reweight + Pre. + RV	PHASES 142 μas floor + Pre. + RV	Combined Average and Uncertainties
P_{A-B} (days)	4237 ±44*	4233*	4224.98 ±0.80	4224.80 ±0.81	4224.89 ±0.81
$T_{0,A-B}$ (MJD)	43950 ±9.9 (52424)†	48188 (52422)†	52400.0 ±1.6	52397.7 ±2.0	52398.8 ±2.0
e_{A-B}	0.313 ±0.009	0.31	0.3147 ±0.0014	0.3152 ±0.0016	0.3150 ±0.0016
i_{A-B} (degrees)	108.04 ±0.50	108	107.899 ±0.026	107.921 ±0.030	107.910 ±0.030
ω_{A-B} (degrees)	304.17 ±0.60	305	304.46 ±0.16	304.28 ±0.21	304.37 ±0.21
Ω_{A-B} (degrees)	288.85 ±0.60	290	109.044 ±0.043	109.114 ±0.057	109.079 ±0.057
P_{Ba-Bb} (days)			5.9714971 $\pm 1.3 \times 10^{-6}$	5.9714971 $\pm 1.3 \times 10^{-6}$	5.9714971 $\pm 1.3 \times 10^{-6}$
$T_{0,Ba-Bb}$ (MJD)			52402.23 ±0.10	52402.23 ±0.10	52402.23 ±0.10
e_{Ba-Bb}			0.0072 ±0.0013	0.0072 ±0.0013	0.0072 ±0.0013
i_{Ba-Bb} (degrees)			128.6 ±1.5	121.4 ±3.3	125.0 ±3.6
ω_{Ba-Bb} (degrees)			359.2 ±6.0	359.1 ±6.0	359.2 ±6.0
Ω_{Ba-Bb} (degrees)			63.96 ±0.93	63.0 ±2.2	63.5 ±2.2
$V_{0,Keck}$ (km s^{-1})			-9.46 ±0.22	-9.46 ±0.22	-9.46 ±0.22
$V_{1,Keck}$ (km s^{-1} day^{-1})			$-2.2 \times 10^{-4} \pm 3.4 \times 10^{-4}$	$-2.2 \times 10^{-4} \pm 3.4 \times 10^{-4}$	$-2.2 \times 10^{-4} \pm 3.4 \times 10^{-4}$
$V_{2,Keck}$ (km s^{-1} day^{-2})			$6.7 \times 10^{-6} \pm 2.4 \times 10^{-6}$	$6.8 \times 10^{-6} \pm 2.4 \times 10^{-6}$	$6.7 \times 10^{-6} \pm 2.4 \times 10^{-6}$
$V_{0,C}$ (km s^{-1})			-9.40 ±0.26	-9.40 ±0.26	-9.40 ±0.26
$V_{0,Lick}$ (km s^{-1})			-8.36 ±0.26	-8.36 ±0.26	-8.36 ±0.26
M_A ($M_\odot$)	1.562 ±0.197	1.78 ±0.16	1.535 ±0.050	1.543 ±0.051	1.539 ±0.051
M_{Ba+Bb} ($M_\odot$)	2.602 ±0.284	3.13 ±0.27	2.474 ±0.078	2.486 ±0.079	2.480 ±0.079
M_{Bb}/M_{Ba}			0.522 ±0.019	0.457 ±0.024	0.490 ±0.033
L_{Bb}/L_{Ba}			0.0077 ±0.013	0.000 ±0.021	0.0038 ±0.021
d (parsecs)			34.59 ±0.21	34.68 ±0.22	34.64 ±0.22
$K_{p,A} - K_{p,B}$ (Magnitudes)					0.190 ±0.001
M_{Ba} ($M_\odot$)					1.665 ±0.064
M_{Bb} ($M_\odot$)					0.816 ±0.045
a_{A-B} (AU)					8.132 ±0.063
a_{Ba-Bb} (AU)					0.08720 ±0.00092
π (mas)	28.63 ±0.92	27.24 ±0.74			28.87 ±0.18

Table 4.3: Orbit models for κ Pegasi. Pre.: Previous differential astrometry measurements. Uncertainties in the final column are the maximum of three uncertainties: the uncertainty from the combined fit that included PHASES-reweighted data, that including PHASES data with a 142 μas noise floor, and the difference in the fit values for the two models. The luminosity ratio L_{Bb}/L_{Ba} is for K-band observations. $K_{p,A} - K_{p,B}$ is derived from Keck adaptive optics imaging rather than from PHASES measurements. The final five parameters are derived from the other quantities; their uncertainties are determined via error propagation.

* Converted from years in original work.

† Converted from years in original work, quantity in parenthesis converts to common epoch.

No evidence supporting additional companions is seen, including the proposed 4.77-day period companion to κ Pegasi A. The suggested amplitude for the velocity curve in Beardsley & King was roughly 30 $\mathrm{km\,s^{-1}}$, corresponding to astrometric motion of star A on order 1.1 mas, an effect that would be seen in the PHASES astrometric data if present. The data residuals are plotted in Figures 4-3 and 4-4.

4.4.1 Eccentricity and Mutual Inclination

A small—but non-zero—eccentricity is found in the Ba-Bb system. The main sequence age for 1.6 $M_\odot$ stars is of order 2.5 gigayears (Gyr); the subgiant luminosity classes of components A and Ba implies the system age is likely near this value. Tidal circularization of the Ba-Bb system is predicted to occur on Gyr timescales [Zahn, 1977]; tidal circularization explains the low eccentricity only if three-body dynamics do not dominate the evolution of the Ba-Bb eccentricity.

The mutual inclination Φ of two orbits is given by

$$\cos\Phi = \cos i_1 \cos i_2 + \sin i_1 \sin i_2 \cos\left(\Omega_1 - \Omega_2\right) \tag{4.5}$$

where i_1 and i_2 are the orbital inclinations and Ω_1 and Ω_2 are the longitudes of the ascending nodes. The combined fit gives a value of 43.8 ± 3.0 degrees for the relative inclinations of the A-B and Ba-Bb orbits. This represents only the sixth system for which unambiguous determination of the mutual inclination is possible.

The mutual inclination of the κ Pegasi system is found to be just over the threshold (39.2 degrees) required for the Kozai Mechanism to drive inclination-eccentricity oscillations in the Ba-Bb system [Kozai, 1962]. The maximum eccentricity found in such oscillations is given by Innanen et al. [1997] as

$$e_{\max} = \sqrt{1 - (5/3)\cos^2\left(\Phi_0\right)} \tag{4.6}$$

where Φ_0 is the mutual inclination at small eccentricity states. For a mutual inclination of 43.8 ± 3.0 degrees, $e_{\max}$ is in the range $0.36^{+0.15}_{-0.10}$. While the fit solution shows a slight (1.5σ) preference for a mutual inclination for which Kozai oscillations will occur, the uncertainty is such that a lack of such oscillations would not be a complete surprise. The period of Kozai oscillations would be of order 10^4 years [Kiseleva et al., 1998]; this is much shorter than predicted tidal circularization timescales. An insignificant amount of orbital energy would be lost to tidal heating over the course of each oscillation, and the Kozai Mechanism would dominate the evolution of the eccentricity of the Ba-Bb subsystem. Over the life of the system, it is possible that some orbital energy is lost to tidal heating.

The current small value for the Ba-Bb eccentricity tempts one to conclude that Kozai oscillations do not occur (i.e. that the true mutual inclination is on the lower side of the 39.2 degrees threshold), but it is also possible that it is simply being observed at a fortunate time. Over the ninety years over which radial velocity measurements of Ba have been made, one might expect to see variations in the Ba-Bb eccentricity of order a fraction of a percent. The Lick and CORAVEL radial velocity

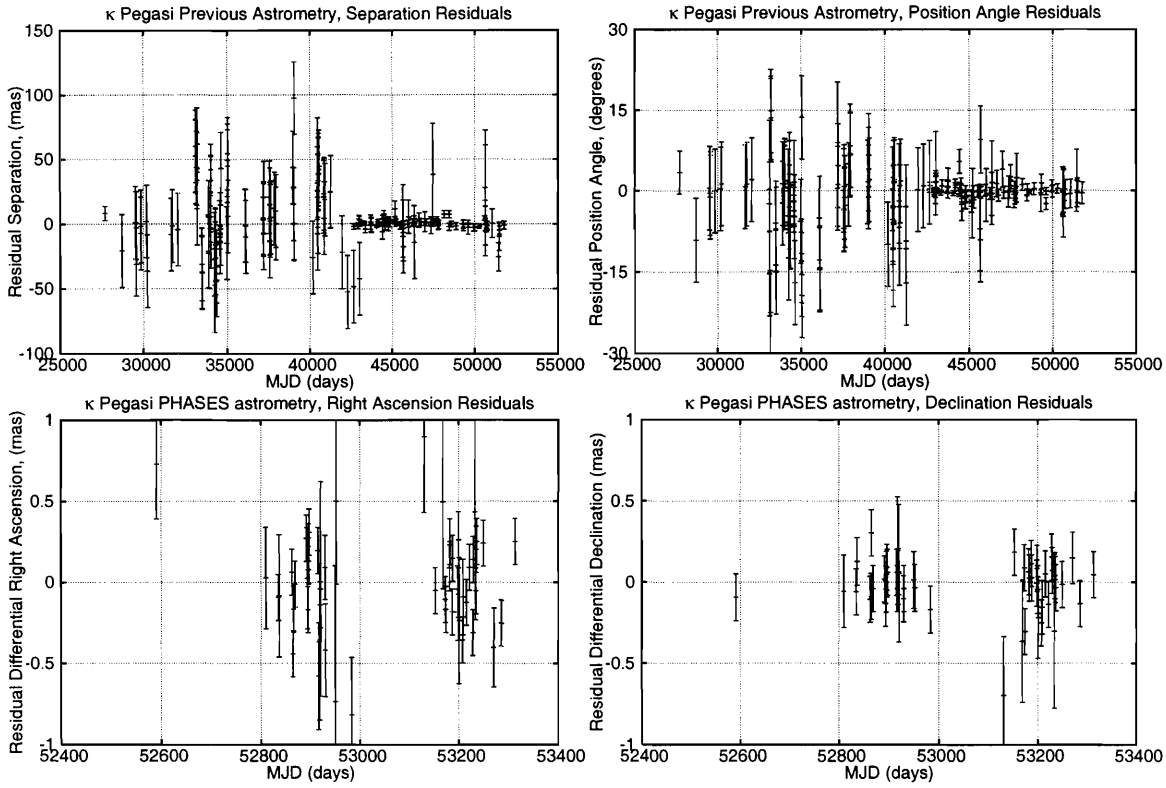

Figure 4-3: Residuals for differential astrometry of κ Pegasi. (Top) Separation (left) and position angle (right) residuals to the combined model for previous astrometric measurements. (Bottom) Right ascension (left) and declination (right) residuals to the combined model for PHASES measurements. A noise floor of 142 μas has been imposed on the PHASES measurements as discussed in the text.

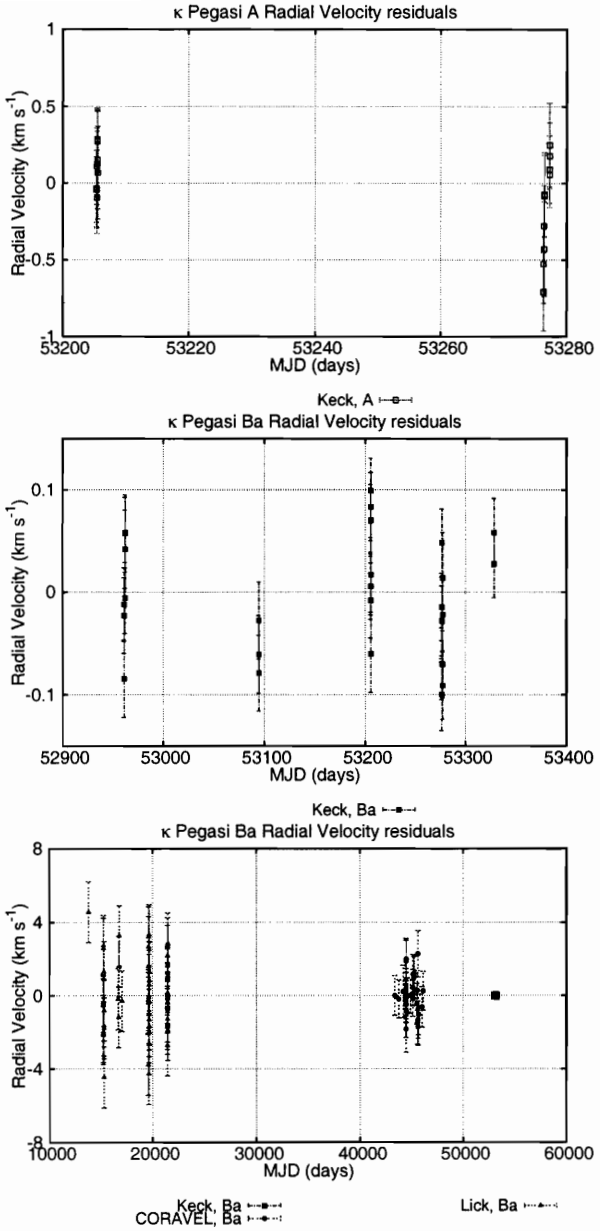

Figure 4-4: Residuals for radial velocimetry of κ Pegasi. (Top) Component A velocity residuals to the combined model. (Middle) Keck-HIRES component Ba velocity residuals to the combined model. (Bottom) All component Ba velocity residuals to the combined model.

measurements by themselves each only determine the Ba-Bb eccentricity to the level of a percent, thus one cannot measure whether significant Kozai-induced eccentricity variations have occurred.

4.4.2 Parallax

The combined astrometric and RV model is used to determine the distance to the system, and in turn a value of 28.87 ± 0.18 milli-arcseconds for the system parallax. This value agrees well with the trigonometric parallax determined from Hipparcos astrometry by Martin et al. [1998], who reprocessed the Hipparcos astrometry using the A-B orbital model of Hartkopf et al. [1989] for CL astrometric corrections; their value is 28.63 ± 0.92. The raw Hipparcos trigonometric parallax of 28.34 ± 0.88 milli-arcseconds also agrees well [Perryman et al., 1997].

The revised Hipparcos analysis of Söderhjelm [1999] gives a value of 27.24 ± 0.74, which does not agree well with the other results. Also discrepant is the original (ground-based) trigonometric parallax measurement of 35.6 ± 3.2 of van de Kamp [1947]. It should be noted that for much of the history of the system's study, the parallax of van de Kamp was used to estimate the total system mass, leading to discrepant values. Both of these do agree at the 3σ level, and it is concluded that the present value of 28.87 ± 0.18 is most consistent with all observations.

4.4.3 Component Masses and Stellar Evolution

Components A and Ba are of roughly equal mass (at $M_A = 1.539 \pm 0.051 M_\odot$ and $M_{Ba} = 1.665 \pm 0.064$), and were likely late-type A or early F dwarfs stars before evolving to their present state slightly off the main sequence. The measured mass for component Bb ($M_{Bb} = 0.816 \pm 0.045 M_\odot$) indicates it is likely a late-type G or early K dwarf. The third set of lines are observed in the Keck-HIRES spectra supports identification of this component as a late G/early K dwarf rather than a white dwarf remnant of a much more massive star. At near-infrared K-band, the expected luminosity of a late G/early K dwarf is 7% that of either component A or Ba; while not in perfect agreement with the combined fit value for the luminosity ratio, this does indicate the low value is appropriate and astrometric effects due to a luminous third component are small.

The κ Pegasi system is valuable to modeling stellar evolution as masses for all three components are well-constrained, and two slightly evolved stars can be assumed coevolved with the faint dwarf component Bb. Differential magnitudes for all system components (which can perhaps be determined from the Keck-HIRES spectra in a later investigation) are required for proper evolutionary modeling.

Keck adaptive optics observations of κ Pegasi on MJD 53227.44 determine a differential magnitude between component A and combined light for Ba and Bb of 0.188 ± 0.001 magnitudes in a narrow band H_2 2-1 filter centered at 2.2622 microns. Observations of similar spectral type 20 Persei (F4V+F6V) during the same evening in both the narrow band filter and astronomical K_p band are used to approximate the

K_p band differential magnitude as 0.190 ± 0.001. Better measurement of the relative intensities of Ba and Bb is required to constrain stellar models.

4.5 Conclusions

The PHASES measurements provide detection of the κ Pegasi Ba-Bb subsystem CL motion for the first time. This allows the mutual inclinations of the wide and narrow orbits to be determined; this is only the sixth such determination that has been made. The high value for the relative inclination implies the narrow (Ba-Bb) pair may undergo eccentricity-inclination oscillations caused by the Kozai mechanism. No evidence for additional system components is observed.

Combined with radial velocity observations, the distance to the κ Pegasi system is determined to a fifth of a parsec. The distance agrees well with that determined by Hipparcos astrometry, and is of higher precision. Masses for each component are determined at the level of a few percent; continued observations—particularly to determine additional velocities for component A (or the first velocities for Bb)—will improves these mass measurements. Future investigations of this system to determine the relative luminosities of the three components will allow model fitting of the components' evolutions, of particular interest because two components have evolved slightly off the main sequence.

Chapter 5

PHASES Differential Astrometry and the Mutual Inclination of the V819 Herculis Triple Star System

V819 Herculis is a well-studied triple star system consisting of a "wide" pair with 5.5 year period, one component of which is a 2.2-day period eclipsing single-line spectroscopic binary. Differential astrometry measurements from the Palomar High-precision Astrometric Search for Exoplanet Systems (PHASES) are presented and used to determine the relative inclinations of the short- and long-period orbits.

The contents of this chapter have been submitted to *Astronomy & Astrophysics* for publication with authors Matthew W. Muterspaugh, Benjamin F. Lane, Maciej Konacki, Bernard F. Burke, M. M. Colavita, S. R. Kulkarni, and M. Shao.

5.1 Introduction

Determinations of the mutual inclinations of the two orbits in hierarchical triple stellar systems are rare, with previously only four unambiguous determinations available in the literature [Lestrade et al., 1993, Heintz, 1996, Hummel et al., 2003], but valuable; the dynamical relaxation process undergone by multiples after formation is expected to leave a statistical "fingerprint" in the distribution of inclinations [Sterzik and Tokovinin, 2002]. In addition, well-characterized stellar multiples represent excellent opportunities to test and challenge stellar models under stringent constraints of common age and metallicity.

V819 Herculis (HR 6469, HD 157482; $V = 5.6$, $K = 4.1$) is a triple system consisting of an evolved star (G7 III-IV; this appears brighter in V and will be referred to as the A component) in an eccentric 5.5 year orbit together with a close ($P_n \approx 2.2$ days) pair of main sequence F stars. The close pair (Ba and Bb) is in an edge-on orbit and exhibits shallow eclipses. A combination of radial velocity, speckle interferometry, eclipse timing and light-curve fitting has made it possible to accurately determine most of the interesting system parameters, including masses, radii and distance [Scarfe et al., 1994, van Hamme et al., 1994, Wasson et al., 1994] with ac-

curacies of a few percent. However, until now it has not been possible to determine the mutual inclination of the orbits. The V819 Her system is listed as a chromospherically active binary in the catalog by Strassmeier et al. [1993]; it exhibits Ca H and K emission and has been detected in X-rays [Dempsey et al., 1993] but not in radio [Drake et al., 1989]. The system is variable with an amplitude of approximately 80 milli-magnitudes. In addition to the eclipses of the close pair, the GIV exhibits quasi-periodic variability attributed to starspots [van Hamme et al., 1994].

5.2 Observations and Data Processing

5.2.1 PHASES Observations

V819 Herculis was observed using PTI on 31 nights in 2003-2005 using the observing mode described in Lane and Muterspaugh [2004]. For V819 Herculis, the typical scanning rate in 2003 was one scan per second and four intensity measurements per ten milliseconds; these values were doubled in 2004. The typical scan amplitude was 100 microns. An average of 3099 scans were collected each night the star was observed over a time span of 18 to 179 minutes.

The differential astrometry measurements are listed in Table 5.1, in the ICRS 2000.0 reference frame. In order to evaluate the night-to-night astrometric stability of the data, the PHASES data were fit to a model consisting of a Keplerian orbit representing the Ba-Bb center of light (CL) motion and a low-order polynomial representing motion of the A-B orbit. The minimized value of reduced $\chi^2_r = 4$, implying either that the internal (i.e. derived from a single night of data) uncertainty estimates are too low by a factor of 2, or that the simple model is not appropriate for this system. Replacing the polynomial model for A-B with a Keplerian does not improve the value of χ^2_r (to be expected given the limited fraction of the A-B orbit covered by the PHASES data set). It is possible starspots caused astrometric jitter on this scale. The PHASES uncertainties presented in this chapter have been increased by a factor of 2 to account for this discrepancy. The rescaled (raw) median minor- and major-axis uncertainties are 15.2 (7.6) and 363 (181) μas. The rescaled (raw) mean minor- and major-axis uncertainties are 19.6 (9.8) and 568 (284) μas respectively.

5.2.2 Potential Systematic Errors

The fractional precision of the PHASES astrometric measurements is $\sim 10^{-4}$; at such an ambitious level there are many possible sources of systematic error that could appear on inter-night timescales. In particular, the system in question exhibits two potential astrophysical sources of measurement noise: starspots and eclipses.

Starspots

The $\approx$ 40 milli-magnitude variability of V819 Herculis A has been attributed to starspots. In the V819 Herculis system, the effect of a single, cold starspot is maximally $\sim 25\mu$as assuming a stellar radius of 0.8 mas. If multiple starspots cause the

Table 5.1
PHASES data for V819 Herculis

JD-2400000.5	δRA (mas)	δDec (mas)	$\sigma_{\rm min}$ (μas)	$\sigma_{\rm maj}$ (μas)	$\phi_{\rm e}$ (deg)	$\sigma_{\rm RA}$ (μas)	$\sigma_{\rm Dec}$ (μas)	$\frac{\sigma^2_{\rm RA,Dec}}{\sigma_{\rm RA}\sigma_{\rm Dec}}$	N
53109.4777819	49.6404	-84.4971	14.7	566.0	158.77	527.6	205.4	-0.99704	2011
53110.4800679	48.0940	-84.1339	23.7	1199.8	159.53	1124.1	420.3	-0.99818	1334
53123.4555720	49.1857	-85.9322	36.2	1015.6	162.47	968.5	307.9	-0.99239	1378
53130.4397626	48.4773	-86.4138	13.1	411.8	162.95	393.7	121.4	-0.99359	2537
53137.4279917	48.3926	-87.1400	27.9	560.7	164.34	539.9	153.7	-0.98203	1226
53145.3928594	48.3081	-87.8018	27.5	633.0	161.59	600.7	201.6	-0.98962	1673
53168.3368802	47.0273	-89.7517	30.1	680.1	162.93	650.2	201.7	-0.98777	1409
53172.3496326	47.3437	-90.1341	12.6	339.9	168.29	332.9	70.1	-0.98310	2560
53173.3294522	47.1580	-90.3605	16.0	154.8	33.97	128.7	87.5	0.97549	2904
53181.3314386	46.4330	-90.7861	15.0	349.0	169.71	343.4	64.1	-0.97112	2795
53186.3020911	45.6581	-91.1217	36.4	853.0	166.80	830.5	198.0	-0.98202	706
53187.3022539	46.1426	-91.2229	26.0	882.1	166.94	859.3	201.0	-0.99114	1578
53197.2663645	46.1848	-92.1526	9.5	234.1	164.87	226.0	61.8	-0.98714	5218
53198.2404599	46.2934	-92.2558	11.4	109.3	160.36	103.0	38.3	-0.94842	5404
53199.2897673	44.0250	-91.9450	49.2	3283.0	171.42	3246.2	492.3	-0.99487	946
53208.2505295	46.4281	-92.4906	13.2	362.5	37.67	287.1	221.8	0.99719	6558
53214.2391404	45.6333	-93.3432	10.9	251.7	169.45	247.5	47.3	-0.97195	5251
53215.2293360	45.6361	-93.5176	9.5	221.3	167.53	216.1	48.7	-0.97963	5723
53221.2207072	46.2536	-92.9732	17.6	683.9	38.91	532.3	429.8	0.99861	3998
53228.2083438	45.0879	-94.3314	14.4	201.2	169.45	197.8	39.5	-0.92815	3180
53233.1820405	45.0989	-94.8462	12.0	129.5	167.67	126.5	30.0	-0.91190	3303
53234.2006462	44.8264	-94.7640	15.2	75.7	172.74	75.1	17.9	-0.51361	3701
53235.2168202	45.2148	-94.9186	17.0	214.3	176.57	213.9	21.2	-0.60018	2094
53236.1665478	44.4594	-94.8865	9.5	156.1	166.59	151.9	37.4	-0.96553	6684
53481.5043302	30.4429	-103.3356	22.2	622.2	38.18	489.3	385.0	0.99730	3301

Table 5.1: PHASES data for V819 Herculis. All quantities are in the ICRS 2000.0 reference frame. The uncertainty values presented in this data have all been scaled by a factor of 2 over the formal (internal) uncertainties within each given night. Column 6, $\phi_{\rm e}$, is the angle between the major axis of the uncertainty ellipse and the right ascension axis, measured from increasing differential right ascension through increasing differential declination (the position angle of the uncertainty ellipse's orientation is $90 - \phi_{\rm e}$). The last column is the number of scans taken during a given night. The quadrant was chosen such that the larger fringe contrast is designated the primary (contrast is a combination of source luminosity and interferometric visibility).

variability, this effect is reduced. In addition, the effect of limb-darkening is to further reduce the astrometric error.

PHASES Observations During Ba-Bb Eclipses

Using the published sizes and temperatures for Ba and Bb from van Hamme et al. [1994], it is found that the magnitude of the astrometric shift in CL position during eclipse compared to what it would be outside of eclipse can be greater than 100 μas. Because this shift is larger than PHASES astrometric measurement precisions, six measurements taken during eclipse are omitted from the data tables and the fits.

5.2.3 Previous Differential Astrometry Measurements

Previously published differential astrometry measurements of the A-B (wide) system have been tabulated by Hartkopf et al. [2004] in the Fourth Catalog of Interferometric Measurements of Binary Stars. In several cases discrepancies were found between uncertainties quoted in the original works (or uncertainty estimates omitted in the catalog); in these cases the uncertainty estimates from the original works are used. All of these measurements were made using the technique of speckle interferometry. These measurements are included in the combined fit to help complete coverage of the A-B orbit.

Many of the previous differential astrometry measurements were published without any associated uncertainties. To allow these to be used in combined fits with other data sets, the average uncertainties were determined as follows. The uncertainties were initially assigned values of 10 milli-arcseconds in separation and 1 degree in position angle. A (single) Keplerian model was fit to the data, and residuals in separation and position angle were treated individually to remove outliers and update the uncertainty estimates. This procedure was iterated until uncertainties were found consistent with the scatter. A double Keplerian model (as in eq. 4.2, to allow for the Ba-Bb subsystem) does not improve the fit; the measurements are insensitive to this small signal. These 22 data points have average uncertainties of 5.92 milli-arcseconds and 0.689 degrees.

A Keplerian model was fit to the data points for which uncertainty estimates were available to determine whether these were systematically too large or too small, and to find outliers. The uncertainty estimates are found to be systematically too small; this factor was larger in position angle than in separation. Upon iteration, it was found that the separation uncertainties for these 12 data points needed to be increased by a factor of 2.43 and the position angle uncertainties by 3.53. Again no improvement was seen in fitting to a double Keplerian model.

5.2.4 Radial Velocity Data

A large number of radial velocity measurements of components A and Ba from four observatories were reported in Scarfe et al. [1994]. Scarfe et al. indicate several measurements as outliers; these measurements have not been used. There are 72

component A velocities and 50 component Ba velocities in the McDonald/Kitt Peak data set, 70 component A and 49 component Ba velocities in the DAO set, and 92 component A and 90 component Ba velocities in the DDO data set.

The velocity measurements for each of three data sets presented were fit to double Keplerian models separately to determine the average velocity uncertainties (measurements from McDonald and Kitt Peak were mixed together in the original work, and these were analyzed together as one group). As noted in Scarfe et al. [1994], the velocity precisions for component A differed from those of Ba. Uncertainties were derived for each data set by fitting to a double Keplerian model and examining the scatter in the residuals for each component separately. The uncertainty guesses were updated and the procedure iterated. The initial values for the component A velocities were 0.46 $\mathrm{km\,s^{-1}}$ for the McDonald/Kitt Peak and DAO data sets, and 0.92 $\mathrm{km\,s^{-1}}$ for the DDO set; for component Ba, all were set to 2 $\mathrm{km\,s^{-1}}$. The average A and Ba uncertainties are 0.43 $\mathrm{km\,s^{-1}}$ and 1.955 $\mathrm{km\,s^{-1}}$ for the McDonald/Kitt Peak velocities, 0.465 $\mathrm{km\,s^{-1}}$ and 3.025 $\mathrm{km\,s^{-1}}$ for the DAO measurements, and 1.015 $\mathrm{km\,s^{-1}}$ and 3.105 $\mathrm{km\,s^{-1}}$ for the DDO observations.

5.3 Orbital Solution and Derived Quantities

The best-fit combined astrometry-radial velocity orbital solution produces a set of parameters listed in Table 5.2. The reduced χ^2_r of the combined fit to PHASES, radial velocity, and previous differential astrometry data is 1.33. This combined set has 521 degrees of freedom with 20 parameters. This value for χ^2_r is slightly higher than one would expect, but this is likely due to the manner in which the uncertainties had to be derived. All parameter uncertainties have been increased by a factor of $\sqrt{1.33}$ to reflect this difference. Also presented is a table of derived parameters of direct astrophysical interest (5.3). A fit to the astrometric data alone does not constrain several of the orbital parameters, but does constrain apparent semi-major axes of the wide and narrow orbits to good precision: $a_{A-B} = 73.9 \pm 0.6$ mas and $a_{Ba-Bb} = 108 \pm 8\mu$as (Ba-Bb CL orbit).

The combined fit A-Ba-Bb orbit is plotted is Figure 5-1; PHASES measurements of the Ba-Bb orbit CL motion is plotted in Figure 5-2. Residuals to the combined fit are shown in Figures 5-3, 5-4, and 5-5; no evidence for additional system components is observed.

5.3.1 Mutual Inclination

The mutual inclination Φ of two orbits is given by

$$\cos\Phi = \cos i_1 \cos i_2 + \sin i_1 \sin i_2 \cos(\Omega_1 - \Omega_2) \tag{5.1}$$

where i_1 and i_2 are the orbital inclinations and Ω_1 and Ω_2 are the longitudes of the ascending nodes. From the combined orbit solution a value for this angle of 23.6 ± 4.9 degrees is derived for the V819 Her system. This low value is below the

Table 5.2
Orbital models for V819 Herculis

	PHASES + Pre. + RV
P_{A-B} (days)	2019.79 ±0.36
$T_{0,A-B}$ (MJD)	52628.1 ±1.3
e_{A-B}	0.6731 ±0.0015
i_{A-B} (degrees)	57.09 ±0.22
ω_{A-B} (degrees)	42.55 ±0.23
Ω_{A-B} (degrees)	322.40 ±0.16
P_{Ba-Bb} (days)	$2.2296337 \pm 1.9 \times 10^{-6}$
$T_{0,Ba-Bb}$ (MJD)	52627.18 ±0.30
e_{Ba-Bb}	0.0041 ±0.0033
i_{Ba-Bb} (degrees)	79.0 ±3.3
ω_{Ba-Bb} (degrees)	47 ±48
Ω_{Ba-Bb} (degrees)	312.9 ±4.8
$V_{0,M/K}$ (km s^{-1})	-3.388 ±0.059
$V_{0,DAO}$ (km s^{-1})	-3.373 ±0.064
$V_{0,DDO}$ (km s^{-1})	-3.35 ±0.12
M_A ($M_\odot$)	1.765 ±0.095
M_{Ba+Bb} ($M_\odot$)	2.512 ±0.067
M_{Bb}/M_{Ba}	0.757 ±0.020
L_{Bb}/L_{Ba}	0.261 ±0.045
d (parsecs)	67.96 ±0.87

Table 5.2: Orbit models for V819 Herculis. Pre.: Previous differential astrometry measurements. The luminosity ratio L_{Bb}/L_{Ba} is for K-band observations.

Table 5.3
Derived physical parameters

Parameter	Derived Value
a_{A-B} (AU)	5.108 ±0.046
a_{Ba-Bb} (AU)	0.0457 ±0.0004
$\cos\Phi$ (degrees)	23.6 ± 4.9

Table 5.3: Physical parameters for V819 Herculis derived from the combined orbital solution.

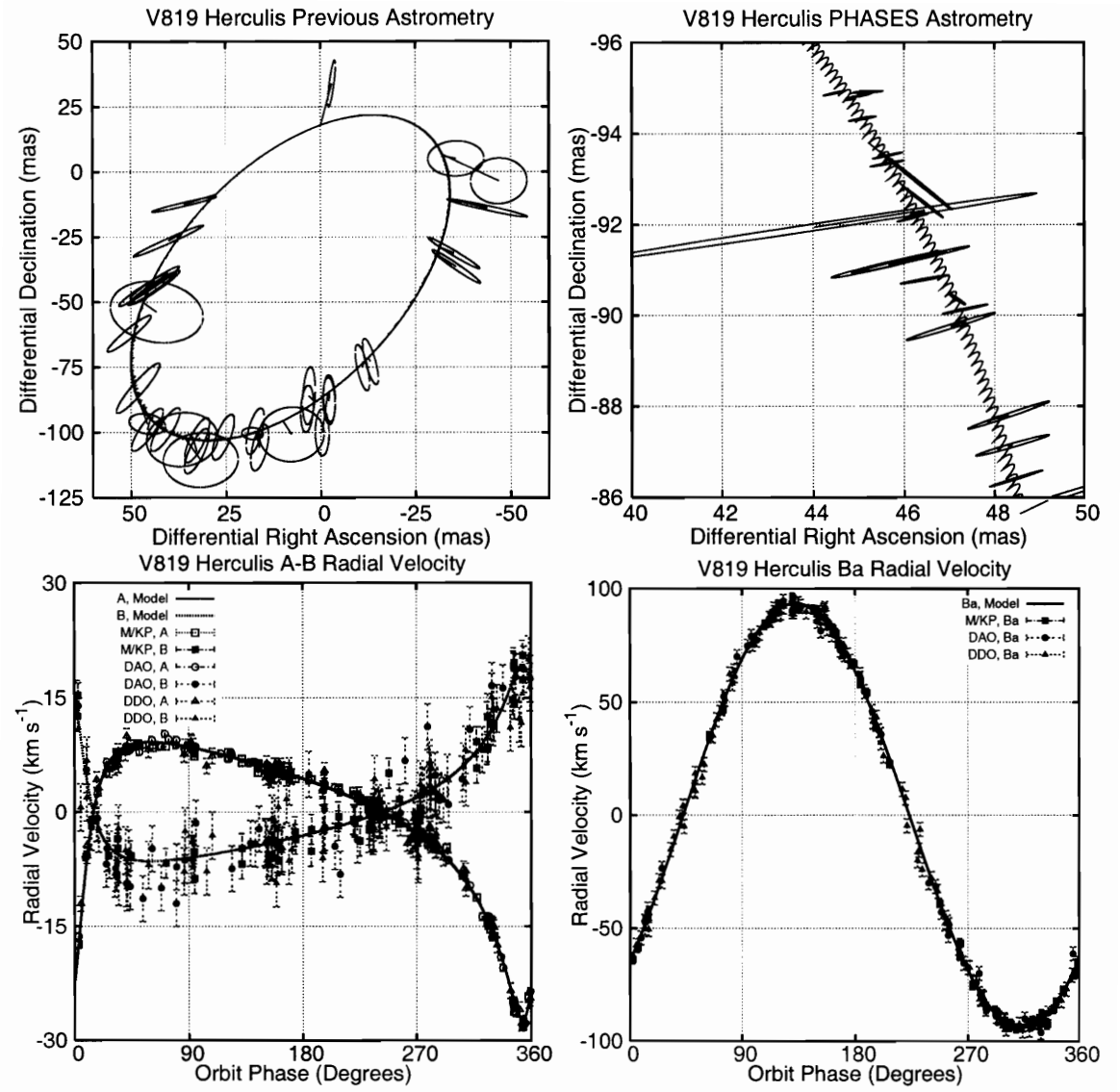

Figure 5-1: The orbit of V819 Herculis. (Top left) Previous (speckle) differential astrometry measurements with derived uncertainty ellipses. (Top right) One season of PHASES astrometry. (Bottom left) CM velocities of the wide pair. (Bottom right) Radial velocities of the Ba and Bb components. The A-B motion has been removed for clarity.

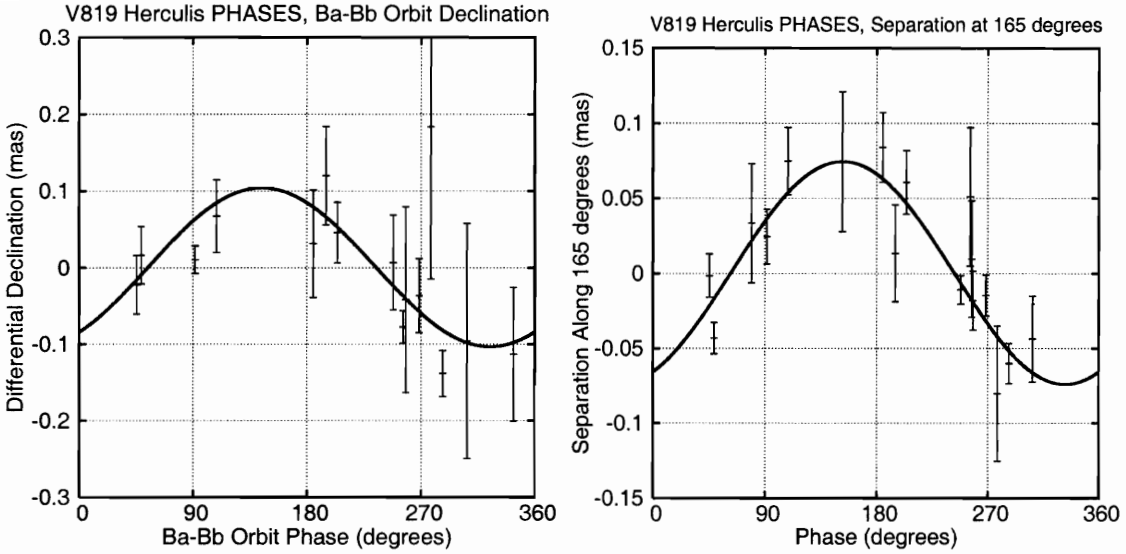

Figure 5-2: CL astrometric motion of the V819 Herculis Ba-Bb system, as measured by PHASES observations along the declination axis (left) and along an axis rotated 165 degrees East of North (equivalent to position angle 285 degrees; right); this is the median position angle of the minor axis of the PHASES uncertainty ellipses. The wide A-B orbital motion has been removed for both plots. The error bars plotted have been stretched by a factor of 2 over the formal uncertainties as discussed in the text. The high ellipticity of the uncertainty ellipses causes neither the right ascension nor the declination uncertainties to be near the precision of the minor axis uncertainties, which have median uncertainty of 15.2 μas. For clarity, measurements with projected uncertainties larger than 200 μas are not shown in the plots. Zero phase indicates periastron passage.

Table 5.4
Known Mutual Inclinations

	Mutual Inclination (degrees)	Reference
V819 Her	23.6 ± 4.9	This chapter.
κ Peg	43.8 ± 3.0	This thesis, chapter 4; [Muterspaugh et al., 2005b]
η Vir	30.8 ± 1.3	[Hummel et al., 2003]
ϵ Hya	39.4	[Heintz, 1996]
ξ UMa	132.1	[Heintz, 1996]
Algol	98.8 ± 4.9	[Lestrade et al., 1993], [Pan et al., 1993]

Table 5.4: Unambiguously known mutual inclinations of triple systems. The value for Algol is determined using the measurement precisions and values of Pan et al. [1993] for all but the A-B nodal position angle of 52 ± 5 degrees from Lestrade et al. [1993]

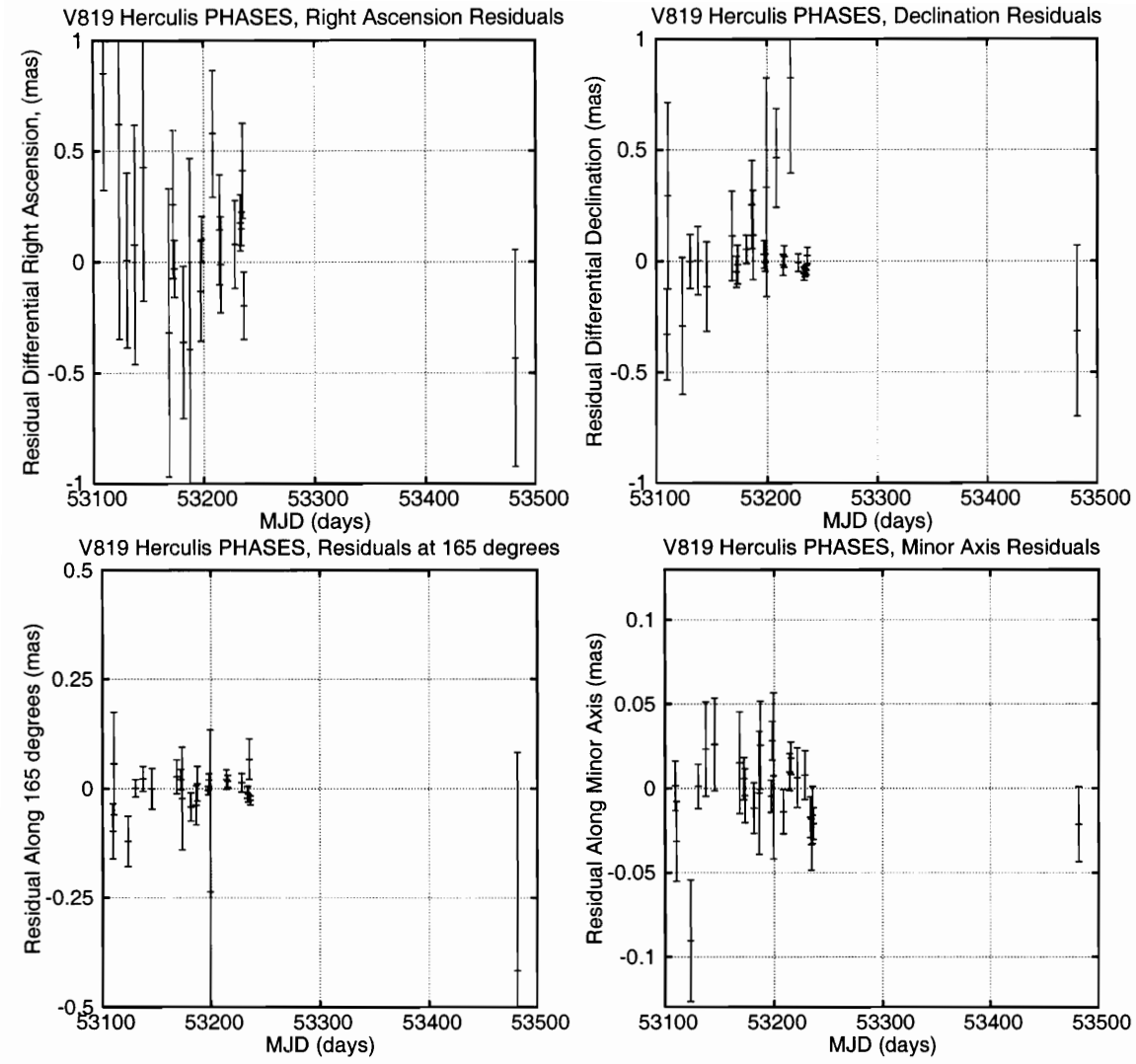

Figure 5-3: Residuals for PHASES differential astrometry of V819 Herculis. The error bars plotted have been stretched by a factor of 2 over the formal uncertainties as discussed in the text. The high ellipticity of the uncertainty ellipses causes neither the right ascension nor the declination uncertainties to be near the precision of the minor axis uncertainties, which have median uncertainty of 15.2 μas. Due to the roughly North-South alignment of the baseline used for most of the measurements, the more sensitive axis was typically declination. The right ascension and declination plots show only those points for which the projected error bar is less than 1 milli-arcsecond. The bottom left plot shows the residuals along a direction that is 165 degrees from increasing differential right ascension through increasing differential declination (equivalent to position angle 285 degrees), which corresponds to the median direction of the minor axis of the PHASES uncertainty ellipses; only measurements with uncertainties less than 500 μas along this axis are plotted. The bottom right plot shows residuals along the minor axis of each measurement's uncertainty ellipse.

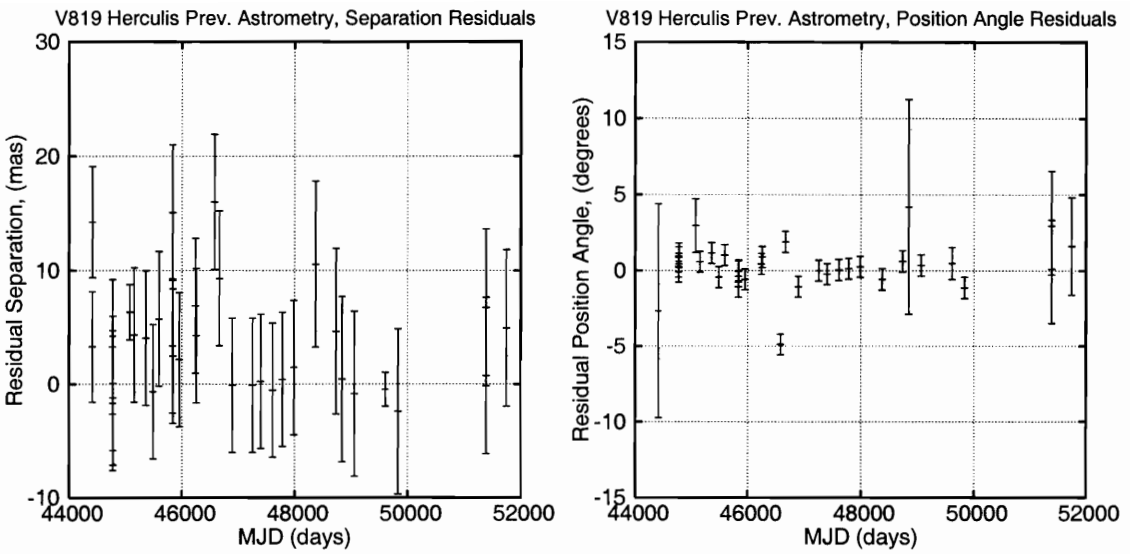

Figure 5-4: Residuals to the combined model for previous differential astrometry of V819 Herculis.

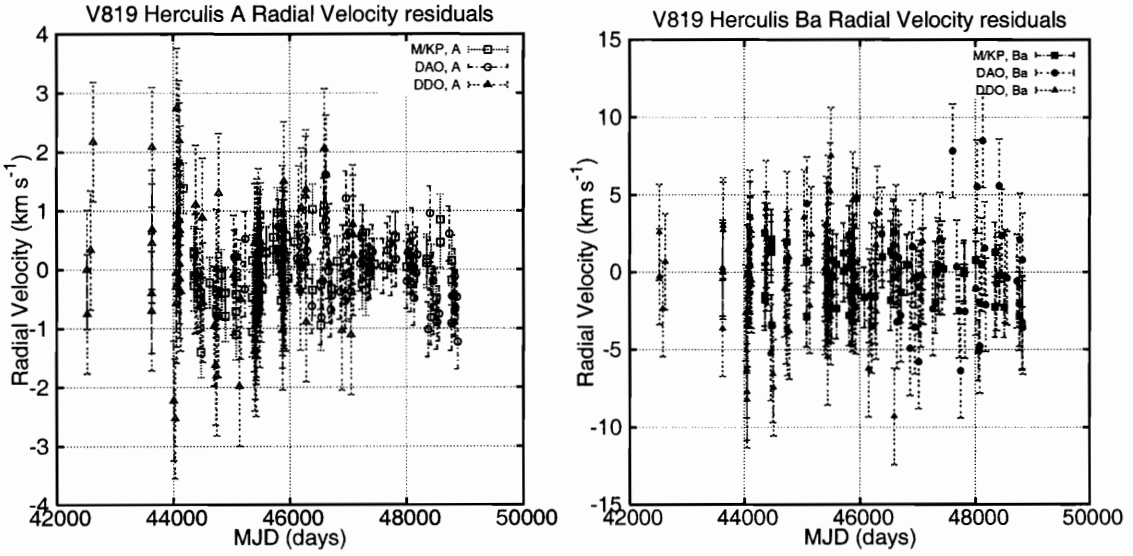

Figure 5-5: Residuals to the combined model for radial velocimetry of V819 Herculis [Scarfe et al., 1994].

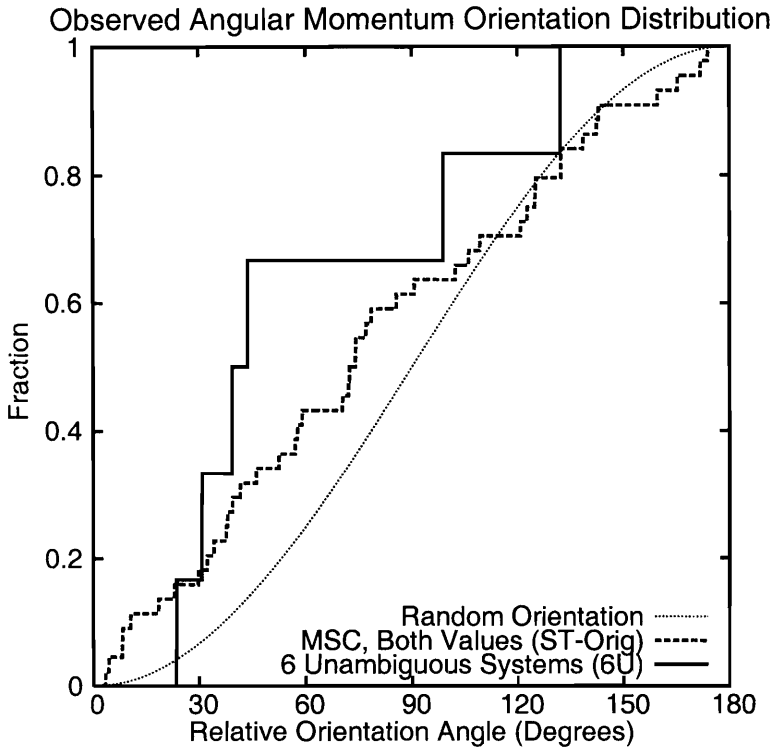

Figure 5-6: Cumulative distribution of the observed distribution of angles between angular momentum vectors of the six systems for which unambiguous mutual inclinations have been determined. This is compared with the results from Sterzik and Tokovinin [2002], who included 22 systems for which the mutual inclinations could only be determined ambiguously—two degenerate angles were both possible solutions due a 180 degree ambiguity in the longitude of the ascending node of at least one component of the triple system. Sterzik and Tokovinin included both possible angles in their distribution. Also shown is the theoretical distribution for random orientations.

limit for inclination-eccentricity oscillations derived by Kozai (1962; 39.2 degrees), and is consistent with the small measured value of the eccentricity of the Ba-Bb pair.

The mutual inclination of the orbits of triple systems is of particular interest for understanding the conditions under which the system formed [Sterzik and Tokovinin, 2002]. Without both radial velocity and visual (or astrometric) orbits for both systems in a triple, unambiguous determinations of the longitudes of the ascending nodes (and thus of the mutual inclination) are impossible. To date there has only been a very small number of cases where the mutual inclination can be unambiguously determined (Table 5.4).

With the tally of systems for which unambiguous mutual inclinations have been determined now at six, it is reasonable to consider the distribution of these orientations. The previous work on this subject is that of Sterzik and Tokovinin [2002], who determined theoretical distributions resulting from a variety of initial conditions within star forming regions. At the time, the authors cited only three systems from which mutual inclinations were known, listed in a previous work by one of them

[Tokovinin, 1993]. (One of these three, ζ Cnc, is most recently listed by Heintz [1996] as still having an ambiguous mutual inclination, and is not included here.) For comparison to real stars, Sterzik and Tokovinin instead included the 22 triple systems in the Multiple Star Catalog [Tokovinin, 1997] for which both visual orbits were known, but the ascending nodes had 180 degree ambiguities. To correct for this lack of information, for each system they included both possible mutual inclinations in a combined cumulative distribution (this distribution is referred to as ST). This procedure assumes the ambiguity is divided evenly between the lower and higher possible angles; i.e. that an equal number of the "true" mutual inclinations are the lesser of the two possible angles as are the greater.

In Figure 5-6 the continuous distribution function of mutual inclinations for the six unambiguous systems (this distribution is referred to as 6U) is plotted with ST and the theoretical distribution for random orientations (referred to simply as Random).

The two-sided Kolmogorov-Smirnov (K-S) probability for agreement between 6U and ST is 0.46; the one-sided KS probability between ST and Random is 0.07 and that for 6U and Random is 0.04. The 6U set confirms the result of Sterzik and Tokovinin [2002] that mutual inclinations are not consistent with random orientations and show a slight preference for coplanarity. The sets 6U and ST agree much better with each other than either do with random orientations, but the agreement probability is still low; this is likely due to the assumption inherent to forming the ST set by including both possible orientations, which dilutes the distribution away from coplanarity. A greater number of systems is required to better determine the distributions, and observational selection effects should also be considered.

5.4 Conclusions

PHASES interferometric astrometry has been used to measure the orbital parameters of the triple star system V819 Herculis, and in particular to resolve the apparent orbital motion of the close Ba-Bb pair. The amplitude of the Ba-Bb CL motion is only 108 ± 9 μas, indicating the level of astrometric precision attainable with interferometric astrometry. By measuring both orbits one is able to determine the mutual inclination of the two orbits, which is found to be 23.6 ± 4.9 degrees. Such a low mutual inclination implies a lack of Kozai oscillations.

Further improvement in determining the system distance and component masses will require improved radial velocity data. Given that the A component is evolved and the Ba-Bb system undergoes eclipses and hence the B components have accurately measured radii, this system may become a very fruitful laboratory for high-precision testing of stellar models.

Chapter 6

Detectability of Circumbinary Extrasolar Planets

Because the long-term stability of planets in binary systems is relatively well established, positive or negative results from searches for companions to binaries will help determine which planet formation models are realized in nature. All the confirmed planets found in binary systems thus far are in S-type orbits. The purpose of this chapter is to evaluate and compare several methods of detecting circumbinary (P-type) planets. If one stellar component is much brighter than all the other components, the methods used to detect extrasolar planets in single star systems can be used without significant change; there are indications that HD 202206 may be such a system [Correia et al., 2004] (in this case, one "stellar" component is thought to be a brown dwarf).

This chapter is primarily concerned with binaries with much smaller contrast ratios and the observational challenges they present. The application of observing programs designed to detect planets around single stars to instead search for circumbinary planets, outlines for modifications to these methods that improve their performances for detecting circumbinary planets, and detection methods unique to circumbinary systems are presented. First, the size scales of observable quantities is reviewed. In section 6.2, the response of stellar coronographs (such as might be used in the Terrestrial Planet Finder (TPF [Beichman, 1998]) missions) to two bright sources (stars) with a faint (planetary) companion is evaluated and an observing scheme that allows for simultaneous nulling of the light from both stars is developed; previous work on coronographs has only addressed the scenario for blocking the light from a single star. Section 6.3 reviews using the periodic apparent delays of binary eclipses caused by the light-time effect for indirect planet detections. In section 6.4 the best demonstrated radial velocity precision for unresolved binaries is reviewed. Two observable radial velocity effects are evaluated: first is the periodic variations of the binary system CM velocity (which is directly analogous to RV searches for planets around single-stars), and second is measuring periodic changes in the orbital phase of the binary caused by the light-time effect, a detection method that has not been previously addressed. In section 6.5 microlensing light curves for lenses consisting of binaries with planets and potential sources of confusion that might prevent one from

uniquely determining the nature of the lens are discussed. The method of detecting planets in edge-on orbits through photometric monitoring of their transits is extended to circumbinary systems in section 6.6, with simulated light curves for such systems and discussion of complications that arise due to the motions of the stars in their binary orbit. In section 6.7 the responses of high-precision astrometric instruments to unresolved or partially resolved binaries is discussed.

The contents of this chapter have been developed by the author with Dr. B. Lane and Dr. E. Pfahl.

6.1 Scale Sizes of Observables

To begin, the size scales of observable quantities are reviewed. A circumbinary planet causes a reflex motion of the binary center of mass (CM) that might be detected. The reflex motion has distance variations of size

$$\begin{aligned} \Delta a_{CM} &= 2\frac{M_p}{M_b}a_p \\ &= \frac{M_p/M_{\rm J}}{M_b/M_\odot}\frac{a_p}{524}. \end{aligned} \tag{6.1}$$

where M_p, M_b, $M_{\rm J}$, $M_\odot$ are respectively masses of the planet, binary, Jupiter, and Sun and a_p is the semimajor axis of the planet. This size variation changes not only the astrometric position of the binary CM, but (if correctly aligned) also adds delays in photon arrival times to Earth (the "light-time effect"). Converting the length reflex to light-seconds gives the magnitude of the light-time effect as

$$\begin{aligned} \Delta t &= 2\frac{a_p M_p \sin i_p}{cM_b} \\ &= 0.95\,\text{seconds} \times \frac{(a_p/1\,\text{AU})\,(M_p/M_{\rm J})\sin i_p}{M_b/M_\odot} \end{aligned} \tag{6.2}$$

where i_p is the inclination of the planet orbit. The reflex motion velocity variations are

$$\begin{aligned} \Delta v_b &= \frac{4\pi a_p M_p}{P\,(M_b+M_p)} \\ &= \frac{2\sqrt{G}M_p}{\sqrt{(M_b+M_p)\,a_p}} \\ &= 56.9\,\text{m}\,\text{s}^{-1} \times \frac{(M_p/M_{\rm J})}{\sqrt{((M_b+M_p)/M_\odot)\,(a_p/1\text{AU})}} \end{aligned} \tag{6.3}$$

where P is the planet orbital period and G is the gravitational constant (to convert to radial velocity motion, one must multiply by $\sin i_p$). Differential reflex motion and perturbations of the binary orbit by the planetary companion are expected to be

The "prototype" circumbinary planet system	
distance	10 pc
M_b	2 $M_\odot$
P_b	10 days
a_b	0.11 AU
	11 mas*
Θ_*†	$\frac{1}{2}$ mas
RV‡	$62 \sin i_b \,\mathrm{km\,s^{-1}}$
M_p	1 M_J
P_p	53 days
a_p	0.35 AU
	35 mas
Δa_{CM}	3.3×10^{-4} AU
	33 μas§
Δt	$\frac{1}{6} \sin i_p$ second
Δv_b	$68 \sin i_p \,\mathrm{m\,s^{-1}}$
Contrast	10^6 (near infrared), 10^8 (visible)

Table 6.1: Properties of the "prototype" circumbinary planet system.
* milli-arcseconds
† stellar diameter
‡ radial velocity of the binary orbit only
§ micro-arcseconds

negligible on reasonable timescales.

Though generalized detection criteria are developed for each method considered, references are made to a prototypical system to establish rough figures for required measurement precisions. The properties of a hypothetical system with two dwarfs (each 1 $M_\odot$) and circumbinary planet in a critically stable orbit are detailed in Table 6.1. The prototypical system is one of critical stability and only more widely separated planets are stable; velocity variations decrease for larger planet orbits (i.e. $68\,\mathrm{m\,s^{-1}}$ is the maximum signal for the prototype binary), whereas distance and time related quantities grow.

6.2 Direct Detection

Perhaps the highest payoff technique for studying extrasolar planets is direct detection; this type of detection has the potential to allow photometry, spectroscopy, polarimetry and a host of related studies, all of which can provide very useful information about such planets. Due to the extreme contrast ratio between a planet and its parent star, it is almost certain that any direct detection methods will require access to space. NASA is currently envisioning two complementary missions under

the rubric "Terrestrial Planet Finder" [Beichman, 1998]: a visible coronograph and a thermal-IR nulling interferometer. At the moment, these missions are intended only to study planets orbiting single stars. However, the ability to detect circumbinary planets would increase the versatility, scientific scope, and number of targets available. If circumbinary planets are common, this ability would also increase the number of successful detections, given that TPF is only expected to be able to detect planets within the nearest 10-15 pc, and hence the sample of candidate systems is currently rather limited. It is not immediately clear that either of the proposed architectures (a nulling interferometer or a coronagraph) will have this capability, but one should consider the various possibilities.

6.2.1 Coronographs

It is likely that the first TPF mission flown will be a large (6-8 meter) optical telescope equipped with some form of high contrast imaging system, either a coronograph or an apodized pupil. Such devices are designed to provide an extreme degree (10^{11}) of suppression of any light from an on-axis source, while leaving light from angularly nearby sources (separation $>$ 50 milli-arcseconds) unblocked. It is useful to think about the performance of such an instrument in terms of a "response function", i.e. the photon throughput as a function of position on the sky (measured with respect to the telescope pointing direction). Such response functions have regions of very low transmission governed by the details of how the suppression is achieved; in the simple case of a classical Lyot coronograph the suppression is provided by a circular blocking spot in an intermediate image plane (as well as a pupil plane mask to suppress diffraction effects). More complicated approaches involve the use of non-circular apertures (e.g. Gaussian prolate spheroids) to achieve very good suppression in particular directions at the expense of other regions. Another possible design is "band-limited masks", a variant of Lyot coronographs that uses multiple blocking spots, typically arranged in grating-like patterns. It is conceivable that a particular configuration could be arranged so as to block out light from multiple stars.

In the case of a binary system, there are three general configurations to consider: very close binaries, very wide binaries, and binaries of intermediate separation. In the case of very close binaries one can simply treat the stars as a single source and suppress both stars sufficiently to find any outer planets. However, it is not obvious that this will often be the case. In particular, the dominant source of starlight "leakage" is due to the finite angular diameter of the star (for a G-class star at 10 pc, this is $\sim$ 1 milli-arcsecond). The instruments being designed are tailored to maximize the searchable area and off-axis throughput (to maximize the planet signal); this requires minimizing the extent of the blocking region. Hence in order for the binary to be considered "close", it would essentially have to be a near-contact system.

Very wide binaries are another possibility. However, the scattered light from any nearby star will persist above the 10^{-11} level out to very considerable angular separations, on the order of tens of arcseconds or 100's of AU. At such separations, TPF-C (which observes planets by their reflected light) will be unable to find any planets, and hence in the widely separated binary case TPF-C could only be used to

find planets in S-type orbits.

The intermediate separation case is both the most likely to occur in the list of potential targets, and is possibly the most scientifically interesting. It is also the most challenging from an instrumental point of view. Clearly the blocking pattern will have to extend out to 10's of milli-arcseconds; this is only feasible in the context of an asymmetric nulling pattern (for which light is blocked along an entire axis of the image plane). Standard observing plans with asymmetric (typically linear) coronographs call for two or more exposures per observation with the telescope roll angle differing by $30 - 90$ degrees between exposures. This allows residual leakage (which rotates with the telescope) to be distinguished (i.e. subtracted) from any potential planet (which rotates with the sky). It also has the effect of placing the non-nulled regions (where a planet could be seen) at all possible locations around the star.

However, when observing a binary system, the telescope roll angle must be kept fixed with respect to the binary position angle in order to null both stars. This alignment must be held to within an angle $\delta\phi = \arcsin \delta\alpha/\rho$, where ρ is the binary separation as projected on the sky, and $\delta\alpha$ is the required pointing accuracy for a single star (the angle at which a star's light starts to only be partially nulled; the angle $\delta\alpha$ depends on the nulling response function (e.g. $\propto \theta^2$ or $\propto \theta^4$, where θ is the off-axis angle) and is typically of order 1–10 milli-arcseconds. Thus, $\delta\phi$ must be held to ~ 1 degree, well within the design capabilities of any proposed instrument. On the other hand, this makes the expose-roll-expose-subtract method more difficult, since the only possible roll angle would likely be 180 degrees. This may work, but it should be noted that residual starlight leakage due to wavefront error can often be point-symmetric on the image plane, which would negate the benefits of rolling. This general problem will require some further analysis, and if the possibility of detecting circumbinary planets is compelling enough, may direct the design of TPF-C.

For general binary configurations, only the portion of space in wedges perpendicular to the binary position angle can be nulled during any individual observation. In the special case of an eclipsing system, one can proceed with the standard observing strategies for single stars during eclipses (which typically last hours). For all other binaries, an observing procedure is introduced that increases the coverage of potential planet orbits. Because the binary is non-eclipsing, the position angle necessarily changes with orbital phase. The binary and planet orbital periods are necessarily unique. Thus, by waiting for the binary position angle to change due to orbital motion, one can re-observe and fill-in spatial coverage of all possible planet orbits.

While binary orbital motion allows one to survey the entire circumbinary space (between the instrumental inner- and outer-working angles), it also limits the integration times of individual observations, restricting the size of planets that can be detected. A single exposure can only be made over a time interval shorter than that during which the position angle changes by less than the angular alignment criteria $\delta\phi$. For a circular, face-on ten-day orbit, and $\delta\phi = 1$ degree, exposures are limited to roughly 40 minutes, severely limiting the sensitivity of the observation (typically ~ 10 hours for a single star).

6.2.2 A Nulling Interferometer

The TPF-I ("interferometer") mission is currently envisioned as a 100-meter baseline multi-aperture interferometer operating at a wavelength of 10 μm. Given this long wavelength of operation it must be cryogenic to reduce thermal backgrounds, and given the long baseline it is likely to require multiple spacecraft flying in formation. As if that was insufficiently challenging, the apertures have to be in the 2-4 meter diameter class.

The central starlight is nulled by combining beams with relative phase shifts very close to π, hence resulting in destructive interference on-axis. Note that given the configuration of four apertures stretched out on a line, the resulting acceptance function on the sky is a linear null (nulling regions stretch perpendicular to the projected baseline). The planet would be somewhat off-axis along the baseline direction, and so would not be nulled. Due to the limited angular resolution of the sub-apertures (~ 0.5 arcseconds), both the stellar leakage light and the planet light will end up on the same detector pixel. For this reason, the planet can only be detected by temporal modulation of the null pattern – in the simplest case by rotation of the entire instrument baseline around the axis pointing in the direction of the star. It is clear that such an approach is entirely incompatible with the presence of a binary companion.

6.3 Eclipse Timing

It has long been recognized that periodic shifts in the observed times of photometric minima of eclipsing binaries can indicate the presence of an additional component to the system (see, for example, Woltjer [1922], Irwin [1952], Frieboes-Conde and Herczeg [1973], Doyle et al. [1998]). The amplitude of the effect is given by eq. 6.2. As with RV measurements, there is a mass/inclination ambiguity; the following derivation assumes no correlation between binary and planet inclinations.

The precision with which eclipse minima can be timed is derived using standard χ^2 fitting techniques. Assume a photometric data set $\{y_i\}$ occurring at times $\{t_i\}$ with measurement precisions $\{\sigma_i\}$ and a model photometric light curve of flux $F(t-t_0)$ and corresponding intensity $I(t-t_0) = fF(t-t_0)\pi D^2 \Delta t/4$, where f $(0 \leq f \leq 1)$ is the fractional efficiency and throughput of the telescope, D is the telescope diameter, and Δt is the sample integration time. ($F(t-t_0)$ might be determined to high precision by observing multiple eclipse events.) The fit parameter t_0 is uncertain by an amount equal to the difference between the value for which χ^2 is minimized and that for which it is increased by one: $1 + \chi^2(t_0) = \chi^2(t_0 + \sigma_{t_0})$.

$$
\begin{aligned}
1 + \sum_{i=1}^{N} \left(\frac{y_i - I\left(t_i - t_0\right)}{\sigma_i} \right)^2 &= \sum_{i=1}^{N} \left(\frac{y_i - I\left(t_i - t_0 - \sigma_{t_0}\right)}{\sigma_i} \right)^2 \\
&\approx \sum_{i=1}^{N} \left(\frac{y_i - I\left(t_i - t_0\right) - \left(\frac{\partial I(t)}{\partial t}\right)_{t_i - t_0} \sigma_{t_0}}{\sigma_i} \right)^2
\end{aligned}
$$

$$= \sum_{i=1}^{N} \left(\left(\frac{y_i - I\left(t_i - t_0\right)}{\sigma_i} \right)^2 + \left(\frac{\left(\frac{\partial I(t)}{\partial t} \right)_{t=t_i-t_0} \sigma_{t_0}}{\sigma_i} \right)^2 - 2 \frac{\left(\frac{\partial I(t)}{\partial t} \right)_{t=t_i-t_0} \left(y_i - I\left(t_i - t_0\right)\right) \sigma_{t_0}}{\sigma_i^2} \right)$$

Because t_0 is the minimizing point, the first derivative of χ^2 at t_0 is zero.

$$\begin{aligned} \left(\frac{\partial \chi^2(t)}{\partial t} \right)_{t=t_0} &= 2 \sum_{i=1}^{N} \frac{\left(\frac{\partial I(t)}{\partial t} \right)_{t=t_i-t_0} \left(y_i - I\left(t_i - t_0\right)\right) \sigma_{t_0}}{\sigma_i^2} \\ &= 0 \end{aligned}$$

Rearrangement of terms leads to

$$\begin{aligned} \sigma_{t_0} &= \frac{1}{\sqrt{\sum_{i=1}^{N} \left(\frac{\left(\frac{\partial I(t)}{\partial t} \right)_{t=t_i-t_0}}{\sigma_i} \right)^2}} \\ &\approx \frac{\sigma_I}{\sqrt{\sum_{i=1}^{N} \left(\frac{\partial I(t)}{\partial t} \right)_{t=t_i-t_0}^2}}. \end{aligned} \tag{6.4}$$

An eclipse of length τ is approximated as a trapezoid-shape light curve with maximum and minimum photon fluxes F_0 and $F_0(1 - h/2)$ (h is a dimensionless positive number producing an eclipse depth of $hF_0/2$; in the case of a faint secondary, h is roughly twice the ratio of the squares of the stellar radii, $2R_2^2/R_1^2$). The ingress and egress are each assumed to be of length $k\tau/2$ ($k \approx 2R_2/(R_1 + R_2)$ is unity in the case of an eclipsing binary with components of equal size, when the trapezoid becomes a "V"-shape). Only the portions of the light curve during ingress and egress have nonzero $\frac{\partial F(t)}{\partial t}$ (in more accurate models, the light curve slope will be nonzero but small in other regions, and will not contribute much to the sum); this slope is $\left| \frac{\partial F(t)}{\partial t} \right| = hF_0/(k\tau)$. The number of data points contributing to the sum is thus $N = gk\tau/\Delta t$, where $0 \leq g \leq 1$ is the fraction of the eclipse observed (and also accounts for the fraction of time lost to camera readout) and Δt is the integration time for each measurement. In functional form, this model is:

$$F(t - t_0) = \begin{cases} F_0 & & t - t_0 & \leq -\tau/2 \\ F_0\left(1 - ht/\left(k\tau\right) - h/\left(2k\right)\right) & -\tau/2 \leq & t - t_0 & \leq -\tau/2 + k\tau/2 \\ F_0\left(1 - h/2\right) & -\tau/2 + k\tau/2 \leq & t - t_0 & \leq \tau/2 - k\tau/2 \\ F_0\left(1 + ht/\left(k\tau\right) - h/\left(2k\right)\right) & \tau/2 - k\tau/2 \leq & t - t_0 & \leq \tau/2 \\ F_0 & \tau/2 \leq & t - t_0 & \end{cases} \tag{6.5}$$

(also, see Figure 6-1).

The measurement noise σ_I is given by

$$\sigma_I = \left(I + \sigma_{sc}^2 + I_{bg} + n_{dark}\Delta t + \sigma_{rn}^2 \right)^{\frac{1}{2}} \tag{6.6}$$

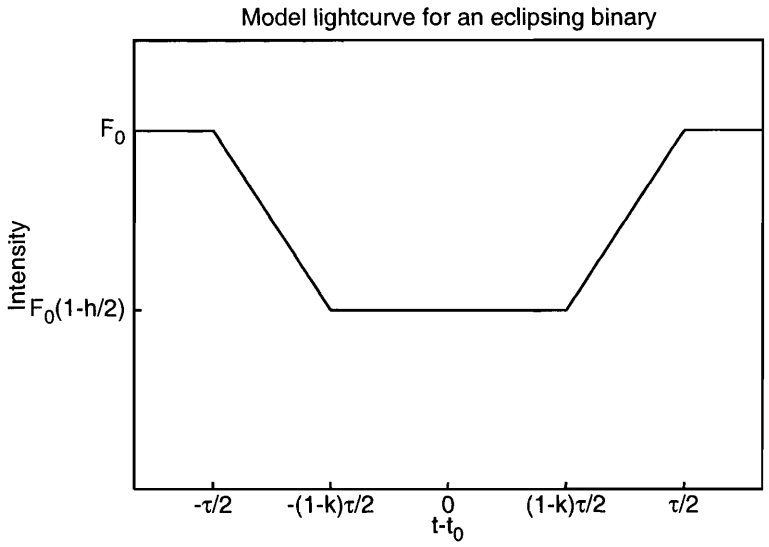

Figure 6-1: Eclipsing binary model light curve.

where $I_{bg} = fF_{bg}\pi D^2 \Delta t/4$ is is the sky background, n_{dark} is detecter dark current, σ_{rn} is detector read noise, and σ_{sc} is scintillation noise given by Young [1967] as

$$\sigma_{sc} = 0.09I\,(D/1\,\mathrm{cm})^{-2/3}\,Xe^{-h/(8000\,\mathrm{m})}/\,(2\Delta t/1\,\mathrm{second})^{\frac{1}{2}} \tag{6.7}$$

$$\approx 0.003I\,(D/1\,\mathrm{m})^{-2/3}\,/\,(\Delta t/1\,\mathrm{second})^{\frac{1}{2}} \tag{6.8}$$

where X is the airmass and h is the altitude of the observatory. The drop in noise during eclipse is ignored (a factor less than ≈ 1.4) and equation 6.6 is combined with equation 6.4 to obtain an overall timing precision (in seconds) of

$$\sigma_{t_0} = \sqrt{\frac{k\,(\tau/1\,\mathrm{second})}{gh^2}}\left(\frac{4}{fF_0\pi\,(D/1\,\mathrm{m})^2}+\frac{9\times10^{-6}}{(D/1\,\mathrm{m})^{4/3}}+\frac{\pi D^2 fF_{bg}/4+n_{dark}+\sigma_{rn}^2/\,(\Delta t/1\,\mathrm{second})}{f^2F_0^2\pi^2\,(D/1\,\mathrm{m})^4/16}\right)^{\frac{1}{2}}$$

$$\approx 0.18\,\mathrm{seconds}\times\sqrt{\frac{k\,(\tau/1\,\mathrm{hr})}{fgh^2}}\left(\frac{10^{(V-12)/2.5}}{(D/1\,\mathrm{m})^2}+\frac{f}{(D/1\,\mathrm{m})^{4/3}}\right)^{\frac{1}{2}}. \tag{6.9}$$

The final term in the first line (associated with dark current, read noise, and background) is generally smallest and will be ignored. In most cases, the term associated with scintillation is dominant.

Dividing the precision of an individual measurement by $N_{obs}-6$ (where N_{obs} is the number of eclipses observed and there are 6 parameters to a timing perturbation fit, two periods and the eccentricity, angle of periastron, epoch of periastron, and mass ratio of the wide pair), converting F_0 to V magnitude, and combining eq. 6.9 with that for the timing effect of reflex motion (eq. 6.2) gives a minimum detectable mass companion of

$$M_p = 0.19M_\mathrm{J}\times\sqrt{\frac{k\,(\tau/1\,\mathrm{hr})}{fgh^2\,(N_{obs}-6)}\frac{M_b/M_\odot}{(a_p/1\,\mathrm{AU})\sin i_p}}\left(\frac{10^{(V-12)/2.5}}{(D/1\,\mathrm{m})^2}+\frac{f}{(D/1\,\mathrm{m})^{4/3}}\right)^{\frac{1}{2}}. \tag{6.10}$$

For a meter-class telescope, the sensitivity to circumbinary planets is limited by (source brightness independent) scintillation noise for objects brighter than about twelfth magnitude. This noise term does not apply for space-based telescopes.

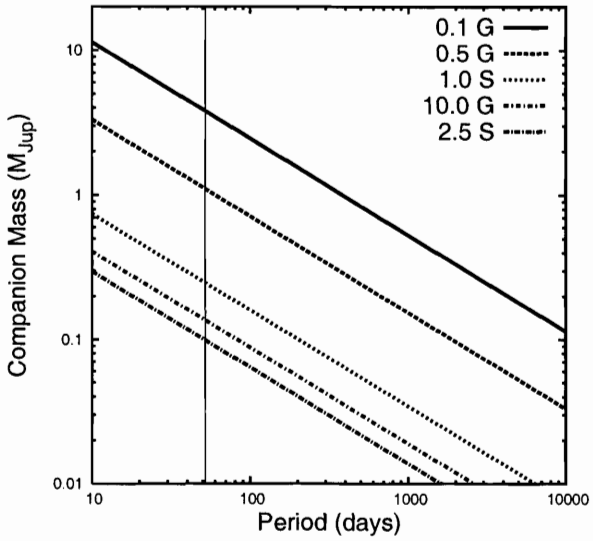

Figure 6-2: Sensitivity of eclipse timing measurements to circumbinary planets. The vertical line represents the approximate critical orbit around a 10-day period binary. The calculations assume the binary consists of two stars each massing 1 $M_{\odot}$, 6 hour eclipses, $N_{obs} = 25$ observations (150 total hours of data), $V = 10$ magnitudes, and 1-σ detections. From top to bottom, lines show sensitivity for $D = 0.1$ m on the ground, $D = 0.5$ m on the ground, $D = 1.0$ m in space (i.e. Kepler), $D = 10$ m on the ground, and $D = 2.5$ m in space (HST, SOFIA).

Eclipse timing observations require long observations on a telescope (the prototypical system analyzed has 6-hour long eclipses, and many eclipses must be measured to search for perturbations). A ground-based, high-speed photometric camera of modest size (≈ 50 cm) can detect Jupiter-like planets in AU-scale orbits for nearly 100 known eclipsing systems. Eclipse timing programs have been attempted in the past (see, for example, Frieboes-Conde and Herczeg [1973], Deeg et al. [2000]), but only on a few targets of particular interest. Modern detectors coupled with robotic telescopes can expand these programs to statistically significant searches for circumbinary planets.

One might also inquire about the sensitivity of this technique to outer planets in systems comprised of a single star and a transiting "hot" Jupiter. In this case, $h \approx 2R_p^2/R_{star}^2 \approx 0.02$ and $k \approx 2R_p/(R_{star} + R_p) \approx 0.18$, the "binary" is half as massive, and the eclipse duration is half as long. The companion sensitivity drops by a factor of 8, and the technique is (barely) in the range of detecting additional companions of planet mass. However, for the typically $V = 10$ magnitude transiting planet systems being discovered, 3 $\mathrm{m\,s^{-1}}$ radial velocity observations are more sensitive than half-meter telescope transit timing for companions with periods up to 60 years; even for observatories such as HST and SOFIA (for which scintillation noise is small or zero), this transition occurs at 15 year period companions.

Systematic and astrophysical noise sources may have effects that limit the actual precisions achieved. Mass transfer between stars can cause drifts in orbital periods. Variations of this type are non-periodic, distinguishing them from companion signals. Applegate [1992] has shown that gravitational coupling to the shapes of magnetically active stars can cause periodic modulations over decade timescales. This mechanism requires the star to be inherently variable; false positives can be removed using the overall calibrations of photometric data. It is possible that star spots will have large effects on timing residuals that are particularly difficult to calibrate [Watson and Dhillon, 2004]. Due to orbit-rotation tidal locking, the effect of a starspot on the light curve can be detected from the light curves of several orbits, and starspot fitting potentially can remove the timing biases introduced.

6.3.1 S-Type Planet Detections via Eclipse Timing

As an interesting side-note, one can also evaluate the potential for this method to detect S-type planets (or similarly moons of transiting planets). For this evaluation it is assumed that the depth of the planet (or moon) eclipse is sufficiently small as to be ignored (in such a detection, one could then reevaluate light curves to look for such transit signals) and the binary orbit is circular. In this case, the equivalent to eq. 6.2 is determined by the velocity of the binary orbit and the offset of the star-planet CM from that of the star by itself as

$$\begin{aligned}\Delta t &= x_{CM}/v_b \\ &= \left(\frac{P_b}{2\pi a_b}\right)\left(\frac{a_p \cos\phi M_p}{M_2+M_p}\right) \\ &\approx 57\,\text{seconds} \times (P_b/\text{month})\,\frac{a_p}{a_b/7}\,\frac{M_p/M_\text{J}}{M_2/M_\odot}\cos\phi \end{aligned} \tag{6.11}$$

where M_2 is the mass of star 2 (or the transiting planet, assumed to host the S-type companion), M_p is the mass of the S-type object orbiting M_2, and ϕ is the relative inclination of binary and planet orbits. The timing delays are not due to the light-time effect, but rather to the orbit of M_2 about the M_2-M_p CM. The factor of 7 appears in the final form because an S-type planet is typically stable if its semimajor axis is less than a seventh that of the binary; the above is thus an upper limit for the timing effect. Converting the semimajor axis to orbital periods,

$$\begin{aligned}\Delta t &\approx 41\,\text{seconds} \times (P_b/\text{month})^{\frac{1}{3}}\,(P_p/\text{day})^{\frac{2}{3}}\,\frac{M_p/M_\text{J}}{\left(M_b^{\frac{1}{3}} M_2^{\frac{2}{3}}\right)/M_\odot}\cos\phi \\ &\approx 65\,\text{seconds} \times (P_b/\text{month})^{\frac{1}{3}}\,(P_p/\text{day})^{\frac{2}{3}}\,\frac{M_p/M_\text{J}}{M_b/M_\odot}\cos\phi \end{aligned} \tag{6.12}$$

where M_1 is the mass of star 1 (which is assumed to have no planet) and $M_b = M_1 + M_2 + M_p$. The final form assumes $M_1 \approx M_2$, in which case the maximum stable

planet period is a thirteenth that of the binary period, implying days and months are the natural units for each respectively. The equivalent relationship for a moon orbiting an eclipsing Jupiter is

$$\Delta t \approx 13.3\,\text{seconds} \times (P_b/\text{month})^{\frac{1}{3}}\,(P_p/\text{day})^{\frac{2}{3}}\,\frac{M_p/M_\oplus}{(M_b/M_\odot)^{\frac{1}{3}}\,(M_2/M_\text{J})^{\frac{2}{3}}}\cos\phi \qquad (6.13)$$

where now the b subscript refers to the star-Jupiter analog system and p to the Jupiter analog's moon, and $M_\oplus$ is the mass of the Earth.

Equation 6.9 indicates that a meter-class ground-based telescope can time a giant planet transit ($h \approx 0.02$, $k \approx 0.18$) to approximately 9.4 seconds in the regime where the photometric precision is dominated by scintillation noise, assuming a Jupiter sized planet orbiting a star of solar size and mass with period of a month (implying 6-hour duration eclipses). This precision is sufficient to find Earth mass moons. For bright stars, space-based observatories offer even better precisions. Unfortunately, no transiting exoplanets with periods this long have yet been discovered.

It is possible that systems of this type may host the only Earth-like planets that can be positively confirmed by photometric missions such as Kepler. In such a scenario, a transiting Jupiter can be positively confirmed by ground-based radial velocity observations. Once this has been established, variations in the transit times would be used to detect Earth-sized moons. Because these photometric missions have limited lifetimes ($\approx$ 3 years), detections of moons are only possible for short period (few months or less) Jupiters, for which many transit events can be observed (unless a follow-up ground-based campaign is pursued with large telescopes). If the planet/moon are to be in the habitable zone, one must look for such systems around late-type (cool) stars. It is possible that such systems have the greatest likelihood of being habitable; the Jupiter-like planet would ensure that the Earth-sized moon has day/night cycles and stabilize its rotational axis similar to the way in which the Earth's is stabilized by its own moon. Both of these conditions have been argued as favorable for life [see, for example, Laskar et al., 1993].

6.4 Radial Velocity Observations

A circumbinary planet will exhibit two indirect effects on the velocities of the stellar components of the system. The apparent system velocity will vary in a periodic manner due to the motion of the binary about the system barycenter. The light-time effect will cause apparent changes in the phase of the binary orbit. These effects may be detectable using modern observational techniques.

The first effect is that the binary will exhibit periodic changes in the apparent system velocity; this is the same effect as seen in a single star. However, it may be harder to detect for three reasons: (1) the binary system is usually more massive than a single star of the same magnitude, (2) extremely short-period planet orbits (to which system velocity measurements are most sensitive) are unstable around binaries, and (3) the presence of two sets of spectral lines may complicate the measurement.

The recent work by Konacki [2004] demonstrates a method for obtaining velocity precisions of $20\,\mathrm{m\,s^{-1}}$ for equal magnitude unresolved binaries. While this is an order of magnitude worse than for isolated stars, it is a factor of ten better than previous work on binaries, potentially allowing for detections of P-type and S-type planets. Equation 6.3 shows that a planet in a critical orbit causes the binary to move about its barycenter by $\approx 70\,\mathrm{m\,s^{-1}}$, with the amplitude decreasing as the square root of planet orbit semimajor axis. Radial velocity observations with the $20\,\mathrm{m\,s^{-1}}$ precision demonstrated with Konacki's method can detect Jupiter-like planets in orbits of size ≈ 4 AU or less, down to the critical orbit.

The second observable effect is the additional light travel time as the binary system undergoes reflex motion caused by the planet. The magnitude of this effect is given in eq. 6.2. This is the same effect that causes eclipse timing variations. However, even in a non-eclipsing system this effect will still be detectable with radial velocity measurements.

Following a similar derivation as that for finding the expected precision of eclipse timing, one finds the precision with which one can estimate the orbital phase of a binary based on radial velocity measurements is

$$\sigma_\phi = \frac{\sigma_{rv}}{\sqrt{\sum_i (\frac{\partial v_i}{\partial \phi})^2}} \tag{6.14}$$

where σ_{rv} is the radial velocity measurement precision and $\frac{\partial v_i}{\partial \phi}$ is the derivative of the model radial velocity curve with respect to orbital phase, evaluated at times i. The timing precision corresponding to the phase precision derived is given by $\frac{\sigma_\phi}{2\pi} = \frac{\sigma_t}{P}$.

Approximating the binary orbit as circular, $v(t) \approx K \cos\left(\frac{2\pi t}{P_b} + \phi\right)$. If N measurements (each with two measured velocities, one for each star) are approximately evenly distributed in phase,

$$\sigma_\phi = \frac{\sqrt{2}\sigma_{rv}}{\sqrt{(2N-12)}K} \tag{6.15}$$

$$\sigma_t = \frac{P_b \sigma_{rv}}{\sqrt{2\,(2N-12)}\pi K}, \tag{6.16}$$

where 12 is the number of degrees of freedom for the model.

If the lines from both stars are observed, the effective K is $K1 + K2$ and the resulting $(1-\sigma)$ minimum detectable mass is thus

$$M_p = 41.4 M_\mathrm{J} \times \frac{(\sigma_{rv}/20\,\mathrm{m\,s^{-1}})\,(P_b/10\,\mathrm{days})^{4/3}\,(M_b/M_\odot)^{2/3}}{\sqrt{2N-12}\sin i_b \sin i_p\,(a_p/1\,\mathrm{AU})} \tag{6.17}$$

where i_b and i_p are the inclinations of the binary and planet orbits, respectively. Twenty-five $20\,\mathrm{m\,s^{-1}}$ radial velocity measurements of the "prototypical" system could detect moderate-mass brown dwarfs ($\approx 30 M_\mathrm{J}$) at critical orbit. Objects at the planet/brown dwarf threshold of 13 M_J are only detectable in orbits larger than 0.82 AU around a ten-day binary of sunlike stars. Alternatively, if only one set of

lines are observed, the resulting expression is

$$M_p = 41.4 M_J \times \left(1 + \frac{M_1}{M_2}\right) \frac{(\sigma_{rv}/20\,\mathrm{m\,s^{-1}})\,(P_b/10\,\mathrm{days})^{4/3}\,(M_b/M_\odot)^{2/3}}{\sqrt{N-11}\,\sin i_b \sin i_p\,(a_p/1\,\mathrm{AU})} \tag{6.18}$$

where M_1 is the mass of the star whose lines are observed, and M_2 is that of the faint star.

High precision radial velocity observations are only possible on slowly rotating ($v \sin i < 10\,\mathrm{m\,s^{-1}}$) stars; measurements of more rapidly rotating stars are limited by line broadening to levels worse than the nominal $20\,\mathrm{m\,s^{-1}}$ that has been referenced by this work. This effect is particularly important for finding planets around short-period binaries, in which the stars' rotation rates are often tidally locked to the binary orbital period; these rotation rates limit the observed precisions for systems with periods approximately five days or less.

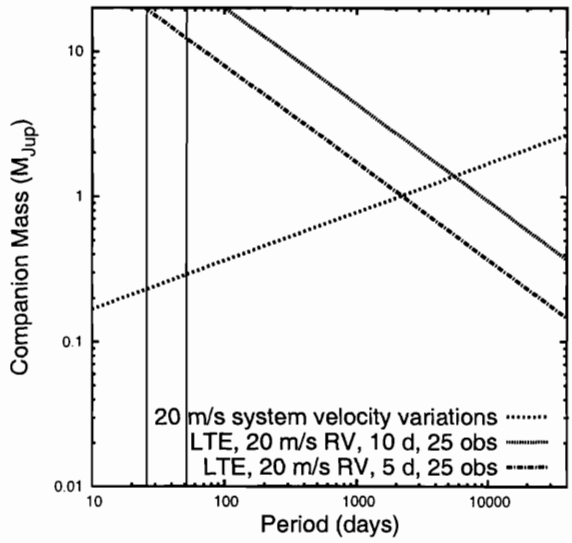

Figure 6-3: Sensitivity of radial velocity measurements to circumbinary planets. The two vertical lines at the left represent the approximate critical orbits around 5-day (to the left) and 10-day period binaries. Stars whose rotation rates are tidally locked to orbital periods less than about 5 days show sufficient rotational line broadening to prevent $20\,\mathrm{m\,s^{-1}}$ radial velocity precisions. The calculations assume the binary consists of two stars each massing 1 $M_\odot$.

6.5 Microlensing

Microlensing of background stars by foreground binaries with planets share many properties with lensing by a single star plus planet. Microlensing events provide high signal-to-noise detections of system components for even terrestrial mass planets, a positive aspect shared by both single and multiple component lenses. Microlensing by multiple star lenses are expected to occur with similar frequency as that by single

stars if the binary frequency for lenses is similar to that found in local stars (57%). A disadvantage of microlensing is that the total number of microlensing events observed is quite low because they require specialized alignments, and such alignments are very unlikely to repeat for any give lens. For this section, the "prototypical" system is modified by placing it much further away from Earth (several kiloparsecs) as microlensing by nearby systems is extremely unlikely.

In addition to these standard advantages and disadvantages of microlensing planet searches, binary star lenses have extra disadvantages due to source complexity, modeling confusion, and model degeneracies. Ground-based observations of microlensing events provide information about what is essentially a single chord across the lens system. The mass distribution of the lens is determined by fitting the observed light curve of a microlensing event. For mass distribution models consisting of only a few (1-2) static point masses, this fitting procedure is straight-forward. However, as one adds more degrees of freedom to the fit (more point masses, non-stationary components, complex source morphology), the light curves from several very different model mass distributions resemble each other and become degenerate.

As an illustration of model confusion, a microlensing detection of a circumbinary planet was announced for the system MACHO-97-BLG-41 [Bennett et al., 1999]. An alternative, simpler model of the same light curve has been suggested by Albrow et al. [Albrow et al., 2000], consisting of a binary lens (without planet) that shows orbital motion over the timescale of observations (a few months). The original work assumed a static system. The second model, of just a binary system undergoing Keplerian orbital evolution, is clearly more simple than the first and is thus more likely. Additionally, the second team had extra measurements of portions of the light curve in which the two models show differences which favored the second model (without a planet). In this model-degenerate regime, it appears the contribution of microlensing observations will be limited for detecting circumbinary systems, whose mass distributions have extra complexity due to the number of system components.

An alternative approach might be to launch a number of photometric telescopes into space. A set of such telescopes separated by tenths of an AU could map several chords across the mass distributions of lenses, providing more information that might be used to lift degeneracies between complex models.

6.6 Transiting Circumbinary Planets

Photometric surveys for transiting extrasolar planets have started to find several candidates around isolated stars [Charbonneau et al., 2000, Torres et al., 2003, Alonso et al., 2004]. Binary stars—particularly the unresolved systems that would be potential hosts for circumbinary planets—are problematic for transit surveys as they can cause both false positives (in the cases of grazing eclipses, eclipsing M-dwarfs, or eclipsing subsystems in unresolved triples) and false negatives (due to a diminished transit depth). The likelihood of a circumbinary planet transiting at least one of its host stars, the observed signal, and potential sources of confusion that may lead to false positives are considered.

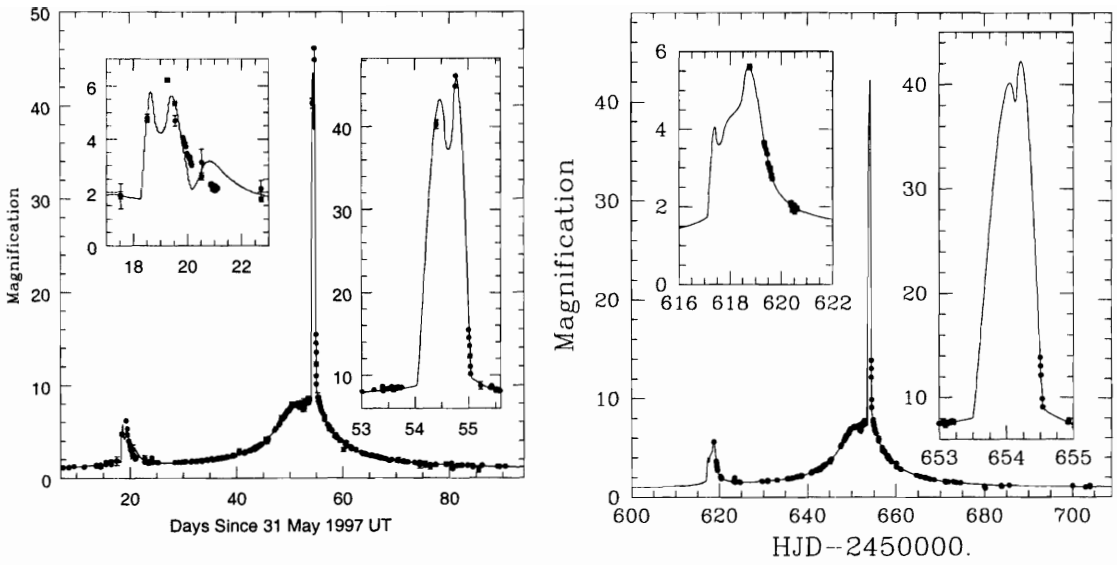

Figure 6-4: Microlensing of MACHO-97-BLG-41 with light curve models representing (left) a static binary system with circumbinary planet and (right) a rotating binary without planets. The discrepant measurements in the left inset were not originally available to Bennett et al. [1999], who concluded the light curve represented a binary with outer planet. The rotating binary model is favored by the additional measurements. These graphs were provided by the PLANET collaboration.

The probability that a randomly oriented planetary orbit is seen to transit its host star in a non-binary system is given by [Gilliland et al., 2000]

$$Pr = 23.8\% \times \left(\frac{M_*}{M_\odot}\right)^{-1/3} \frac{\Theta_*}{\Theta_\odot} \left(\frac{P}{\text{day}}\right)^{-2/3} . \tag{6.19}$$

Two factors cause the probability of circumbinary planet transits to differ from the results for single stars. First, the probability is lowered by the fact that the shortest period orbits (with highest chance to be seen as transiting) are dynamically unstable. Whereas exoplanets have been detected with periods as short as one day (with roughly 24% chance to transit), these high probability planets would not be found orbiting two stars.

The second effect altering the probability of circumbinary planet transits is that the stars move in their orbits. Consider a binary comprised of stars 1 and 2 with masses M_1 and M_2 and radii R_1 and R_2. Assume, for simplicity, that the binary orbit is circular and that the relative separation of the stars is a_b. Likewise, suppose that the circumbinary orbit of the planet is circular with separation a_p from the binary center of mass. Here it is assumed that the mass of the planet is negligibly small. Let the binary and planetary orbits have inclinations i_b and i_p relative to the plane of the sky. Define Ω as the angle between the projected major axes of the orbits; see Figure 6-5.

The necessary, but not sufficient, condition for the planet to transit star 1 is that the projected minor axis of the planetary orbit, $a_p \cos i_p$, must be smaller than the maximum perpendicular distance of star 1 from the projected major axis of the planetary orbit, plus the stellar radius. The mathematical condition is

$$a_p \cos i_p < R_1 + a_b \left(\frac{M_2}{M_b}\right) [1 - \sin^2 i_b \cos^2 \Omega]^{1/2} \ . \tag{6.20}$$

If this condition is met and if the ratio of the planetary and binary orbital periods is irrational, a transit is guaranteed to occur at some time. For irrational period ratios and random inclinations, the transit probability for star 1 is

$$P_t = \frac{R_1}{a_p} + \frac{a_b}{a_p} \left(\frac{M_2}{M_b}\right) [1 - \sin^2 i_b \cos^2 \Omega]^{1/2} \ . \tag{6.21}$$

The planet may occult one or both stars on some orbits and not during others. However, the overall probability that a transit is *ever* seen is increased, particularly for planet orbits perpendicular to the binary orbit.

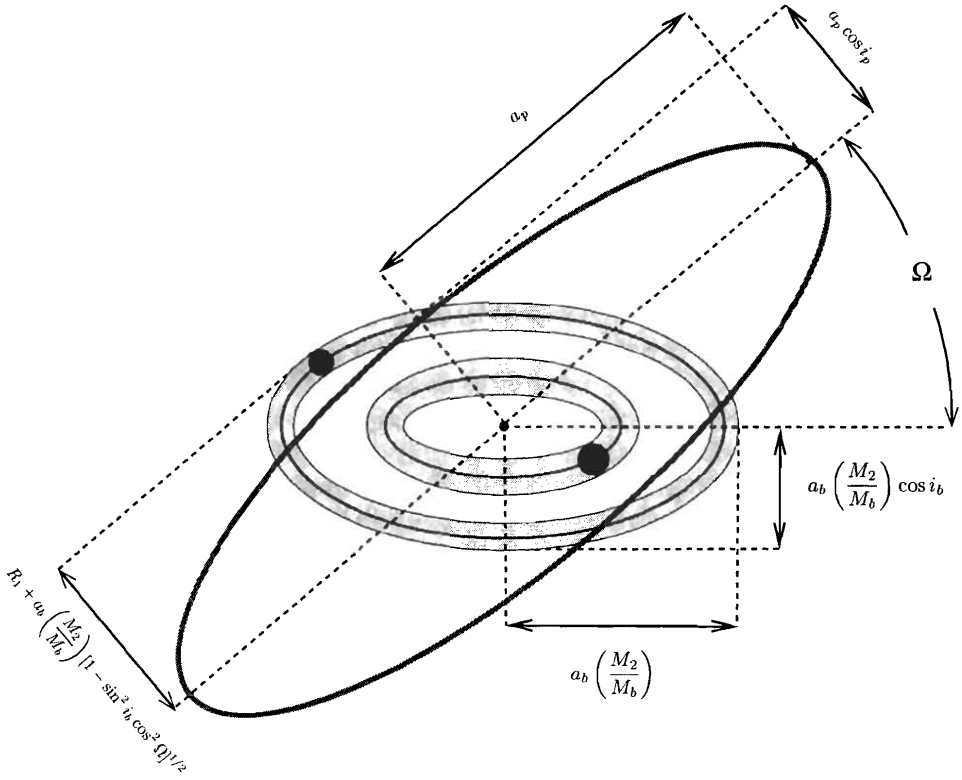

Figure 6-5: Illustration of the circumbinary planetary transit geometry. Angles i_b and i_b are, respectively, the inclinations of the binary and planetary orbits relative to the plane of the sky, and Ω is the angle between the projected major axes of the orbits.

Whether and at what time a transit occurs depends on the phase of the binary orbit, causing the photometric signal to be only quasi-periodic and potentially inter-

mittent; see Figures 6-6, 6-7, and 6-8. The circumstance in which the binary and planet orbits are coaligned (same inclinations and longitudes of the ascending nodes) simplifies planet detection because transits occur during every orbit of the planet (note that this is not assured for eclipsing binaries with transiting planets, for which only the inclinations are equal).

While the signal of a circumbinary planet transiting its host stars is detectable with current photometric surveys, it is concluded that doing so is impractical unless there is a tendency in nature for binary and planet orbits to be coaligned (a tendency which very well may exist). The overall lower alignment probabilities and non-persistent signals that occur in non-coplanar systems prevent transit surveys from being a reliable method in generalized cases

The strategy used to search for transiting circumbinary planets would thus be very different from those of existing transit searches. One would employ a targeted search focused on eclipsing binaries, as these are more likely to have persistent signals (if any signal is detected at all). If coplanarity of orbits is preferred by nature (and if circumbinary planets are as common as those around single stars), one would expect a higher success rate per target system in such a search than in standard transit searches, though the number of systems targeted would clearly be much lower. Such a search would additionally require much more observing time, as one is necessarily looking for relatively long period planets (due to stability criteria). A program to search for planets transiting eclipsing binaries would test the combined hypothesis that circumbinary planets are common and that their orbits are coplanar with that of the binary system; unfortunately, these hypotheses cannot be separated by searches for such transiting planets alone.

6.7 Astrometry

Astrometry measures the relative center of light (CL) positions of two or more targets. The required precisions for astrometric detections of circumbinary planets are similar to those for single stars (to within a factor of two due to increased "stellar" mass). In practice, astrometry of compact binaries is more complicated than that for single stars.

To detect planets, one desires high-precision measurements of the CM position of the bright (stellar) components of a target system—planets cause perturbations to this CM position that cannot be explained by only accounting for the visible system components. Astrometry measures this quantity only indirectly—the CM and CL of a target are not necessarily identical. For single stars, star spots and flares can cause non-constant variations in CL position; noise sources shared for compact binaries. Binaries have the additional complication that orbital motion changes the system CL position relative to its CM. One must solve a combined model of binary and planet orbit, requiring many more observations. The two orbits will be on different timescales, and support observations to determine the relative binary orbit can assist fitting procedures. This affects both single-aperture (e.g. the Palomar STEPS program, [Pravdo and Shaklan, 1996]) and interferometric astrometry.

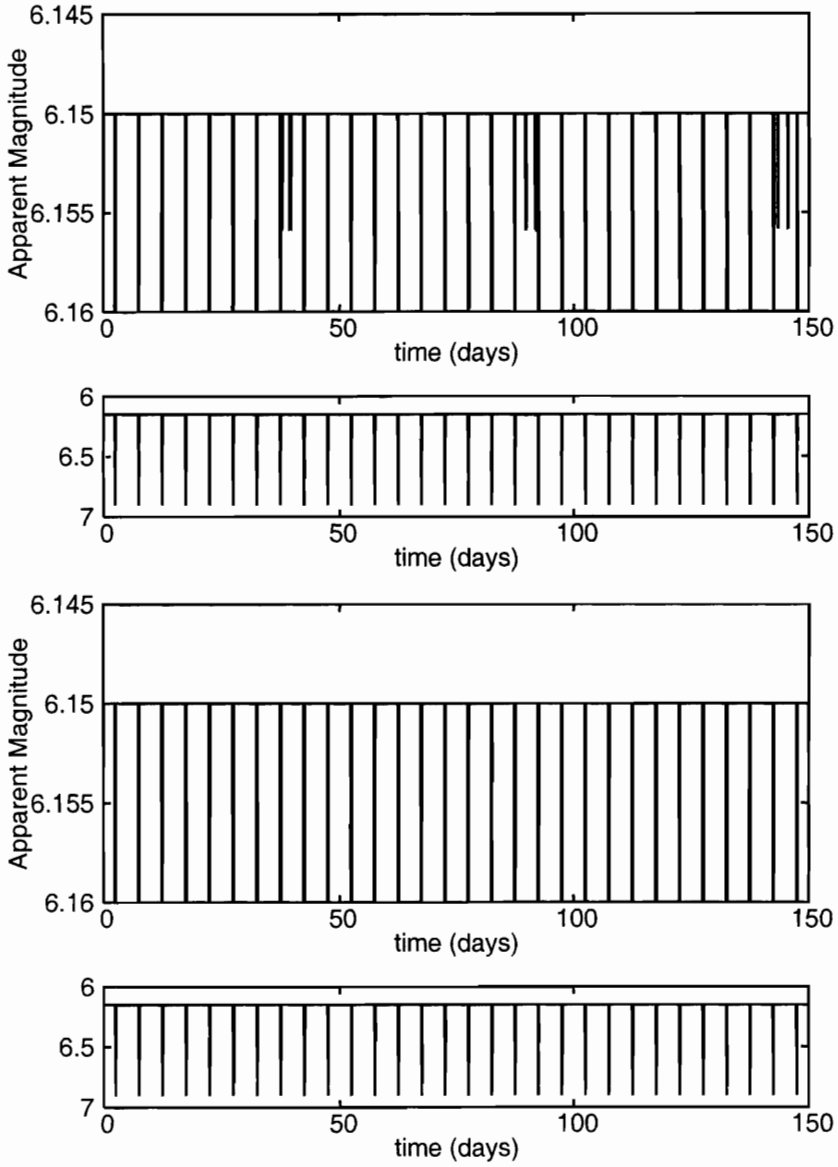

Figure 6-6: Transits in the "prototype" circumbinary planet system with planet and binary inclination both 90 degrees. In the first two graphs, the orbits are coplanar; in the second two they are perpendicular. When the orbits are coplanar, binary eclipses and planet transits are seen every orbit; when perpendicular, the planet manages to pass between both stars on every pass without transiting either, despite its edge-on orbit (in this case, the ratio of binary and planet periods was chosen to be rational; irrational ratios in this geometry are guaranteed to transit at some point).

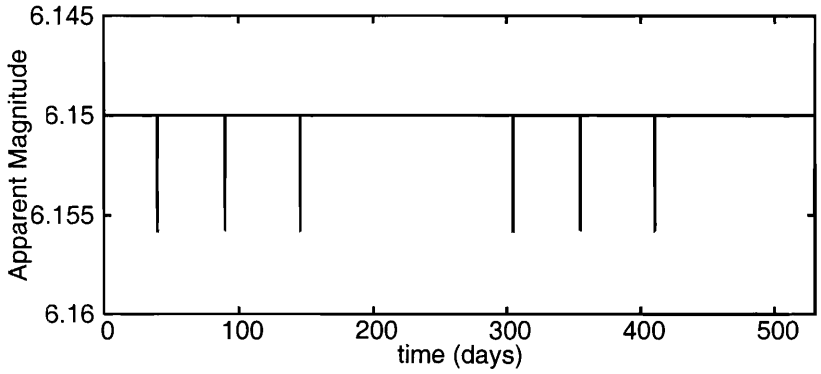

Figure 6-7: Transits in the "prototype" circumbinary planet system with planet inclination 90 degrees and binary inclination 80 degrees (the other two Keplerian angles are the same for planet and binary orbits). The binary itself is not seen to eclipse. Planet transits are sometimes seen, though many times the planet misses both stars; the signal is intermittent.

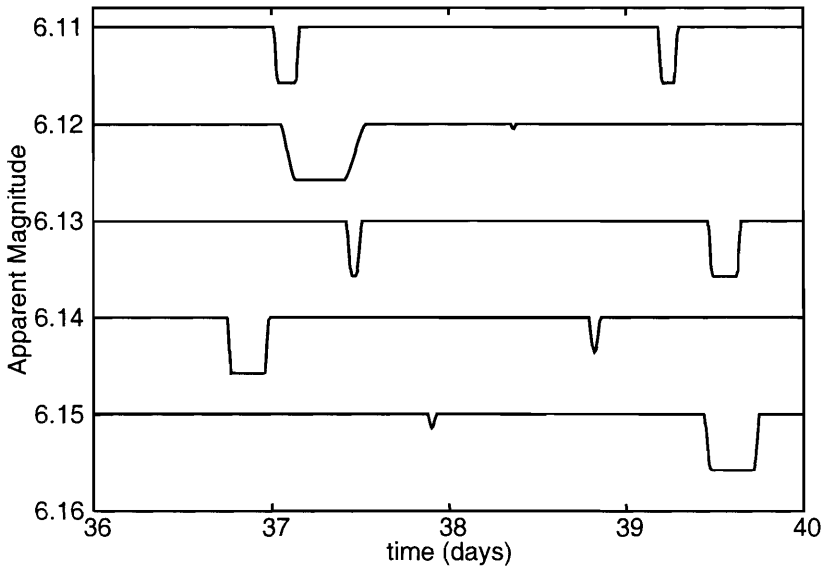

Figure 6-8: Transits in the "prototype" circumbinary planet system with planet inclination 90 degrees and binary inclination 85 degrees (the other two Keplerian angles are the same for planet and binary orbits), modulo the planet's orbital period of 53 days. Consecutive light curves for the planet orbits have been offset by 0.01 magnitudes for clarity. The transits are quasi-periodic—they do not always occur at the same phase of the planet orbit. The exact times at which the transits occur depend on the phase of the binary orbit.

Interferometric astrometry of binary stars has the additional complication that the observable quantity is not necessarily the CL position when the target is only marginally resolved or unresolved. Depending on the design of the interferometer, the measured position for such a source depends on the source brightness distribution and the interferometer resolution. In an interferometer, one can track a source centered either at a position of broadband zero phase or one of zero "group delay"—the position at which all wavelengths of light have an identical phase. In the first case, phase tracking, the phase zero is only equal to the CL position for unresolved sources (the approximation breaks down rapidly as the source separation approaches a fraction of the interferometer resolution). A binary with separation exactly equal to the interferometer resolution would have a phase zero very near the position of just one of the two stars, due to the oscillatory nature of the interferometric fringes. A much better position indicator is the group delay. For a binary target, three positions of zero group delay exist: one near the position of each star and a third between the two. The third group delay zero is an unstable tracking location—servo loops will be driven away from rather than toward this position. The group delay zeros near each star are not perfectly aligned with the star—light (and sidelobe fringes) from the other star biases this position in a way depending on the binary separation, star colors and luminosities, and instrument bandpass. The instrument also will not always remain locked at one group delay zero; jumps from one position to the other are expected, and the fraction of time at either location is related to the combination of star luminosity and size. Some of this confusion might be lifted by also measuring the interferometric visibility of the binary source, and using this information to model the binary itself, which would then be applied to the astrometric data through a complicated model of the instrument.

6.8 Conclusions

For a complete understanding of planetary system diversity and frequency, all possible planetary environments must be included in exoplanet searches. No technique for detecting circumbinary planets is either as simple and as sensitive as its single-star counterpart. However, several possible observational methods are predicted to be capable of achieving the measurement precisions necessary to detect planetary mass companions in circumbinary orbits. Direct imaging of circumbinary planets may be possible with TPF-C if specialized observing sequences are employed. Ground-based eclipse timing and radial velocity observations may be able to detect Jupiter-massed circumbinary planets over the next few years. A search for transiting planets in eclipsing binaries would test the combined hypotheses that circumbinary planets are common and that the orbital planes of the binary and planets are preferentially coaligned.

Bibliography

M. D. Albrow, J.-P. Beaulieu, J. A. R. Caldwell, M. Dominik, B. S. Gaudi, A. Gould, J. Greenhill, K. Hill, S. Kane, R. Martin, J. Menzies, R. M. Naber, K. R. Pollard, P. D. Sackett, K. C. Sahu, P. Vermaak, R. Watson, A. Williams, H. E. Bond, and I. M. van Bemmel. Detection of Rotation in a Binary Microlens: PLANET Photometry of MACHO 97-BLG-41. *ApJ*, 534:894–906, May 2000.

R. Alonso, T. M. Brown, G. Torres, D. W. Latham, A. Sozzetti, G. Mandushev, J. A. Belmonte, D. Charbonneau, H. J. Deeg, E. W. Dunham, F. T. O'Donovan, and R. P. Stefanik. TrES-1: The Transiting Planet of a Bright K0 V Star. *ApJ*, 613: L153–L156, October 2004.

J. H. Applegate. A mechanism for orbital period modulation in close binaries. *ApJ*, 385:621–629, February 1992.

E. Aristidi, M. Carbillet, J.-L. Prieur, B. Lopez, Y. Bresson, and L. Koechlin. ICCD speckle observations of binary stars: Measurements during 1994-1995. *A&AS*, 126: 555–561, December 1997.

J. T. Armstrong, D. Mozurkewich, L. J. Rickard, D. J. Hutter, J. A. Benson, P. F. Bowers, N. M. Elias, C. A. Hummel, K. J. Johnston, D. F. Buscher, J. H. Clark, L. Ha, L.-C. Ling, N. M. White, and R. S. Simon. The Navy Prototype Optical Interferometer. *ApJ*, 496:550–+, March 1998.

W. G. Bagnuolo, T. A. ten Brummelaar, H. A. McAlister, N. H. Turner, L. Sturmann, J. Sturmann, and S. T. Ridgway. Well-resolved binary astrometry with the CHARA array. In *Interferometry for Optical Astronomy II. Edited by Wesley A. Traub . Proceedings of the SPIE, Volume 4838, pp. 1061-1067 (2003).*, pages 1061–1067, February 2003.

P. Baize. Mesures d'étoiles doubles faites à l'Observatoire de Paris. *Journal des Observateurs*, 37:73–+, January 1954.

I. Balega, D. Bonneau, and R. Foy. Speckle interferometric measurements of binary stars. II. *A&AS*, 57:31–36, July 1984.

I. I. Balega and Y. Y. Balega. Digital speckle interferometery of binary stars with the six-meter telescope. *Soviet Astronomy Letters*, 13:208–+, May 1987.

I. I. Balega, Y. Y. Balega, I. N. Belkin, A. F. Maximov, V. G. Orlov, E. A. Pluzhnik, Z. U. Shkhagosheva, and V. A. Vasyuk. Binary star speckle measurements during 1989-1993 from the SAO 6 M and 1 M telescopes in Zelenchuk. *A&AS*, 105:503–506, June 1994.

I. I. Balega, Y. Y. Balega, K.-H. Hofmann, A. F. Maksimov, E. A. Pluzhnik, D. Schertl, Z. U. Shkhagosheva, and G. Weigelt. Speckle interferometry of nearby multiple stars. *A&A*, 385:87–93, April 2002.

I. I. Balega, Y. Y. Balega, A. F. Maksimov, E. A. Pluzhnik, Z. U. Shkhagosheva, and V. A. Vasyuk. Binary star speckle measurements during 1992-1997 from the SAO 6-m and 1-m telescopes in Zelenchuk. *A&AS*, 140:287–292, December 1999.

I. I. Balega, Y. Y. Balega, and V. A. Vasyuk. Speckle Interferometry Measurements of Binaries Using the 6-METER Telescope in 1986. *BULL. SPECIAL ASTROF.OBS. NORTH CAUCASUS V. 28, P. 102, 1989*, 28:102–+, 1989.

Y. Y. Balega and I. I. Balega. Digital Speckle Interferometry of 72 Binary Stars. *Soviet Astronomy Letters*, 11:47–+, February 1985.

M. Barbieri, F. Marzari, and H. Scholl. Formation of terrestrial planets in close binary systems: The case of alpha Centauri A. *A&A*, 396:219–224, December 2002.

D. J. Barlow and C. D. Scarfe. Kap Peg, a triple system. *PASP*, 89:857–861, December 1977.

G. Basri. Observations of Brown Dwarfs. *ARA&A*, 38:485–519, 2000.

W. R. Beardsley and M. W. King. Interpretation of a spectrographic observations of the resolved components of kap Peg. *PASP*, 88:200–203, April 1976.

C. A. Beichman. Terrestrial Planet Finder: the search for life-bearing planets around other stars. In *Proc. SPIE Vol. 3350, p. 719-723, Astronomical Interferometry, Robert D. Reasenberg; Ed.*, pages 719–723, July 1998.

G. F. Benedict, B. E. McArthur, T. Forveille, X. Delfosse, E. Nelan, R. P. Butler, W. Spiesman, G. Marcy, B. Goldman, C. Perrier, W. H. Jefferys, and M. Mayor. A Mass for the Extrasolar Planet Gliese 876b Determined from Hubble Space Telescope Fine Guidance Sensor 3 Astrometry and High-Precision Radial Velocities. *ApJ*, 581:L115–L118, December 2002.

D. Benest. Planetary orbits in the elliptic restricted problem. I - The Alpha Centauri system. *A&A*, 206:143–146, November 1988.

D. Benest. Planetary orbits in the elliptic restricted problem. II - The Sirius system. *A&A*, 223:361–364, October 1989.

D. Benest. Stable planetary orbits around one component in nearby binary stars. II. *Celestial Mechanics and Dynamical Astronomy*, 56:45–50, June 1993.

D. Benest. Planetary orbits in the elliptic restricted problem. III. The η Coronae Borealis system. *A&A*, 314:983–988, October 1996.

D. Benest. Planetary orbits in the elliptic restricted problem. V.. The ADS 11060 system. *A&A*, 400:1103–1111, March 2003.

D. P. Bennett, S. H. Rhie, A. C. Becker, N. Butler, J. Dann, S. Kaspi, E. M. Leibowitz, Y. Lipkin, D. Maoz, H. Mendelson, B. A. Peterson, J. Quinn, O. Shemmer, S. Thomson, and S. E. Turner. Discovery of a planet orbiting a binary star system from gravitational microlensing. *Nature*, 402:57–59, November 1999.

D. C. Black. A simple criterion for determining the dynamical stability of three-body systems. *AJ*, 87:1333–1337, September 1982.

C. Boehm. The mass and luminosity of cool dwarf stars. *Ap&SS*, 155:241–248, May 1989.

D. Bonneau, A. Blazit, R. Foy, and A. Labeyrie. Speckle interferometric measurements of binary stars. *A&AS*, 42:185–188, November 1980.

D. Bonneau, J. M. Carquillat, and J. L. Vidal. Observations of binary stars by speckle interferometry at the PIC DU Midi T2m. *A&AS*, 58:729–733, December 1984.

A. P. Boss. Extrasolar Planets and Brown Dwarf Stars. *Bulletin of the American Astronomical Society*, 30:1048–+, September 1998.

R. A. Broucke. Stable Orbits of Planets of a Binary Star System in the Three-Dimensional Restricted Problem. *Celestial Mechanics and Dynamical Astronomy*, 81:321–341, December 2001.

S. W. Burnham. the discovery of κ Pegasi as a close double star. *MNRAS*, 41:33–+, November 1880.

W. W. Campbell and W. H. Wright. A list of nine stars whose velocities in the line of sight are variable. *ApJ*, 12:254–257, November 1900.

B. W. Carroll and D. A. Ostlie. *An introduction to modern astrophysics.* Reading, MA: Addison-Wesley, —c1996, 1996.

F. Castelli, R. G. Gratton, and R. L. Kurucz. Notes on the convection in the ATLAS9 model atmospheres. *A&A*, 318:841–869, February 1997.

CHARA. Unpublished CHARA KPNO 2.1-m data. 1984.

D. Charbonneau, T. M. Brown, D. W. Latham, and M. Mayor. Detection of Planetary Transits Across a Sun-like Star. *ApJ*, 529:L45–L48, January 2000.

G. Chauvin, A.-M. Lagrange, C. Dumas, B. Zuckerman, D. Mouillet, I. Song, J.-L. Beuzit, and P. Lowrance. A giant planet candidate near a young brown dwarf. Direct VLT/NACO observations using IR wavefront sensing. *A&A*, 425:L29–L32, October 2004.

M. M. Colavita. Measurement of the Atmospheric Limit to Narrow Angle Interferometric Astrometry Using the Mark-III Stellar Interferometer. *A&A*, 283:1027–+, March 1994.

M. M. Colavita. Beam walk calculations. Private communication, 1998.

M. M. Colavita and M. Shao. Indirect planet detection with ground-based long-baseline interferometry. *Ap&SS*, 212:385–390, February 1994.

M. M. Colavita, J. K. Wallace, B. E. Hines, Y. Gursel, F. Malbet, D. L. Palmer, X. P. Pan, M. Shao, J. W. Yu, A. F. Boden, P. J. Dumont, J. Gubler, C. D. Koresko, S. R. Kulkarni, B. F. Lane, D. W. Mobley, and G. T. van Belle. The Palomar Testbed Interferometer. *ApJ*, 510:505–521, January 1999.

A. C. M. Correia, S. Udry, M. Mayor, J. Laskar, D. Naef, F. Pepe, D. Queloz, and N. C. Santos. A pair of planets around HD 202206 or a circumbinary planet? *Submitted to A&A*, 2004. http://arxiv.org/abs/astro-ph/0411512.

P. Couteau. Mesures d'étoiles doubles faites aux Observatoires Yerkes et McDonald. *Journal des Observateurs*, 45:225–+, 1962.

P. Couteau. Mesures d'étoiles doubles faites au réfracteur de 38 cm de l'Observatoire de Nice. *Journal des Observateurs*, 46:155–+, 1963.

P. Couteau. Mesures d'étoiles doubles faites au réfracteur de 38 cm de l'Observatoire de Nice. *Journal des Observateurs*, 49:341–+, 1966.

P. Couteau. Mesures d'etoiles doubles faites a Nice a la lunette de 50 cm. *Journal des Observateurs*, 51:337–+, 1968.

P. Couteau. Mesures d'étoiles doubles faites à Nice aux lunettes de 50 et de 74 CM. *A&AS*, 3:51–+, November 1970.

P. Couteau. Mesures d'étoiles doubles faites à Nice. *A&AS*, 6:185–+, June 1972.

P. Couteau. Measurements of double stars made at Nice. *A&AS*, 20:391–+, June 1975.

P. Couteau. Measurements of double stars at Nice with 74-cm and 50-cm refractors. *A&AS*, 60:241–259, May 1985.

P. Couteau. Measurements of binary stars obtained at Pic-du-Midi and at Nice. *A&AS*, 79:385–389, September 1989.

A. N. Cox. *Allen's astrophysical quantities.* Allen's astrophysical quantities, 4th ed. Publisher: New York: AIP Press; Springer, 2000. Editedy by Arthur N. Cox. ISBN: 0387987460, 2000.

A. Danjon. Observations d'Etoiles Doubles avec un micromètre interférentiel à demi-onde. *Journal des Observateurs*, 35:85–+, January 1952.

H. J. Deeg, L. R. Doyle, V. P. Kozhevnikov, J. E. Blue, E. L. Martín, and J. Schneider. A search for Jovian-mass planets around CM Draconis using eclipse minima timing. *A&A*, 358:L5–L8, June 2000.

R. C. Dempsey, J. L. Linsky, T. A. Fleming, and J. H. M. M. Schmitt. The ROSAT All-Sky Survey of active binary coronae. I - Quiescent fluxes for the RS Canum Venaticorum systems. *ApJS*, 86:599–609, June 1993.

J. A. Docobo. Micrometer measurements of double stars from the Spanish observatories at Calar Alto and Santiago de Compostela. *A&AS*, 130:117–+, May 1998.

L. R. Doyle, H. Deeg, J. M. Jenkins, J. Schneider, Z. Ninkov, R. Stone, H. Gotzger, B. Friedman, J. E. Blue, and M. F. Doyle. Detectability of Jupiter-to-Brown-Dwarf-Mass Companions Around Small Eclipsing Binary Systems. In *ASP Conf. Ser. 134: Brown Dwarfs and Extrasolar Planets*, pages 224–+, 1998.

S. A. Drake, T. Simon, and J. L. Linsky. A survey of the radio continuum emission of RS Canum Venaticorum and related active binary systems. *ApJS*, 71:905–930, December 1989.

A. Duquennoy and M. Mayor. Duplicity in the solar neighbourhood. III - New spectroscopic elements for nine solar-type binary stars. *A&A*, 195:129–147, April 1988.

A. Duquennoy and M. Mayor. Multiplicity among solar-type stars in the solar neighbourhood. II - Distribution of the orbital elements in an unbiased sample. *A&A*, 248:485–524, August 1991.

M. M. Dworetsky, D. M. Popper, and D. S. Dearborn. The Mass and Absolute Magnitude of the Visual Binary Delta Equulei from Radial Velocity Observations. *PASP*, 83:207–+, April 1971.

H. M. Dyck, J. A. Benson, and F. P. Schloerb. Imaging a Binary Star With a Two-Telescope Michelson Stellar Interferometer. *AJ*, 110:1433–+, September 1995.

O. J. Eggen. Kinematics and Metallicity of Stars in the Solar Region. *AJ*, 115: 2397–2434, June 1998.

J. A. Eisner and S. R. Kulkarni. Sensitivity of the Astrometric Technique in Detecting Outer Planets. *ApJ*, 561:1107–1115, November 2001.

W. S. Finsen. *Union Obs. Circ.*, 6:94, 1951.

W. S. Finsen. *Union Obs. Circ.*, 6:170, 1953.

W. S. Finsen. *Union Obs. Circ.*, 6:240, 1954.

W. S. Finsen. *Union Obs. Circ.*, 6:259, 1956.

W. S. Finsen. *Union Obs. Circ.*, 6:333, 1960.

W. S. Finsen. *Republic Obs. Circ.*, 7:10, 1963.

W. S. Finsen. *Republic Obs. Circ.*, 7:32, 1964.

W. S. Finsen. *Republic Obs. Circ.*, 7:79, 1966.

H. Frieboes-Conde and T. Herczeg. Period variations of fourteen eclipsing binaries with possible light-time effect. *A&AS*, 12:1–+, October 1973.

H. Fu, W. I. Hartkopf, B. D. Mason, H. A. McAlister, E. G. Dombrowski, T. Westin, and O. G. Franz. ICCD Speckle Observations of Binary Stars. XVI. Measurements During 1982-1989 from the Perkins 1.8-M Telescope. *AJ*, 114:1623–+, October 1997.

G. Gatewood. One milliarcsecond precision studies in the regions of δ Equulei and χ^1 Orionis. *PASP*, 106:138–144, February 1994.

M. E. Germain, G. G. Douglass, and C. E. Worley. Speckle Interferometry at the US Naval Observatory. II. *AJ*, 117:1905–1920, April 1999a.

M. E. Germain, G. G. Douglass, and C. E. Worley. Speckle Interferometry at the US Naval Observatory. III. *AJ*, 117:2511–2527, May 1999b.

R. Gili and D. Bonneau. CCD measurements of visual double stars made with the 74 cm and 50 cm refractors of the Nice Observatory (2nd series). *A&A*, 378:954–957, November 2001.

R. L. Gilliland, T. M. Brown, P. Guhathakurta, A. Sarajedini, E. F. Milone, M. D. Albrow, N. R. Baliber, H. Bruntt, A. Burrows, D. Charbonneau, P. Choi, W. D. Cochran, P. D. Edmonds, S. Frandsen, J. H. Howell, D. N. C. Lin, G. W. Marcy, M. Mayor, D. Naef, S. Sigurdsson, C. R. Stagg, D. A. Vandenberg, S. S. Vogt, and M. D. Williams. A Lack of Planets in 47 Tucanae from a Hubble Space Telescope Search. *ApJ*, 545:L47–L51, December 2000.

L. Girardi, A. Bressan, G. Bertelli, and C. Chiosi. Evolutionary tracks and isochrones for low- and intermediate-mass stars: From 0.15 to 7 $M_{\odot}$, and from Z=0.0004 to 0.03. *A&AS*, 141:371–383, February 2000.

R. O. Gray, C. J. Corbally, R. F. Garrison, M. T. McFadden, and P. E. Robinson. Contributions to the Nearby Stars (NStars) Project: Spectroscopy of Stars Earlier than M0 within 40 Parsecs: The Northern Sample. I. *AJ*, 126:2048–2059, October 2003.

F. Graziani and D. C. Black. Orbital stability constraints on the nature of planetary systems. *ApJ*, 251:337–341, December 1981.

G. M. H. J. Habets and J. R. W. Heintze. Empirical bolometric corrections for the main-sequence. *A&AS*, 46:193–237, November 1981.

A. Hale. Orbital coplanarity in solar-type binary systems: Implications for planetary system formation and detection. *AJ*, 107:306–332, January 1994.

E. M. Hans, C. D. Scarfe, J. M. Fletcher, and C. L. Morbey. The orbit of Delta Equulei in three dimensions. *ApJ*, 229:1001–1007, May 1979.

W. I. Hartkopf, B. D. Mason, D. J. Barry, H. A. McAlister, W. G. Bagnuolo, and C. M. Prieto. ICCD speckle observations of binary stars. VIII - Measurements during 1989-1991 from the Cerro Tololo 4 M telescope. *AJ*, 106:352–360, July 1993.

W. I. Hartkopf, B. D. Mason, and H. A. McAlister. Binary Star Orbits From Speckle Interferometry. VIII. Orbits of 37 Close Visual System. *AJ*, 111:370–+, January 1996.

W. I. Hartkopf, B. D. Mason, H. A. McAlister, L. C. Roberts, N. H. Turner, T. A. ten Brummelaar, C. M. Prieto, J. F. Ling, and O. G. Franz. ICCD Speckle Observations of Binary Stars. XXIII. Measurements during 1982-1997 from Six Telescopes, with 14 New Orbits. *AJ*, 119:3084–3111, June 2000.

W. I. Hartkopf, B. D. Mason, G. L. Wycoff, and H. A. McAlister. Fourth catalog of interferometric measurements of binary stars. *http://ad.usno.navy.mil/wds/int4.html*, 2004.

W. I. Hartkopf, H. A. McAlister, and O. G. Franz. Binary star orbits from speckle interferometry. II - Combined visual-speckle orbits of 28 close systems. *AJ*, 98: 1014–1039, September 1989.

W. I. Hartkopf, H. A. McAlister, and O. G. Franz. ICCD speckle observations of binary stars. VI - Measurements during 1989-1990 from the Kitt Peak 4 M telescope. *AJ*, 104:810–820, August 1992.

W. I. Hartkopf, H. A. McAlister, B. D. Mason, D. J. Barry, N. H. Turner, and H. Fu. ICCD speckle observations of binary stars. 11: Measurements during 1991-1993 from the Kitt Peak 4 M telescope. *AJ*, 108:2299–2311, December 1994.

W. I. Hartkopf, H. A. McAlister, B. D. Mason, T. T. Brummelaar, L. C. Roberts, N. H. Turner, and J. W. Wilson. ICCD Speckle Observations of Binary Stars. XVII. Measurements During 1993-1995 From the Mount Wilson 2.5-M Telescope. *AJ*, 114:1639–+, October 1997.

W. D. Heacox. Statistical dynamics of solar-like binaries. *AJ*, 115:325–+, January 1998.

W. D. Heintz. Mikrometermessungen von Doppelsternen. VI. *Journal des Observateurs*, 50:343–+, 1967.

W. D. Heintz. A Study of Multiple-Star Systems. *AJ*, 111:408–+, January 1996.

F. Henroteau. Buletin Number 304 - A prectrographic study of kappa Pegasi. *Lick Observatory Bulletin*, 9:120–127, 1918.

F. Holden. Measures of double stars. *Journal des Observateurs*, 46:133–+, 1963.

F. Holden. Double Star Measures at Lick Observatory, Mount Hamilton, California. *PASP*, 86:902–+, December 1974.

F. Holden. Micrometric measures of visual double stars. *PASP*, 87:253–257, April 1975.

F. Holden. Double star measures at Lick Observatory Mount Hamilton California. *PASP*, 88:325–333, June 1976.

F. Holden. Double star measures at Lick Observatory, Mount Hamilton, California. *PASP*, 90:465–472, August 1978.

F. Holden. Visual double stars measured at Lick Observatory Mount Hamilton, California. *PASP*, 91:479–486, August 1979.

M. J. Holman and P. A. Wiegert. Long-Term Stability of Planets in Binary Systems. *AJ*, 117:621–628, January 1999.

E. Horch, Z. Ninkov, W. F. van Altena, R. D. Meyer, T. M. Girard, and J. G. Timothy. Speckle Observations of Binary Stars with the WIYN Telescope. I. Measures During 1997. *AJ*, 117:548–561, January 1999.

E. Horch, W. F. van Altena, T. M. Girard, O. G. Franz, C. E. López, and J. G. Timothy. Speckle Interferometry of Southern Double Stars. II. Measures from the CASLEO 2.15 Meter Telescope, 1995-1996. *AJ*, 121:1597–1606, March 2001.

E. P. Horch, S. E. Robinson, R. D. Meyer, W. F. van Altena, Z. Ninkov, and A. Piterman. Speckle Observations of Binary Stars with the WIYN Telescope. II. Relative Astrometry Measures during 1998-2000. *AJ*, 123:3442–3459, June 2002.

C. A. Hummel, J. A. Benson, D. J. Hutter, K. J. Johnston, D. Mozurkewich, J. T. Armstrong, R. B. Hindsley, G. C. Gilbreath, L. J. Rickard, and N. M. White. First Observations with a Co-phased Six-Station Optical Long-Baseline Array: Application to the Triple Star η Virginis. *AJ*, 125:2630–2644, May 2003.

C. A. Hummell, D. Mozurkewich, N. M. Elias, A. Quirrenbach, D. F. Buscher, J. T. Armstrong, K. J. Johnston, R. S. Simon, and D. J. Hutter. Four years of astrometric measurements with the Mark 3 optical interferometer. *AJ*, 108:326–336, July 1994.

K. A. Innanen, J. Q. Zheng, S. Mikkola, and M. J. Valtonen. The Kozai Mechanism and the Stability of Planetary Orbits in Binary Star Systems. *AJ*, 113:1915–+, May 1997.

J. B. Irwin. The Determination of a Light-Time Orbit. *ApJ*, 116:211–+, July 1952.

R. M. Ismailov. Interferometric observations of double stars in 1986-1990. *A&AS*, 96: 375–377, December 1992.

S. Isobe, M. Noguchi, J. Ohtsubo, N. Baba, N. Miura, T. Tanaka, and M. Ni-Ino. Speckle observations of visual and spectroscopic binaries. III. *Publications of the National Astronomical Observatory of Japan*, 2:459–474, 1992.

S. Isobe, Y. Norimoto, M. Noguchi, J. Ohtsubo, and N. Baba. Speckle observations of visual and spectroscopic binaries. II. *Publications of the National Astronomical Observatory of Japan*, 1:381–392, 1990.

H. M. Jeffers. a.

H. M. Jeffers. Bulletin Number 518 - Measures of double stars. *Lick Observatory Bulletin*, 19:175–181, b.

G. H. Kaplan, J. A. Hughes, P. K. Seidelmann, C. A. Smith, and B. D. Yallop. Mean and apparent place computations in the new IAU system. III - Apparent, topocentric, and astrometric places of planets and stars. *AJ*, 97:1197–1210, April 1989.

L. G. Kiseleva, P. P. Eggleton, and S. Mikkola. Tidal friction in triple stars. *MNRAS*, 300:292–302, October 1998.

M. Konacki. Precision radial velocities of double-lined spectroscopic binaries with an iodine absorption cell. *Submitted to ApJ*, 2004.

Y. Kozai. Secular perturbations of asteroids with high inclination and eccentricity. *AJ*, 67:591–+, November 1962.

B. F. Lane and M. M. Colavita. Phase-referenced Stellar Interferometry at the Palomar Testbed Interferometer. *AJ*, 125:1623–1628, March 2003.

B. F. Lane, M. M. Colavita, A. F. Boden, and P. R. Lawson. Palomar Testbed Interferometer: update. In *Proc. SPIE Vol. 4006, p. 452-458, Interferometry in Optical Astronomy, Pierre J. Lena; Andreas Quirrenbach; Eds.*, pages 452–458, July 2000.

B. F. Lane and M. W. Muterspaugh. Differential Astrometry of Subarcsecond Scale Binaries at the Palomar Testbed Interferometer. *ApJ*, 601:1129–1135, February 2004.

J. Laskar, F. Joutel, and P. Robutel. Stabilization of the earth's obliquity by the moon. *Nature*, 361:615–617, February 1993.

E. Lastennet, J. Fernandes, and T. Lejeune. A revised HRD for individual components of binary systems from BaSeL BVRI synthetic photometry. Influence of interstellar extinction and stellar rotation. *A&A*, 388:309–319, June 2002.

G. Laughlin and J. E. Chambers. Extrasolar Trojans: The Viability and Detectability of Planets in the 1:1 Resonance. *AJ*, 124:592–600, July 2002.

P. R. Lawson, editor. *Principles of Long Baseline Stellar Interferometry*, 2000.

J. Le Beau. Binary star measurements made at Nice with the 50-cm reflector. *A&AS*, 77:125–130, January 1989.

J. Lestrade, R. B. Phillips, M. W. Hodges, and R. A. Preston. VLBI astrometric identification of the radio emitting region in Algol and determination of the orientation of the close binary. *ApJ*, 410:808–814, June 1993.

L. Lindegren. Atmospheric limitations of narrow-field optical astrometry. *A&A*, 89: 41–47, September 1980.

J. F. Ling and C. Prieto. Micrometer measurements of visual double stars made at the Cote d'Azur Observatory. *Astronomische Nachrichten*, 318:365–367, November 1997.

S. H. Lubow and P. Artymowicz. Interactions of Young Binaries with Disks. *Protostars and Planets IV*, pages 731–+, May 2000.

W. J. Luyten. New Orbits for Four Binary Stars. *PASP*, 46:199–+, August 1934a.

W. J. Luyten. The Triple System of κ Pegasi. *ApJ*, 79:449–+, June 1934b.

G. W. Marcy and R. P. Butler. Detection of Extrasolar Giant Planets. *ARA&A*, 36: 57–98, 1998.

C. Martin, F. Mignard, W. I. Hartkopf, and H. A. McAlister. Mass determination of astrometric binaries with Hipparcos. III. New results for 28 systems. *A&AS*, 133: 149–162, December 1998.

F. Marzari and H. Scholl. Planetesimal Accretion in Binary Star Systems. *ApJ*, 543: 328–339, November 2000.

B. D. Mason, W. I. Hartkopf, E. R. Holdenried, and T. J. Rafferty. Speckle Interferometry of New and Problem Hipparcos Binaries. II. Observations Obtained in 1998-1999 from McDonald Observatory. *AJ*, 121:3224–3234, June 2001.

B. D. Mason, C. Martin, W. I. Hartkopf, D. J. Barry, M. E. Germain, G. G. Douglass, C. E. Worley, G. L. Wycoff, T. Ten Brummelaar, and O. G. Franz. Speckle Interferometry of New and Problem HIPPARCOS Binaries. *AJ*, 117:1890–1904, April 1999.

R. D. Mathieu, A. M. Ghez, E. L. N. Jensen, and M. Simon. Young Binary Stars and Associated Disks. *Protostars and Planets IV*, pages 703–+, May 2000.

L. Mayer, T. R. Quinn, J. Wadsley, and J. Stadel. SPH Simulations Of Giant Planet Formation From Disk Instability. *AAS/Division of Dynamical Astronomy Meeting*, 35:–+, May 2004.

M. Mayor and T. Mazeh. The frequency of triple and multiple stellar systems. *A&A*, 171:157–177, January 1987.

M. Mayor and D. Queloz. A Jupiter-Mass Companion to a Solar-Type Star. *Nature*, 378:355–+, November 1995.

T. Mazeh, D. Goldberg, A. Duquennoy, and M. Mayor. On the mass-ratio distribution of spectroscopic binaries with solar-type primaries. *ApJ*, 401:265–268, December 1992.

H. McAlister, W. I. Hartkopf, and O. G. Franz. ICCD speckle observations of binary stars. V - Measurements during 1988-1989 from the Kitt Peak and the Cerro Tololo 4 M telescopes. *AJ*, 99:965–978, March 1990.

H. A. McAlister. Speckle interferometric measurements of binary stars. I. *ApJ*, 215: 159–165, July 1977.

H. A. McAlister. Speckle interferometric measurements of binary stars. II. *ApJ*, 225: 932–938, November 1978.

H. A. McAlister. Speckle interferometric measurements of binary stars. IV. *ApJ*, 230: 497–501, June 1979.

H. A. McAlister and F. C. Fekel. Speckle interferometric measurements of binary stars. V. *ApJS*, 43:327–337, June 1980.

H. A. McAlister, W. I. Hartkopf, B. J. Gaston, E. M. Hendry, and F. C. Fekel. Speckle interferometric measurements of binary stars. IX. *ApJS*, 54:251–257, February 1984.

H. A. McAlister, W. I. Hartkopf, E. M. Hendry, B. G. Campbell, and F. C. Fekel. Speckle interferometric measurements of binary stars. VIII. *ApJS*, 51:309–320, March 1983.

H. A. McAlister, W. I. Hartkopf, D. J. Hutter, and O. G. Franz. ICCD speckle observations of binary stars. II - Measurements during 1982-1985 from the Kitt Peak 4 M telescope. *AJ*, 93:688–723, March 1987a.

H. A. McAlister, W. I. Hartkopf, D. J. Hutter, M. M. Shara, and O. G. Franz. ICCD speckle observations of binary stars. I - A survey for duplicity among the bright stars. *AJ*, 93:183–194, January 1987b.

H. A. McAlister, W. I. Hartkopf, J. R. Sowell, E. G. Dombrowski, and O. G. Franz. ICCD speckle observations of binary stars. IV - Measurements during 1986-1988 from the Kitt Peak 4 M telescope. *AJ*, 97:510–531, February 1989.

H. A. McAlister and E. M. Hendry. Speckle interferometric measurements of binary stars. VI. *ApJS*, 48:273–278, March 1982a.

H. A. McAlister and E. M. Hendry. Speckle interferometric measurements of binary stars. VII. *ApJS*, 49:267–272, June 1982b.

C. McCabe, G. Duchêne, and A. M. Ghez. The First Detection of Spatially Resolved Mid-Infrared Scattered Light from a Protoplanetary Disk. *ApJ*, 588:L113–L116, May 2003.

N. Miura, N. Baba, M. Ni-Ino, J. Ohtsubo, M. Noguchi, and S. Isobe. Speckle observations of visual and spectroscopic binaries. IV. *Publications of the National Astronomical Observatory of Japan*, 2:561–571, 1992.

N. Miura, M. Ni-Ino, N. Baba, T. Iribe, and S. Isobe. Speckle observations of visual and spectroscopic binaries. V. *Publications of the National Astronomical Observatory of Japan*, 3:153–167, 1993.

P. J. Morel. Mesures d'étoiles doubles visuelles. *A&AS*, 3:71–+, November 1970.

B. L. Morgan, G. K. Beckmann, and R. J. Scaddan. Observations of binary stars by speckle interferometry. II. *MNRAS*, 192:143–151, July 1980.

B. L. Morgan, D. R. Beddoes, R. J. Scaddan, and J. C. Dainty. Observations of binary stars by speckle interferometry. I. *MNRAS*, 183:701–710, June 1978.

P. Muller. Mesures d'Etoiles Doubles faites à Strasbourg en 1948-50. *Journal des Observateurs*, 33:105–+, January 1950.

P. Muller. Double star observations at Lick Observatory. *AJ*, 59:388–+, November 1954a.

P. Muller. Mesures d'étoiles doubles faites à Strasbourg en 1952-1953. *Journal des Observateurs*, 37:125–+, January 1954b.

P. Muller. Mesures d'étoiles doubles faites à Strasbourg en 1954. *Journal des Observateurs*, 38:221–+, January 1955.

P. Muller. Observations d'étoiles doubles faites au Pic-du-Midi en spetembre octobre 1957. *Journal des Observateurs*, 41:109–+, January 1958.

P. Muller. Mesures d'étoiles doubles à Meudon. *Journal des Observateurs*, 49:335–+, 1966.

P. Muller. Mesures d'etoiles doubles a Meudon (3eme et derniere serie). *A&AS*, 23: 205–221, January 1976.

M. W. Muterspaugh, B. F. Lane, M. Konacki, B. F. Burke, M. M. Colavita, S. R. Kulkarni, and M. Shao. Phases differential astrometry and the mutual inclination of the v819 herculis triple star system. Submitted for publication., 2005a.

M. W. Muterspaugh, B. F. Lane, M. Konacki, S. Wiktorowicz, B. F. Burke, M. M. Colavita, S. R. Kulkarni, and M. Shao. Phases differential astrometry and iodine cell radial velocities of the κ pegasi triple star system. Submitted for publication., 2005b.

T. Nakajima, B. R. Oppenheimer, S. R. Kulkarni, D. A. Golimowski, K. Matthews, and S. T. Durrance. Discovery of a Cool Brown Dwarf. *Nature*, 378:463–+, November 1995.

A. F. Nelson. Planet Formation is Unlikely in Equal-Mass Binary Systems with A ˜ 50 AU. *ApJ*, 537:L65–L68, July 2000.

B. Nordström, M. Mayor, J. Andersen, J. Holmberg, F. Pont, B. R. Jørgensen, E. H. Olsen, S. Udry, and N. Mowlavi. The Geneva-Copenhagen survey of the Solar neighbourhood. Ages, metallicities, and kinematic properties of ∼14000 F and G dwarfs. *A&A*, 418:989–1019, May 2004.

X. Pan, M. Shao, and M. M. Colavita. High angular resolution measurements of Algol. *ApJ*, 413:L129–L131, August 1993.

J. Patience, R. J. White, A. M. Ghez, C. McCabe, I. S. McLean, J. E. Larkin, L. Prato, S. S. Kim, J. P. Lloyd, M. C. Liu, J. R. Graham, B. A. Macintosh, D. T. Gavel, C. E. Max, B. J. Bauman, S. S. Olivier, P. Wizinowich, and D. S. Acton. Stellar Companions to Stars with Planets. *ApJ*, 581:654–665, December 2002.

Y. J. Pendleton and D. C. Black. Further studies on criteria for the onset of dynamical instability in general three-body systems. *AJ*, 88:1415–1419, September 1983.

M. A. C. Perryman. Extra-solar planets. *Reports of Progress in Physics*, 63:1209–1272, 2000.

M. A. C. Perryman, L. Lindegren, J. Kovalevsky, E. Hoeg, U. Bastian, P. L. Bernacca, M. Crézé, F. Donati, M. Grenon, F. van Leeuwen, H. van der Marel, F. Mignard, C. A. Murray, R. S. Le Poole, H. Schrijver, C. Turon, F. Arenou, M. Froeschlé, and C. S. Petersen. The HIPPARCOS Catalogue. *A&A*, 323:L49–L52, July 1997.

E. Pilat-Lohinger and R. Dvorak. Stability of S-type Orbits in Binaries. *Celestial Mechanics and Dynamical Astronomy*, 82:143–153, 2002.

E. Pilat-Lohinger, B. Funk, and R. Dvorak. Stability limits in double stars. A study of inclined planetary orbits. *A&A*, 400:1085–1094, March 2003.

D. M. Popper. Stellar masses. *ARA&A*, 18:115–164, 1980.

D. M. Popper and M. M. Dworetsky. Improved orbits of the visual binary del Equ. *PASP*, 90:71–72, February 1978.

D. Pourbaix. Resolved double-lined spectroscopic binaries: A neglected source of hypothesis-free parallaxes and stellar masses. *A&AS*, 145:215–222, August 2000.

S. H. Pravdo and S. B. Shaklan. Astrometric Detection of Extrasolar Planets: Results of a Feasibility Study with the Palomar 5 Meter Telescope. *ApJ*, 465:264–+, July 1996.

G. Rabl and R. Dvorak. Satellite-type planetary orbits in double stars - A numerical approach. *A&A*, 191:385–391, February 1988.

L. F. Rodriguez, P. D'Alessio, D. J. Wilner, P. T. P. Ho, J. M. Torrelles, S. Curiel, Y. Gomez, S. Lizano, A. Pedlar, J. Canto, and A. C. Raga. Compact protoplanetary disks around the stars of a young binary system. *Nature*, 395:355–357, 1998.

V. S. Safronov. *Evolution of the Protoplanetary Cloud and Formation of the Earth and the Planets.* Coronet Books, —c1972, 1972.

S. K. Saha. Modern optical astronomy: technology and impact of interferometry. *Reviews of Modern Physics*, 74:551–600, April 2002.

C. D. Scarfe, D. J. Barlow, F. C. Fekel, R. F. Rees, R. W. Lyons, C. T. Bolton, H. A. McAlister, and W. I. Hartkopf. The spectroscopic-speckle triple system HR 6469. *AJ*, 107:1529–1541, April 1994.

J. Schneider. The extrsolar planets encyclopaedia. *http://www.obspm.fr/encycl/encycl.html*, 2003.

M. Shao, A. F. Boden, M. M. Colavita, B. F. Lane, P. R. Lawson, and PTI Collaboration. Differential Astrometry of the 61 Cygni System with the Palomar Testbed Interferometer. *Bulletin of the American Astronomical Society*, 31:1504–+, December 1999.

M. Shao and M. M. Colavita. Potential of long-baseline infrared interferometry for narrow-angle astrometry. *A&A*, 262:353–358, August 1992.

M. Shao, M. M. Colavita, B. E. Hines, D. H. Staelin, and D. J. Hutter. The Mark III stellar interferometer. *A&A*, 193:357–371, March 1988.

M. Shao and D. H. Staelin. First fringe measurements with a phase-tracking stellar interferometer. *Appl. Opt.*, 19:1519–1522, May 1980.

S. Sigurdsson, H. B. Richer, B. M. Hansen, I. H. Stairs, and S. E. Thorsett. A Young White Dwarf Companion to Pulsar B1620-26: Evidence for Early Planet Formation. *Science*, 301:193–196, July 2003.

M. Simon, A. M. Ghez, C. Leinert, L. Cassar, W. P. Chen, R. R. Howell, R. F. Jameson, K. Matthews, G. Neugebauer, and A. Richichi. A lunar occultation and direct imaging survey of multiplicity in the Ophiuchus and Taurus star-forming regions. *ApJ*, 443:625–637, April 1995.

B. Smalley and M. M. Dworetsky. The calibration of uvbyβ photometry for B, A and F stars. I. Fundamental atmospheric parameters. *A&A*, 293:446–456, January 1995.

S. Söderhjelm. Visual binary orbits and masses post hipparcos. *A&A*, 341:121–140, 1999.

G. A. Starikova. Orbits for 44 visual binaries. *Soviet Astronomy Letters*, 7:130–+, April 1981.

M. F. Sterzik and A. A. Tokovinin. Relative orientation of orbits in triple stars. *A&A*, 384:1030–1037, March 2002.

K. G. Strassmeier, D. S. Hall, F. C. Fekel, and M. Scheck. A catalog of chromospherically active binary stars (second edition). *A&AS*, 100:173–225, July 1993.

O. Struve. On some lately discovered Double Stars. *MNRAS*, 20:8–+, November 1859.

O. Struve and K. L. Franklin. Spectrographic Observations of Visual Double Stars. *ApJ*, 121:337–+, March 1955.

F. Svensson and H.-G. Ludwig. Hydrodynamical Simulations of Convection-Related Stellar Micro-variability. *Proceedings of the 13th Cool Stars Workshop, Hamburg, 5-9 July 2004, F. Favata et al. eds. astro-ph 0409714*, July 2004.

T. ten Brummelaar, B. D. Mason, H. A. McAlister, L. C. Roberts, N. H. Turner, W. I. Hartkopf, and W. G. Bagnuolo. Binary Star Differential Photometry Using the Adaptive Optics System at Mount Wilson Observatory. *AJ*, 119:2403–2414, May 2000.

A. R. Thompson, J. M. Moran, and G. W. Swenson. *Interferometry and synthesis in radio astronomy.* Interferometry and synthesis in radio astronomy by A. Richard Thompson, James M. Moran, and George W. Swenson, Jr. 2nd ed. New York : Wiley, c2001.xxiii, 692 p. : ill. ; 25 cm. "A Wiley-Interscience publication." Includes bibliographical references and indexes. ISBN : 0471254924, 2001.

A. A. Tokovinin. Interferometric Observations of Double Stars. *Astronomicheskij Tsirkulyar*, 1097:3–+, 1980.

A. A. Tokovinin. Interferometer observations of double stars. I. *Soviet Astronomy Letters*, 8:22–24, February 1982a.

A. A. Tokovinin. Interferometer observations of double stars. II. *Soviet Astronomy Letters*, 8:99–101, April 1982b.

A. A. Tokovinin. Interferometer Observations of Double Stars - Part Three. *Soviet Astronomy Letters*, 9:293–+, June 1983.

A. A. Tokovinin. Interferometric observations of double stars in 1983 and 1984. *A&AS*, 61:483–486, September 1985.

A. A. Tokovinin. Relative orientation of angular momenta in multiple star systems. *Astronomy Letters*, 19:383–388, September 1993.

A. A. Tokovinin. MSC - a catalogue of physical multiple stars. *A&AS*, 124:75–84, July 1997.

A. A. Tokovinin and R. M. Ismailov. Interferometric Observations of Double Stars in 1985 and 1986. *A&AS*, 72:563–+, March 1988.

G. Torres, M. Konacki, D. D. Sasselov, and S. Jha. The transiting planet OGLE-TR-56b. *American Astronomical Society Meeting Abstracts*, 203:–+, December 2003.

W. A. Traub, N. P. Carleton, and I. L. Porro. A search technique for planets in nearby binary stars using a ground-based interferometer. *J. Geophys. Res.*, 101 (.10):9291–9296, 1996.

G. van Biesbroeck. Micrometric Measures of Double Stars. *ApJS*, 28:413–+, November 1974.

P. van de Kamp. A determination of the parallax and mass-ratio Of K Pegasi. *AJ*, 53:34–+, October 1947.

P. van de Kamp. Masses of visual binaries. *AJ*, 59:447–+, December 1954.

P. van de Kamp and S. L. Lippincott. A determination of the parallax and mass-ratio of 6 Equulei. *AJ*, 51:162–+, September 1945.

W. H. van den Bos. *Union Obs. Circ.*, 4:134, 1935.

W. H. van den Bos. Micrometer measures of double stars. *AJ*, 67:141–+, March 1962.

W. H. van den Bos. Micrometer measures of doubles stars. III. *AJ*, 68:57–+, February 1963.

W. V. van Hamme, D. S. Hall, A. W. Hargrove, G. W. Henry, R. Wasson, W. S. Barkslade, S. Chang, R. E. Fried, C. L. Green, H. C. Lines, R. D. Lines, P. Nielsen, H. D. Powell, R. C. Reisenweber, C. W. Rogers, S. Shervais, and R. Tatum. The two variables in the triple system HR 6469 = V819 Her: One eclipsing, one spotted. *AJ*, 107:1521–1528, April 1994.

F. van Leeuwen, D. W. Evans, M. Grenon, V. Grossmann, F. Mignard, and M. A. C. Perryman. The HIPPARCOS mission: photometric data. *A&A*, 323:L61–L64, July 1997.

S. S. Vogt, G. W. Marcy, R. P. Butler, and K. Apps. Six New Planets from the Keck Precision Velocity Survey. *ApJ*, 536:902–914, June 2000.

R. Wasson, D. S. Hall, A. W. Hargrove, A. Bertoglio, E. W. Burke, G. J. Frey, R. E. Fried, G. Galli, C. L. Green, and N. Iacovone. Ten years of eclipse timings to refine the period of HR 6469=V819 HER. *AJ*, 107:1514–1520, April 1994.

C. A. Watson and V. S. Dhillon. The effect of star-spots on eclipse timings of binary stars. *MNRAS*, 351:110–116, June 2004.

D. P. Whitmire, J. J. Matese, L. Criswell, and S. Mikkola. Habitable Planet Formation in Binary Star Systems. *Icarus*, 132:196–203, March 1998.

R. H. Wilson. *Publ. Univ. Penn.*, 6.4:3, 1941a.

R. H. Wilson. *Publ. Univ. Penn.*, 6.4:21, 1941b.

R. H. Wilson. Observations of double stars. *AJ*, 55:153–+, August 1950.

R. H. Wilson. Observations of double stars - Summer 1950. *AJ*, 56:69–+, May 1951.

R. H. Wilson. Double star observations in 1951. *AJ*, 57:248–+, December 1952.

R. H. Wilson. Double stars observations in 1953. *AJ*, 59:256–+, August 1954a.

R. H. Wilson. Observations of double stars in 1952. *AJ*, 59:132–+, April 1954b.

R. H. Wilson. Double star observations in 1954. *AJ*, 60:446–+, December 1955.

A. Wolszczan and D. A. Frail. A planetary system around the millisecond pulsar PSR1257 + 12. *Nature*, 355:145–147, January 1992.

J. Woltjer. On a special case of orbit determination in the theory of eclipsing variables. *Bull. Astron. Inst. Netherlands*, 1:93–+, June 1922.

C. E. Worley. Measures of 266 double stars. *AJ*, 62:153–+, July 1957.

C. E. Worley. Measures of 278 double stars. *AJ*, 67:403–+, August 1962.

A. T. Young. Photometric error analysis. VI. Confirmation of Reiger's theory of scintillation. *AJ*, 72:747–+, August 1967.

J.-P. Zahn. Tidal friction in close binary stars. *A&A*, 57:383–394, May 1977.

S. Zucker and T. Mazeh. On the Mass-Period Correlation of the Extrasolar Planets. *ApJ*, 568:L113–L116, April 2002.